Development of in vitro bioelectronic implant aging

Jacob Sporrer
Vivek Subramanian, Ed.
Michel Maharbiz, Ed.
Ana Claudia Arias, Ed.
Kevin Healy, Ed.

Electrical Engineering and Computer Sciences
University of California, Berkeley

Technical Report No. UCB/EECS-2024-28
http://www2.eecs.berkeley.edu/Pubs/TechRpts/2024/EECS-2024-28.html

May 1, 2024

Development of in vitro bioelectronic implant aging

By

Jacob Jeffry Sporrer

A dissertation submitted in partial satisfaction of the

requirements for the degree of

Doctor of Philosophy

in

Engineering – Electrical Engineering and Computer Sciences

in the

Graduate Division

of the

University of California, Berkeley

Committee in charge:

Professor Vivek Subramanian, Chair

Professor Ana Claudia Arias

Professor Michel Maharbiz

Professor Kevin Edward Healy

Fall 2022

Abstract

Development of in vitro bioelectronic implant aging

by

Jacob Jeffry Sporrer

Doctor of Philosophy in Engineering – Electrical Engineering and Computer Sciences

University of California, Berkeley

Professor Vivek Subramanian, Chair

Intracortical recording devices have the capability to bring functionality back to people that have lost it through neurological conditions and injuries. These devices have been demonstrated in humans to control robotic limbs and enable brain-to-text communication. One major drawback of current intracortical recording technology is the limited effective recording lifetime of implant technology. To evaluate the lifetime of implants, durability studies are performed on implant designs. Current in vitro accelerated aging methods use heated saline baths intended to accelerate implant degradation using elevated temperatures and hydrogen peroxide to simulate the reactive oxygen attack that implants undergo as a part of the foreign body response.

The focus of this thesis will be on the development of a microfluidic platform for durability evaluation of intracortical recording devices as well as a novel aging method that uses immune cells to simulate this reactive species attack. This work describes a microfluidic chamber design and fabrication process as well as techniques to control the reactive oxygen attack in the microreactor. The degradation of neural probes aged in microfluidic chambers using the saline/hydrogen peroxide method and the immune cell method is evaluated and compared to in vivo device degradation. An acceleration factor for immune cell aging is proposed for the acceleration of the reactive oxygen-induced polymer chain scission that occurs in vivo. Lastly, this work presents a model for implant lifetime prediction that incorporates both biological and material failure mechanisms using an equivalent circuit model for a neural implant.

Acknowledgements

To my academic advisor, Professor Vivek Subramanian, thank you for encouraging me to seek out problems worth solving and for giving me opportunities to do work that I find meaningful.

To the academic mentors that have guided me, Professor Martin Thuo, Professor Alan Constant, Professor Michel Maharbiz, Professor Kevin Healy, Professor Ana Arias, and Professor Stephanie Lacour, thank you for making me a better scientist, educator, and researcher.

To the lab mates I've worked with, Matt McPhail, Will Scheideler, Raj Kumar, Carlos Biaou, Alvin Li, Nishita Deka, Steve Volkman, Annelies Sels, Mustafa Fadelmula, Kyle Haas, Mengmeng Deng, Jinhui Guo, Biruktait Ayele, Sanjay Manoharan, Babak Mazinani, and the entire LAFT, LSBI, and INK labs, thank you for the advice and camaraderie.

To my wife, Laura, thank you for the constant support and love. Thank you for moving across the Atlantic Ocean with me. Thank you for believing in me through it all. <3

To my friends and family, thank you for always supporting me.

Table of Contents

Chapter 1. Introduction

1.1 Neural implants

Neural implants have the capability to bring functionality back to people that have lost it through genetic conditions, neurological conditions, and injuries. These devices have been demonstrated in humans to treat Parkinson's [1], control robot limbs [2], and enable language in non-verbal patients [3]. Neural stimulation can be therapeutic and neural recording allows us to extract the intent of the brain when biological pathways have been severed. Developing technologies have the potential to improve quality of life for patients suffering from mental illness, amputation, or paralysis.

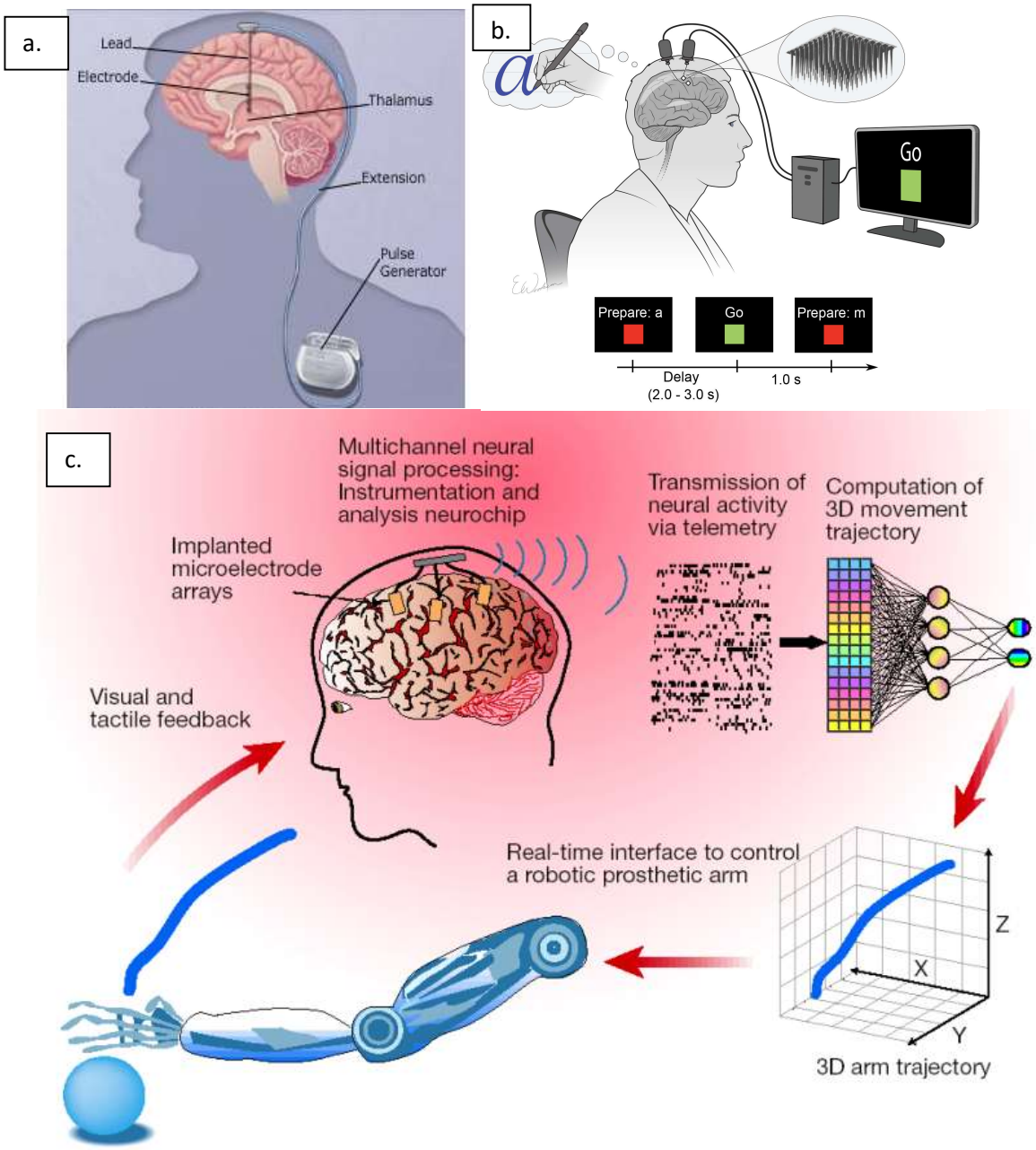

Figure 1.1 a. Implantable deep brain stimulator technology for Parkinson's treatment.[17] b. Thought-to-text conversion technology for non-verbal patients.[3] c. Schematic of brain machine interface for robotic limb control.[18] d. Human trial of brain machine interface for robotic limb control.[2]

Figure 1.1 showcases some examples of neural implant technology. Figure 1.1a is a schematic of the deep brain stimulator. The deep brain stimulator provides relief from the tremor commonly associated with Parkinson's disease. The deep brain stimulator has been in use clinically for 25 years. It features a long shank that penetrates into the thalamus and provides electrical stimulus. The power supply is implanted in the chest and a lead is implanted that transports power from the pulse generator in the chest to the electrode in the brain. This device requires brain surgery, but despite the risks associated, more than 100,000 [27] of these devices have been implanted.

Figure 1.1b and 1.1c are experimental technologies that aim to restore function. These technologies use arrays of electrodes implanted intracortically to record individual neurons. The general experimental procedure for recording devices intended to restore function starts with a training period. The experimentalist will ask the subject to attempt an activity, i.e., writing a letter or moving a limb. When the subject attempts that activity, their neurons will fire in specific configurations. After many training sessions of attempting a variety of desired tasks, each task is mapped to a configuration of firing neurons by a computer. The next step is to have the patient attempt a task to see if the computer can translate the neuron configuration to the correct task, i.e., that patient tries to write the letter "A" and the computer correctly identifies the patient's neural activity as the letter "A". A similar translation would occur for a patient attempting to move their left hand to the right. The goal of an implant like this is to maximize the fraction of correct intent identifications. Once the neural environment of the implant is mapped, the implant and computer are connected to a machine. This machine could be a robotic limb, a computer cursor, a text editor, or any interface with external hardware or software. Once this process is refined, the

patient performs trials with the machine. This technology is called a brain-machine interface. Figure 1.1d is from a study where a patient that is paralyzed from the neck down is controlling a robotic arm to bring a beverage to her mouth. This study shows the incredible potential of brain-machine interfaces to restore function.

Not all neural recording is for the purpose of brain-machine interfaces. The brain is incredibly complex. Another application of neural recording is in understanding the operation of a healthy brain as well as how unhealthy brains differ from healthy ones. Neural recording is frequently used clinically to diagnose and localize epilepsy to aid in treatment. Additionally, neural recording has the potential to give insight into the mechanisms of depression, post-traumatic stress disorder, and a myriad of other mental illnesses. The combination of recording and stimulation has significant potential for treatment of these disorders. Neuropharmaceuticals act by increasing or suppressing neural activity in specific regions of the brain. Pairing recording with stimulation to localize and specifically target abnormal neural regions has the potential to increase the potency of treatment while reducing the side effects associated with neuropharmaceuticals.

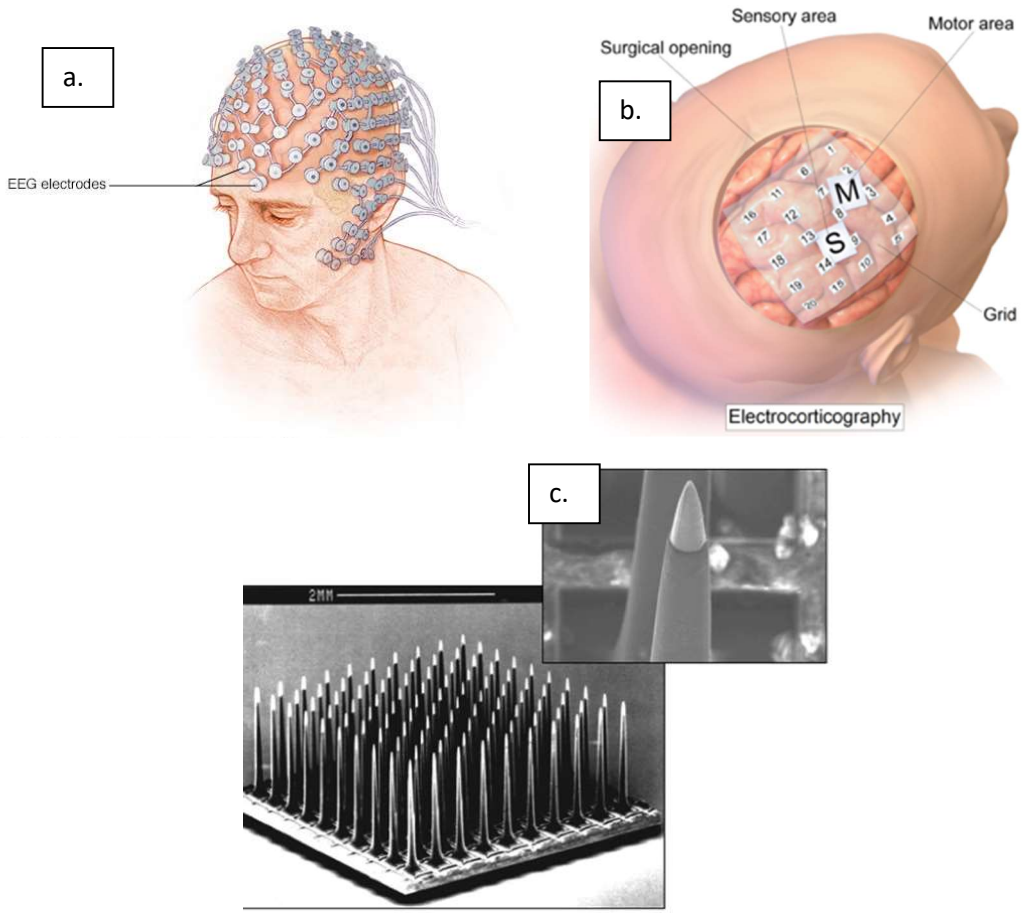

Figure 1.2 a. EEG electrodes are placed on the scalp to do large area neural activity recording. [19] b. ECOG electrodes are placed on the brain below the skull to more precisely record neural activity.

[20] c. Intracortical implants are implanted into brain tissue to record individual neurons, providing the most precise recordings. This implant is the Utah Electrode Array. [21]

1.1.1 Neural implant technologies

Stimulating devices have been in use clinically in the form of the deep brain stimulator for 25 years. Stimulating devices typically require an electrode and a source of electrical energy to operate. They deliver current to a region of the nervous system to alleviate symptoms like the hand tremor commonly seen in Parkinson's patients.

Neural recording has long been researched to understand the brain [4]. Recording electrodes come in many different styles. Intracortical recording devices have increased specificity when compared to EEG (electroencephalogram) and ECOG (electrocorticography).

Figure 1.2a shows a schematic of an EEG device, a technology where the electrodes are placed on the scalp and record entire regions of the brain. EEG electrodes are arranged in the form of an array of discs sewn into a cap. The cap is placed directly on the scalp to minimize the distance between the recording sites and the brain and maximize the neural signal captured. EEG is in use clinically for the identification of epilepsy, stroke, and brain death. The data is collected in the form of a time resolved voltage. The shape, frequency, and intensity of the recorded brain waves is used to identify brain irregularities. No surgery is required for EEG and there are very few risks associated. EEG cannot resolve individual neurons, but instead records general brain activity.

In figure 1.2b, an ECoG device schematic is shown where the electrodes are placed on the surface of the brain, below the skull, and record clusters of neurons. The two types of ECoG are epidural (on top of the dura) and subdural (below the dura). ECoG requires a craniotomy to implant the device on the surface of the brain. The ECoG device typically consists of a flexible mesh array of electrodes. The skull attenuates a significant amount of neural signal. Therefore, ECoG has a significant advantage over EEG in terms of recording resolution, making it a valuable tool for identifying regions of interest before brain surgery. One of the most common applications of ECoG is for presurgical identification of epileptic regions before epileptic resectioning is performed. ECoG devices record the local field potentials of the brain and have the potential to be used for brain-machine interfaces. ECoG requires a craniotomy, making it an invasive technology that comes with the associated risks of brain surgery.

Figure 1.2c shows an intracortical recording device. Intracortical recording devices pierce the meninges and require a craniotomy, making them the most invasive neural recording device structure. An intracortical single potential recording device records individual neurons and, when placed in the primary motor cortex, can use the patterns from several electrodes to determine the intent of the brain. This has been demonstrated in non-human primate and human brains. [2,5] Piercing the meninges can be risky; blood clotting, infection, and meningitis can result. Due to the invasiveness of intracortical recording devices, they must offer considerable benefits and longevity over alternative recording techniques.

The primary barrier to the adoption of intracortical recording devices is the lifetime of implants. In a study of NHP (non-human primates) studies, 70% of arrays failed within a year [5]. Considering that each array has 100 individual electrodes, and every single electrode must be rendered nonfunctional for the array to be reported as "failed", there must be significant improvement before these devices can be considered for therapeutic applications. The gold standard for implant lifetime is the pacemaker which is replaced every 6-10 years. In order for implantation of neural recording devices to be clinically viable, we must increase the lifetime of intracortical implants to the 5-10 year range [6]. Chapter 5 describes a modelling framework to explore the contributions to implant failure for intracortical implants in greater detail.

Figure 1.3 comes from the study of implants in NHPs. Figure 1.3a shows the rapid decline in viable arrays over time. The particular array that was focused on was the Utah multielectrode array shown in figure 1.2c. This array is one of very few FDA approved intracortical recording devices and serves as a benchmark against which other implants are measured. The failure of these arrays in vivo was further characterized into type of failure and time to failure as a function of type of failure (figure 1.3b and 1.3c). Several assumptions go into deciding how to design implant evaluation strategies. One such assumption is that any device design must limit acute failure. Acute failure arises from the implantation process. An acute biological failure might be intracranial bleeding or implant site infection. An example of an acute mechanical failure is a faulty implantation process that fractures the electrode array. Due to the short-term nature of acute failure, it is a problem that can be solved without aging studies.

Therefore, the focus of the majority of implant improvement is in the prevention of chronic failure. The goal of many neural recording devices, particularly those used for brain-machine interfaces is chronic use. It is the chronic failure mechanisms that are of interest for the purpose of implant lifetime improvement. These failures are divided into biological failure and material failure. The average time to failure for biological failure is significantly shorter than for material failure, but even the average time to failure for material failure falls short of the desired 5-10 years by a significant margin. While this study only evaluated a single intracortical design, it is certainly the most comprehensive review of in vivo chronic intracortical implant failure and clearly demonstrates the need for device design improvement before clinical application is viable. There is a large community of scientists developing new device designs to meet this goal. The goal of this work is to provide these scientists with better tools to determine the efficacy of their device design improvements for chronic applications. The next sections of this chapter will outline the current understanding of the mechanisms of intracortical device failure, device design strategies employed for intracortical devices, and the current methods to predict chronic performance of these devices.

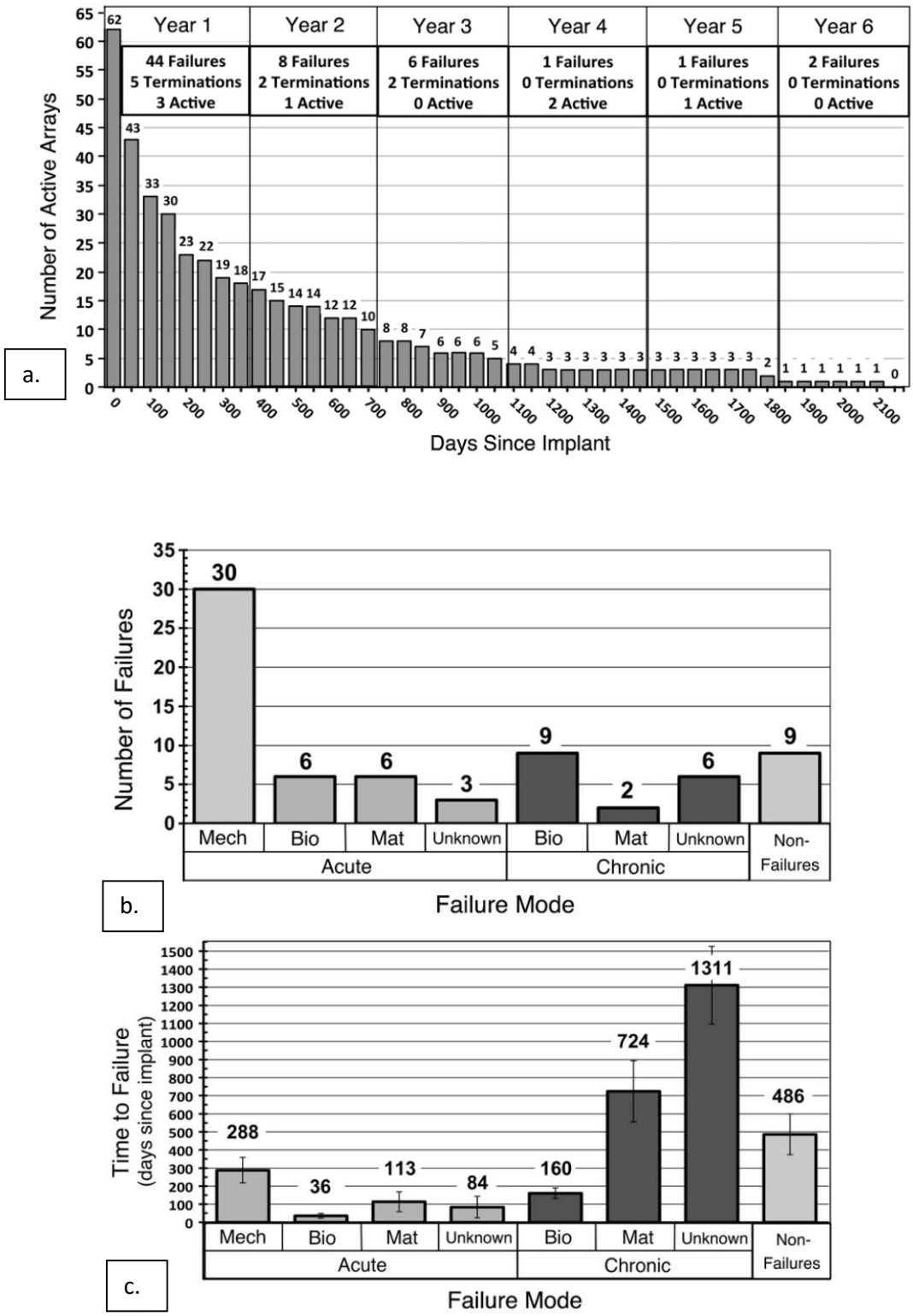

Figure 1.3 a. In a study of Utah MEAs implanted in NHPs, more than 70% of arrays failed within 1 year of implantation. Only 1 of 62 arrays survived through year 5. [5] b,c. Those failures were analyzed by failure type and time-to-failure to determine the prevailing issues with the technology. [5]

1.1.2 Biological response and electrode failure

Figure 1.4 shows some common failure mechanisms of intracortical implants as well as the biological response to device implantation. When an object is placed in the human body, the body has a defense system to protect itself. Floating throughout the body are cells called macrophages. Macrophages can exhibit one of two phases, type 1 macrophages are inflammatory and cause a local response to the foreign body whether it be a stick, a flu virus, an allergen, or a neural implant. Type 2 macrophages are anti-inflammatory. One goal of implant design to minimize the recruitment of type 1 macrophages. The common approach for short-term immune response minimization is a surface coating, but none have been durable enough for chronic (5+ years) use in the brain so far. The lack of effective anti-inflammatory coatings mean that the immune response is a critical factor to consider in the design of chronic implants. Another assumption made in chronic implant lifetime prediction is that the immune response will play a role in device degradation at some point in the lifetime of the device.

The response of macrophages to a foreign body depends on the foreign body's size. Bacteria, for instance, are engulfed by the macrophage. The macrophage uses its enzymes to destroy the bacteria. When something large, like an implant, is introduced, the macrophage cannot engulf it. Instead, the macrophage employs an alternative strategy. It releases signaling agents to recruit more macrophages to the area. Then, the macrophage goes through a process called oxidative burst where it releases reactive oxygen species, primarily superoxide and nitrogen oxide ions. These reactive species attack the foreign body via a free radical degradation mechanism. They steal the foreign body's electrons and degrade its bonds. These reactive oxygen species have a very short lifetime in the body due to enzymes like superoxide dismutase which prevent damage to healthy cells by converting reactive oxygen to less harmful compounds, like hydrogen peroxide, which will eventually break down into water. Over time, fibrosis begins to occur and fibrous, scar-like tissue forms at the implant-tissue interface.

Simultaneously, the electrode materials of an implant are being attacked by the chemical environment of the body. Warm saline environments are notoriously aggressive at breaking down metallic compounds and metal oxides. Polymer materials can suffer from swelling that may reduce their insulating properties, form pinholes, or cause delamination from the electrode material.

The foreign body response is not specific to the brain. However, in the brain, there are several other cell types of importance in this process. Neurons are the electrically excitable cells in the brain that transmit information. Neurons are the cells that recording and stimulation implants target. Glial cells act as a support system for the brain. They hold neurons in place, supply nutrients, and protect neurons from attack. When a foreign body is introduced into the neural environment, some glial cells, macrophages called microglia, are recruited to the area and begin the inflammation and wound response process. These cells also begin the fibrosis process.

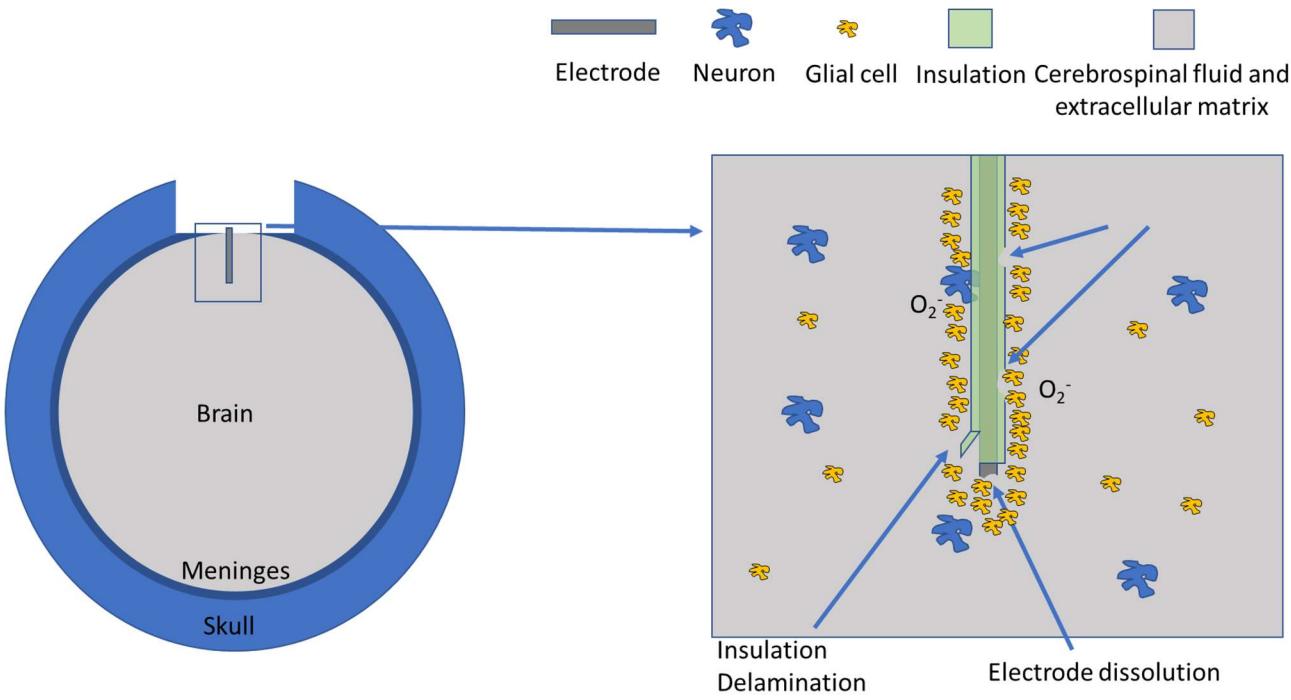

Figure 1.4 Intracortical implants are implanted by opening a window in the skull and implanting electrodes into the brain tissue. Over time, immune cells, reactive oxygen, and the warm saline neural environment break down the implanted electrode, rendering it unable to properly record neural activity.

Failure in a neural implant can take many forms. Acute biological failure can occur if there is significant infection or bleeding upon implantation that threatens the health of the patient. Chronic biological failure can occur when fibrous tissue forms at the recording site, reducing the signal received from nearby neurons until the signal to noise ratio is unsuitable for recording. Acute material failure can occur if an implant fractures during the surgical process or if implantation forces cause insulation tearing. Chronic material failure can take the form of insulation pinhole formation, delamination, or disintegration. Electrode materials can corrode and oxidize in response to the neural environment. Mechanical failure is when an implant is affected by outside forces, pulling on a tether, scratching the implant site, and impact on the skull are some of the reported sources of mechanical failure. Implants must be designed with all these failure modes in mind and there is often a tradeoff between durability, sensitivity, specificity, and inflammation recruitment.

1.1.3 Intracortical device designs

In order to address these failure modes and improve device lifetime, several design principles have arisen. Generally, it is believed that the best implants are soft, flexible, small, and wireless [6]. Hard, stiff implants (MPa-GPa) tend to stimulate chronic foreign body response and fibrosis in the brain due to micromotion. An implant on the order of kPa that moves and flexes with the brain would likely reduce the micromotion-induced biological response. It is hypothesized that a hard

implant can be made much more tolerable if it is very small and untethered [7]. Neural dust implants are designed to “float” on the brain surface, moving with the brain and preventing the typical fibrosis associated with hard implant materials (figure 1.5b). Wired implants, sometimes referred to as tethered implants, are the most common style in use. These implants must tether to somewhere on the skull in order to make a connection to the external computer. This tethering leads to stress on the brain as the implant is not allowed to freely move with the micromotion of the brain and will stress the brain anytime that it is pulled away from its tether point. Additionally, the tethering point can be a persistent infection risk. Providing communication and power wirelessly through the skull has proven difficult as the most common form of wireless power transfer, inductive coupling, has tissue heating concerns. Ultrasonic power has been demonstrated as a potential wireless power transfer method but has its own issues with efficiently transmitting acoustic power through mechanically mismatched layers of skull, cerebrospinal fluid, meninges, and grey matter tissue.

There are several recording device designs, but the overall structure is consistent across designs. The exposed recording site is a conductive material connected to the data I:O by a continuous conductive path. In order to prevent recording too many neurons per recording site, the exposed recording site must be small (on the order of a few neurons) and the conductive path must be insulated.

A basic design is the wire probe (figure 1.5a). The wire probe is simply a wire that is entirely coated in an insulating material except for the exposed recording site tip and the data I:O connection. Wire probes can be placed in arrays for multisite recording. Wire probes are simple to manufacture and effective at recording but are inefficient for multiple recording sites as each site requires a separate wire, reducing recording density.

There are a series of designs based on the Utah multielectrode array (figure 1.2c). The Utah electrode array is created by etching a silicon wafer to form an array of recording “spikes”. The entire array is then conformally vapor coated with Parylene C. After the vapor deposition, the Parylene C is etched off the spike tips using an ion beam to reveal a small recording site. The Utah multielectrode design takes advantage of the incredible body of knowledge of silicon processing to achieve improved recording site density. These devices can be manufactured to a high degree of precision but suffer from the issues associated with using stiff materials.

The multielectrode shank (figure 1.5c) is another multielectrode array design. Instead of a series of spikes where each spike is a single recording site, this design places multiple recording sites on a single shank. Within the shank, many individual traces run in parallel to their individually exposed recording sites. This device design can achieve extremely high recording site density and can be modified to use flexible materials. The shank size required to accommodate multiple recording sites in a multielectrode shank array can lead to increased displaced tissue upon implantation and the accompanying immune response and cell death.

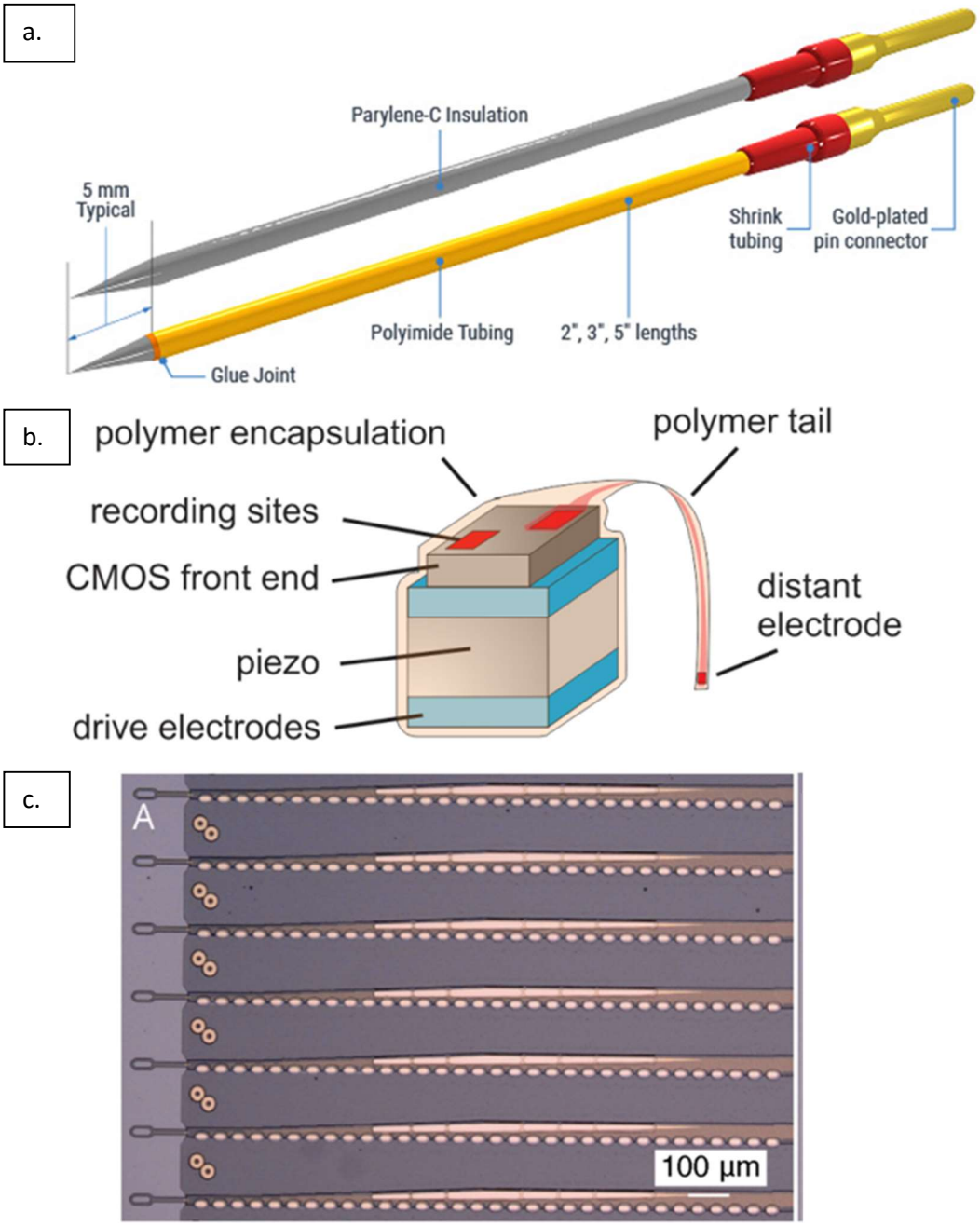

Figure 1.5 a. Design for a basic, single wire probe for intracortical neural recording. [22] b. Neural dust implant design for wireless, acoustically powered neural recording. [23] c. Flexible, multielectrode implant design to reduce the stiffness and compliance mismatch based immune response in neural implants. [24]

There are several other recording electrode designs, but these three are the most common platforms that are designed around. Much of the development in electrode design is in the pursuit

of softer, more compliant, smaller, higher recording site count, wireless versions of these device structures.

There are two main materials choices in designing an implant: the conductive material and the insulating material. Silicon is a common conductive material due to the vast body of knowledge on the microfabrication of silicon devices. Silicon has a significantly mismatched modulus compared to brain tissue and has been shown to induce considerable immune response in chronic implantation applications [5,6]. Historically, tungsten was the material of choice due to its durability in handling. A long, thin probe could be handled by human hands without the probe breaking. In more modern devices, the recording site is typically a platinum or platinum/iridium alloy. These alloys are corrosion resistant and have high charge transfer capacity [8]. Conductive material choices have gotten more exotic in the pursuit of compliant implants with conducting polymers [9], liquid metals [10], and flexible semiconductors being proposed for implantable devices. The insulating material of choice is Parylene C. Parylene C can be deposited via vapor deposition, enabling a thin, conformal coating of the electrode. Polyimide and certain metal oxides have also been used [11,12]. Polyimide suffers from moisture ingress issues and metal oxides tend to be poor moisture barriers at the thicknesses required for neural recording.

Of critical importance is the interface between the insulating and conductive material. Some implant designs aim to fabricate the implant from a single material that can be modified to be conductive or insulating in order to eliminate any mismatch between the insulating and conductive material. One such design is the silicon carbide implant, where conductive silicon carbide is used for the conductive traces and recording sites and insulating silicon carbide is used for the insulating material. [26]

1.2 Electrode lifetime prediction

In order to determine if an implant design is suitable for clinical application, the lifetime of that implant must be evaluated. Implants that fail quickly will not be considered for chronic implantation. There are two main methods to evaluate implant lifetime: In vivo and In vitro.

1.2.1 In vivo testing

The in vivo method consists of putting an implant in a living being (rodent, primate typically) and performing some tests. Historically, the timescale for in vivo testing has been short (1-4 weeks) as maintaining animals is expensive and the results of the desired experiment are obtainable in this timeframe. The tests generally consist of learning about the brain by putting an animal through a maze, training it to drink under some stimulation, or teaching it to control a prosthetic. Under this testing modality, the lifetime/reliability of the device does not come into play because the testing period is short. However, several chronic durability studies have been conducted on implants aged in vivo [5,8,13,14]. The advantage of in vivo testing is that it tends to serve as a very representative analogue to predict device longevity in clinical applications. The disadvantage of in vivo testing is that it can be expensive and time-consuming. Maintenance of living beings for scientific study is

complicated. Implants have been reported to fail due to NHPs physically removing the device or smashing it against a wall, complicating aging studies. To predict chronic performance in vivo, the implant must be placed in an animal for the entirety of the relevant duration. It would be virtually impossible to test every new implant design in a NHP model for 5+ years.

1.2.2 In vitro testing and accelerated aging

In vitro testing serves as a complement to in vivo testing. The in vitro method consists of placing the implant in a model solution and studying how it breaks down under an accelerated aging model. Typical designs consist of a heated PBS bath where the acceleration factor is calculated using an acceleration prediction that 10 °C doubles the rate of degradation [15,25]. The advantage of acceleration is that it can significantly reduce the time required to evaluate implant durability. An acceleration factor of 30x will reduce the aging time from 5 years to 2 months. Accelerated aging acts as an important prerequisite to in vivo characterization.

The most important question to ask of accelerated aging is “is it representative?” There are two major deviations from the neural environment that heated saline misses. The first is the temperature range. The human body is roughly 37 °C. In order to reach the ~30x acceleration, the temperature of our aging system must be approximately 87 °C. Several materials used in neural implants, particularly polymers, are extremely temperature sensitive. Many of these materials begin undergoing phase transitions around 90 °C. Aging a material that has undergone a phase transition violates the assumptions laid out by the Arrhenius relationship that this acceleration model is built on. Careful attention must be paid when choosing the temperature of an accelerated aging system. The second deviation is the presence of immune cells in the body. Heated saline makes no attempt to recreate the degrading effect of the foreign body response on implant materials. In order to improve the quality of accelerated aging for neural implants, controlled amounts of hydrogen peroxide have been introduced into the solution. This is intended to simulate the effects of the foreign body response and oxidative burst observed in vivo. However, the concentration and relevance of hydrogen peroxide in the degradation process is not well understood. The need for representative acceleration has been expressed by several authors [16,25].

1.3 Proposal and thesis organization

The goal of this work is to demonstrate a novel microfluidic platform for accelerated aging of neural implants. Two aging modalities are demonstrated in the microreactor: 1. The current state of the art saline and hydrogen peroxide method and 2. A novel, macrophage-based aging method. This platform has been demonstrated for neural implants but should provide value for any bioelectronic implant that is sensitive to foreign body response-generated reactive oxygen. As device designs become more and more divergent, increased durability evaluation will be required. In vivo testing for durability will not be an option for every new implant and current in vitro testing methods are not perfectly representative. This work provides an alternate path to acceleration of

the biological attack suffered by neural implants to enhance the prediction of implant failure in vivo.

This thesis will be organized into chapters. Chapter 2 describes the microfluidic platform and macrophage activation validation. Chapter 3 shows the results of the saline and peroxide aging method. Chapter 4 reports the results of the macrophage-based aging method. Chapter 5 is about a lifetime prediction model for neural implants. Chapter 6 showcases future research directions to address the need for representative accelerated aging of neural implants.

References

1. Benabid A, L, Pollak P, Louveau A, Henry S, de Rougemont J: Combined (Thalamotomy and Stimulation) Stereotactic Surgery of the VIM Thalamic Nucleus for Bilateral Parkinson Disease. Stereotact Funct Neurosurg 1987;50:344-346. doi: 10.1159/000100803
2. Hochberg, L., Bacher, D., Jarosiewicz, B. et al. Reach and grasp by people with tetraplegia using a neurally controlled robotic arm. Nature 485, 372–375 (2012). https://doi.org/10.1038/nature11076
3. Willett, F.R., Avansino, D.T., Hochberg, L.R. et al. High-performance brain-to-text communication via handwriting. Nature 593, 249–254 (2021). https://doi.org/10.1038/s41586-021-03506-2
4. Kawala-Sterniuk A, Browarska N, Al-Bakri A, Pelc M, Zygarlicki J, Sidikova M, Martinek R, Gorzelanczyk EJ. Summary of over Fifty Years with Brain-Computer Interfaces-A Review. Brain Sci. 2021 Jan 3;11(1):43. doi: 10.3390/brainsci11010043. PMID: 33401571; PMCID: PMC7824107.
5. Barrese, James C., Naveen Rao, Kaivon Paroo, Corey Triebwasser, Carlos Vargas-Irwin, Lachlan Franquemont, and John P. Donoghue. “Failure Mode Analysis of Silicon-Based Intracortical Microelectrode Arrays in Non-Human Primates.” Journal of Neural Engineering 10, no. 6 (November 2013): 066014. https://doi.org/10.1088/1741-2560/10/6/066014.
6. Wellman, Steven M., James R. Eles, Kip A. Ludwig, John P. Seymour, Nicholas J. Michelson, William E. McFadden, Alberto L. Vazquez, and Takashi D. Y. Kozai. “A Materials Roadmap to Functional Neural Interface Design.” Advanced Functional Materials 28, no. 12 (2018): 1701269. https://doi.org/10.1002/adfm.201701269.
7. Neely, Ryan M., David K. Piech, Samantha R. Santacruz, Michel M. Maharbiz, and Jose M. Carmena. “Recent Advances in Neural Dust: Towards a Neural Interface Platform.” Current Opinion in Neurobiology 50 (2018): 64–71. https://doi.org/10.1016/j.conb.2017.12.010.
8. Cassar, Isaac R., Chunxiu Yu, Jaydeep Sambangi, Curtis D. Lee, John J. Whalen, Artin Petrossians, and Warren M. Grill. “Electrodeposited Platinum-Iridium Coating Improves in Vivo Recording Performance of Chronically Implanted Microelectrode Arrays.” Biomaterials 205 (June 1, 2019): 120–32. https://doi.org/10.1016/j.biomaterials.2019.03.017.
9. Green, Rylie A., Nigel H. Lovell, Gordon G. Wallace, and Laura A. Poole-Warren. “Conducting Polymers for Neural Interfaces: Challenges in Developing an Effective Long-Term Implant.” Biomaterials 29, no. 24 (August 1, 2008): 3393–99. https://doi.org/10.1016/j.biomaterials.2008.04.047.
10. Guo, Rui, and Jing Liu. “Implantable Liquid Metal-Based Flexible Neural Microelectrode Array and Its Application in Recovering Animal Locomotion Functions.” Journal of Micromechanics and Microengineering 27, no. 10 (September 2017): 104002. https://doi.org/10.1088/1361-6439/aa891c.
11. Rubehn, Birthe, and Thomas Stieglitz. “In Vitro Evaluation of the Long-Term Stability of Polyimide as a Material for Neural Implants.” Biomaterials 31, no. 13 (May 1, 2010): 3449–58. https://doi.org/10.1016/j.biomaterials.2010.01.053.
12. Xie, Xianzong, Loren Rieth, Layne Williams, Sandeep Negi, Rajmohan Bhandari, Ryan Caldwell, Rohit Sharma, Prashant Tathireddy, and Florian Solzbacher. “Long-Term Reliability of Al2O3 and Parylene C Bilayer Encapsulated Utah Electrode Array Based Neural Interfaces

for Chronic Implantation." Journal of Neural Engineering 11, no. 2 (March 2014): 026016. https://doi.org/10.1088/1741-2560/11/2/026016.
13. Woeppel, Kevin, Qianru Yang, and Xinyan Tracy Cui. "Recent Advances in Neural Electrode–Tissue Interfaces." Current Opinion in Biomedical Engineering, Synthetic Biology and Biomedical Engineering / Neural Engineering, 4 (December 1, 2017): 21–31. https://doi.org/10.1016/j.cobme.2017.09.003.
14. Prasad, Abhishek, Qing-Shan Xue, Viswanath Sankar, Toshikazu Nishida, Gerry Shaw, Wolfgang J. Streit, and Justin C. Sanchez. "Comprehensive Characterization and Failure Modes of Tungsten Microwire Arrays in Chronic Neural Implants." Journal of Neural Engineering 9, no. 5 (September 2012): 056015. https://doi.org/10.1088/1741-2560/9/5/056015.
15. Hukins, D. W. L., A. Mahomed, and S. N. Kukureka. "Accelerated Aging for Testing Polymeric Biomaterials and Medical Devices." Medical Engineering & Physics, Special issue to commemorate the 30th anniversary of Medical Engineering & Physics, 30, no. 10 (December 1, 2008): 1270–74. https://doi.org/10.1016/j.medengphy.2008.06.001.
16. Fallegger, Florian, Giuseppe Schiavone, and Stéphanie P. Lacour. "Conformable Hybrid Systems for Implantable Bioelectronic Interfaces." Advanced Materials 32, no. 15 (2020): 1903904. https://doi.org/10.1002/adma.201903904.
17. "Deep Brain Stimulation", WebMD, Inc. 2002. https://www.webmd.com/parkinsons-disease/guide/dbs-parkinsons WebMD, LLC. All rights reserved
18. Rothschild, Ryan. (2010). Neuroengineering Tools/Applications for Bidirectional Interfaces, Brain–Computer Interfaces, and Neuroprosthetic Implants – A Review of Recent Progress. Frontiers in neuroengineering. 3. 112. 10.3389/fneng.2010.00112.
19. "EEG Electrodes", Mayo foundation for medical education and research. https://www.mayoclinic.org/tests-procedures/eeg/multimedia/eeg-electrodes/img-20005916
20. Blausen.com staff (2014). "Medical gallery of Blausen Medical 2014". WikiJournal of Medicine 1 (2). DOI:10.15347/wjm/2014.010. ISSN 2002-4436
21. Romero, Samuel & Morillas, Christian & Pelayo, Francisco & Fernandez, Eduardo. (2008). Computer-Controlled Neurostimulation for a Visual Implant.. BIODEVICES 2008 - Proceedings of the 1st International Conference on Biomedical Electronics and Devices. 1. 84-91.
22. "Monopolar Electrodes" Microprobes for Life Science. 2022. https://microprobes.com/products/metal-microelectrodes/monopolar-electrodes
23. Seo, Dongjin, Jose M. Carmena, Jan M. Rabaey, Elad Alon, and Michel M. Maharbiz. "Neural Dust: An Ultrasonic, Low Power Solution for Chronic Brain-Machine Interfaces." arXiv, July 8, 2013. http://arxiv.org/abs/1307.2196.
24. Musk, Elon. "An Integrated Brain-Machine Interface Platform with Thousands of Channels," 2019, 12.
25. Street, Matthew G., Cristin G. Welle, and Pavel A. Takmakov. "Automated Reactive Accelerated Aging for Rapid in Vitro Evaluation of Neural Implant Performance." Review of Scientific Instruments 89, no. 9 (September 2018): 094301. https://doi.org/10.1063/1.5024686.
26. C Diaz-Botia et al. J Neural Eng, 2017.

27. Lozano, Andres M., Nir Lipsman, Hagai Bergman, Peter Brown, Stephan Chabardes, Jin Woo Chang, Keith Matthews, et al. “Deep Brain Stimulation: Current Challenges and Future Directions.” Nature Reviews. Neurology 15, no. 3 (March 2019): 148–60. https://doi.org/10.1038/s41582-018-0128-2.

Chapter 2. Microfluidic bioelectronic implant accelerated aging platform

2.1 Background

Microfluidic devices see use in cell culture, energy, chemistry, and beyond. Microfluidic devices are often employed in applications that require laminar flow, low volume liquid processing, a sterile environment, or multiplexing capability. In this work, a microfluidic bioreactor is used for accelerated aging of neural implants. A neural implant is placed in the microfluidic chamber and a representative aging solution is introduced to the chamber. This chapter will outline the optimization of the microfluidic chamber and reactive oxygen maintenance techniques used in later chapters for both hydrogen peroxide and immune cell-generated reactive oxygen in sections 2.2 and 2.3 respectively.

In section 1.1.2, the immune response to intracortical implants was described. One component of the immune response is the generation of reactive oxygen species. As neural implant technology advanced from short-term, 1-3 week studies, to chronic recording studies conducted over multiple years, implant durability became a critical factor in the success of recording experiments. In response to the increased importance of long-term performance, accelerated aging techniques started being applied to intracortical probes. The early versions of accelerated aging techniques used heated saline[7]. Implant designers hypothesized that the reactive oxygen generated in vivo in response to device implantation may play a role in intracortical device degradation. To capture the effect of reactive oxygen attack on neural implants, hydrogen peroxide was introduced to the aging solution[6]. Hydrogen peroxide is an important reactive oxygen species in the immune response. Shortly after immune cells generate reactive oxygen, an enzyme called superoxide dismutase converts superoxide to hydrogen peroxide[8]. Capturing the effects of reactive oxygen could be achieved using a readily available solution, hydrogen peroxide.

[6] describes a method for maintaining a consistent hydrogen peroxide concentration in a heated phosphate buffered saline bath. This method was called reactive accelerated aging, or RAA, and involved the use of a timed addition of peroxide addition. [6] measured the half-life of hydrogen peroxide at the elevated temperature of aging and set up a timer to replace the hydrogen peroxide at appropriate intervals using a peristaltic pump. This method was able to maintain hydrogen peroxide concentrations within 10 mM. In a follow-up paper, [1], this method was refined as shown in figure 2.1. Using a raspberry pi, electrochemical monitoring of hydrogen peroxide concentration, and a peristaltic pump, they were able to actively monitor hydrogen peroxide concentration and add hydrogen peroxide whenever the concentration dropped. This method was able to maintain hydrogen peroxide concentration within 3 mM. This method is the state of the art for reactive accelerated aging as it requires low human interaction and maintains temperature and hydrogen peroxide concentration within tight tolerances.

There are several complications with a setup like this. 1. Active monitoring of hydrogen peroxide requires electronics and increases experimental complexity. 2. Active monitoring of hydrogen peroxide requires a method to accurately measure the concentration in real time. Electrical monitoring of the saline-peroxide system is difficult at low peroxide concentrations. 3. Large vessels are difficult to transport for in situ measurements. 4. Evaporated water can interact with electrode components, confounding realistic in vivo failure mechanisms with peroxide aging system specific failure modes.

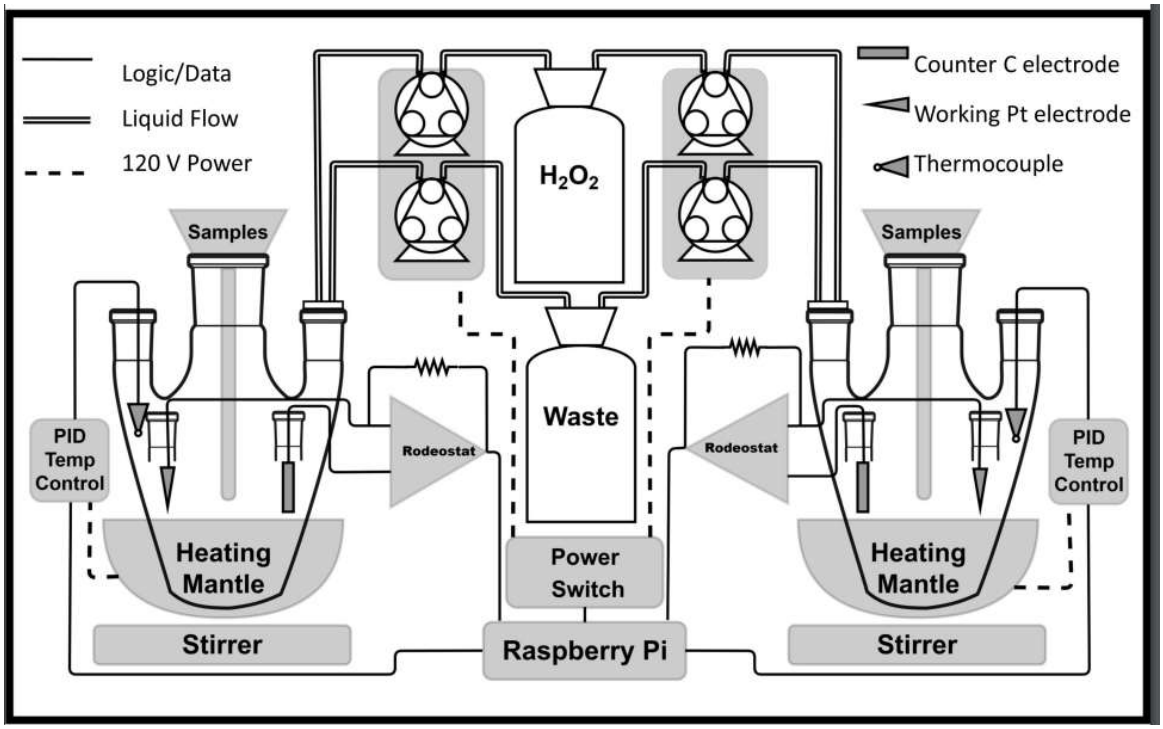

Figure 2.1. Active peroxide maintenance system [1]

Development of a microfluidic platform to downscale the standard is attractive and addresses some of the concerns above. Reproducing the saline-peroxide aging method using microfluidics is relatively straightforward. The desired peroxide concentration is flowed through the microfluidic chamber faster than the peroxide decays.

Microfluidics also enable an alternative aging mechanism, immune cell-generated reactive species, which will be the focus of much of the subsequent chapters of this thesis. The sterile environment of the microfluidic chamber is ideal for cell culture and accelerated aging can be achieved by the intermittent introduction of immune cell activating species to stimulate the production of reactive oxygen from immune cell culture.

Microfluidic devices see use in lab-on-a-chip, organ-on-a-chip, rapid diagnostics, microanalytical methods and many more fields. Microfluidics are typically employed in applications that require laminar flow and benefit from low solution volumes. Early microfluidic devices were created in silicon and glass, benefiting from the expertise of the microfabrication community. However, once

biologists began to realize the potential of microfluidics, materials that could support cell culture became desirable. Fully enclosed glass and silicon devices did not provide adequate gas permeation to sustain cell life. Microfluidic technology began to advance rapidly upon the development of soft lithography for microfluidic devices wherein a curable polymer, polydimethylsiloxane, is patterned over a lithographically defined photoresist to form microfluidic channels[9]. PDMS has appropriate gas permeability properties for cell culture and is easily bonded to glass or itself using oxygen plasma bonding. This chapter outlines the development of a glass-PDMS chamber, but initially, a polystyrene chamber was preferred. PDMS has a few limitations for cell culture. Unreacted monomer or initiator can cause unwanted cell differentiation if the curing process is not fully completed. Additionally, PDMS is highly water vapor permeable and evaporation from microfluidic chambers has been observed[2]. Polystyrene is the material of choice for the majority of dish cell culture. Cell line interactions with tissue culture polystyrene dishes have been heavily investigated[2], making polystyrene an attractive choice for microfluidic cell culture. The next section will describe the development of a hot embossed polystyrene microfluidic device that was deemed unsuitable for microfluidic neural implant accelerated aging as well as the PDMS-glass chamber that was used for the investigations in chapters 3 and 4.

2.2 Chamber design

2.2.1 Polystyrene chambers

The polystyrene chamber was fabricated using a hot embossing technique modified from [2]. Figure 2.2 shows the general process flow for the fabrication of the microfluidic chambers in one sheet of polystyrene and the bonding process to seal the chamber to another piece of polystyrene. The process calls for an epoxy mold to emboss features onto a polystyrene sheet. The epoxy mold is fabricated by curing epoxy in a PDMS mold. The PDMS mold is patterned by curing PDMS on a silicon wafer with features defined by lithographically patterned SU-8. The resulting epoxy mold is placed in a heated press in contact with the polystyrene sheet.

For the polystyrene microfluidic process, a chamber mold was fabricated by curing epoxy resin on a PDMS mold with the chamber feature shape. The epoxy resin mold was then pressed in a heated press with a polystyrene sheet. The embossing process caused material damage to the epoxy resin mold. Additionally, the bonding process caused the chambers to collapse. In order to remedy these failures, an experiment testing different embossing and bonding conditions was performed.

Fabrication Process for top layer "feature" polystyrene

1. Air clean PS and mold
2. Place Teflon sheet on press at temperature
3. Place mold on Teflon
4. Place PS on mold
5. Place Teflon on PS
6. Apply pressure
7. Cool press to 70°C
8. Remove pressure
9. Remove PS from mold using a razor blade

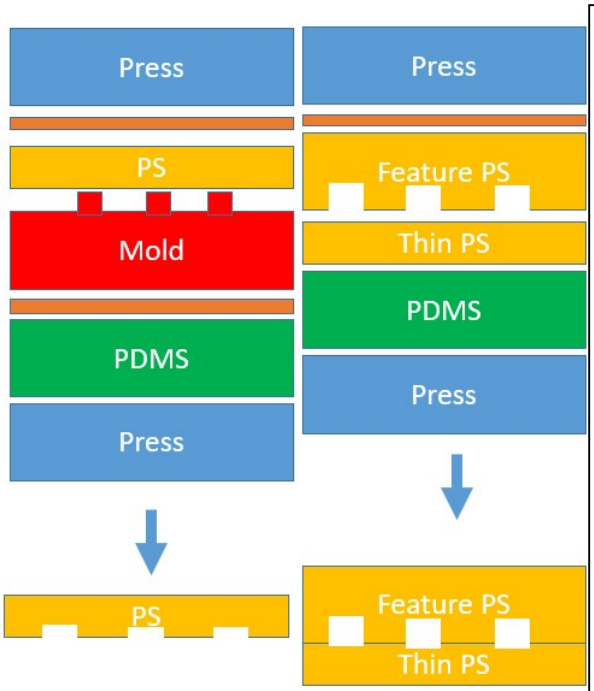

Fabrication Process to bond "feature" polystyrene to thin base layer polystyrene sheet

1. Air clean PS with features and thin base
2. Place feature PS on base PS
3. Heat to 85°C
4. Apply pressure
5. Cool press to 70°C
6. Remove pressure
7. Remove PS from mold using a razor blade

Figure 2.2. Polystyrene microfluidic embossing and bonding processes

The embossing experiment was a partial factorial experiment with 3 factors: temperature of the press, pressure of the press, and time of pressure application. In this experiment, the responses were "% usable surface" and "area of epoxy mold damage in um^2". Both responses were measured visually using ImageJ. Figure 2.3 shows the surface plot of temperature vs pressure for both the fraction of the finish part that was successfully embossed and the area of the mold that was damaged during the embossing process. Pressure was the most significant factor for mold damage with a p-value <.05, showing increased damage with increased pressure. Increasing pressure and temperature were both significant (p-values <.05) in increasing usable "feature" polystyrene surface. The competing demands of maximizing usable surface while minimizing mold damage were not met under any temperature/pressure condition. Additionally, run number, the number of times the same mold was used, was evaluated to determine if repeated mold use would increase the damage caused by the embossing process. The run number analysis showed that the epoxy mold was unsuitable for repeat use. Increasing run number increased mold damage with a p-value of <.05.

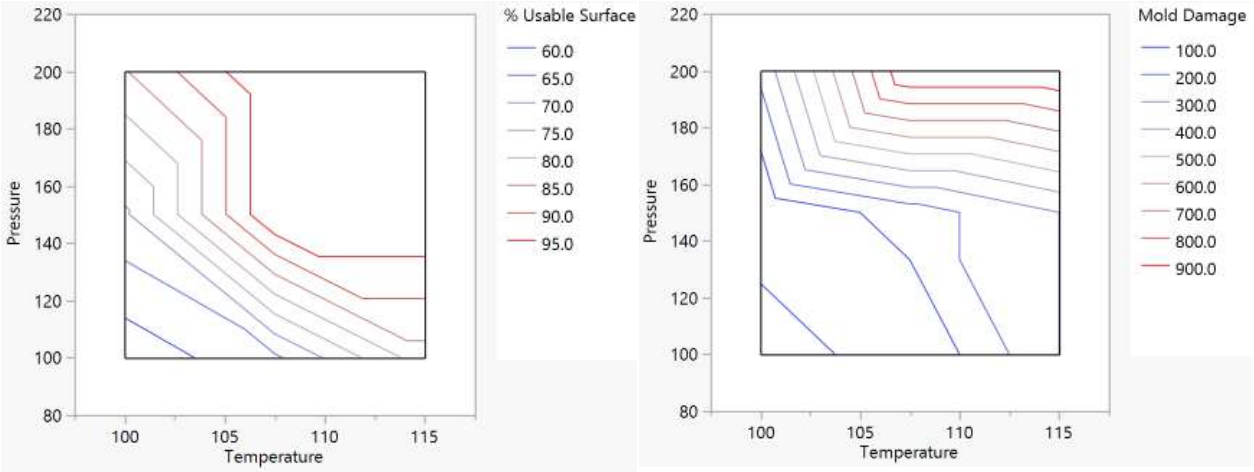

Figure 2.3. Surface map of embossing experiment results. Conditions with successful embossing show significant mold damage.

The bonding experiment was a partial factorial experiment with 3 factors: temperature of the press, pressure of the press, and plasma treatment of the polystyrene. In this experiment, the responses were "% bonded surface" and "% collapsed chamber". The most significant factor was pressure of the press with a p-value of <.05 for both "% bonded surface" and "% collapsed chamber". Increasing pressure led to increased bonding and increased chamber collapse with no conditions showing suitable bonding without unacceptable chamber collapse. Responses were measured visually using ImageJ. An example of a fully collapsed chamber is shown in figure 2.4.

Figure 2.4. Collapsed polystyrene chamber showing viable fluid path in green

The results of these experiments showed that hot embossing was unsuitable for polystyrene chambers of this size. Not only was the epoxy mold material not durable enough for repeat use at the desired temperature and pressure conditions, even when an acceptable "feature" polystyrene was produced, there were no bonding conditions that led to a usable microfluidic chamber.

2.2.2 Glass/PDMS soft lithography chambers

While polystyrene is the current material of choice for tissue culture, glass is also an appropriate choice and was the material used for cell culture dishes before polystyrene was adopted. Soft lithography and plasma bonding of PDMS glass chambers were selected to build the accelerated aging microreactor.

The microfluidic chambers were fabricated using a soft lithography process in a cleanroom. The process flow for microfluidic chamber fabrication is shown in figure 2.5. For the mold, a blank, 100 mm silicon wafer was spin-coated with SU-8 2100 to a final thickness of 130 um. The SU-8 was patterned using a custom mask and a contact aligner. The wafer was then placed in developer and rinsed. The dimensions of the SU-8 chamber molds were evaluated using stylus profilometry. For the chamber, Sylgard 184 was mixed with its crosslinker, placed in a Mixer Thinky for 1 min at 2000 rpm, and degassed. The wafer mold was then placed in a 150 mm tissue culture polystyrene dish. The Sylgard 184 was carefully poured over the wafer. Any included gas bubbles were removed using tweezers and a nitrogen gun. The mold was then placed in an oven at 75C for at least 5 hours to harden.

After removing the chambers from the oven, the PDMS was peeled off the silicon wafer mold. The PDMS chambers were then cut out using a razor blade. A 3.5 mm biopsy punch was used to make ports for tubing. Next, a 25x75 mm glass slide was placed in an oxygen plasma tool with the cut out PDMS chamber. An oxygen plasma treatment was applied to the surface of the parts. After removing the glass and PDMS from the chamber, the electrodes were placed on the PDMS with appropriate spacing. The glass slide was then sandwiched on top of the PDMS and electrodes. A completed chamber is shown in figure 2.6.

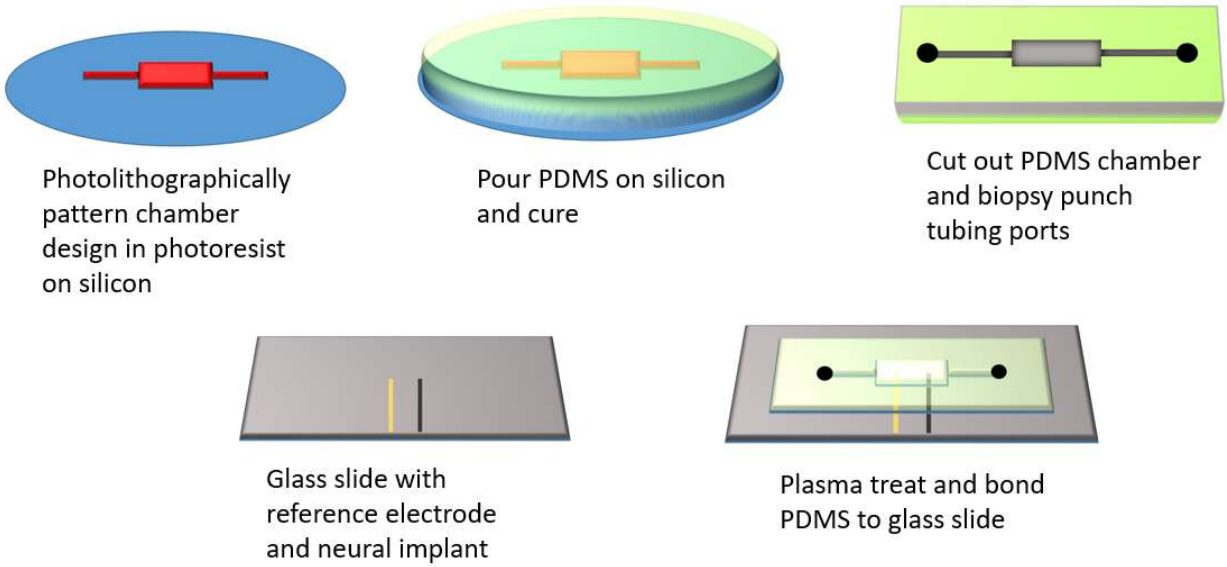

Figure 2.5. Microfluidic chamber process flow

The sandwiched electrodes were chosen based on the purpose of the chamber. For the amperometry chamber, the electrodes were 1. Ag/AgCl reference electrode, 2. Pt counter electrode, 3. Pt working electrode. For the probe aging chamber, the electrodes were 1. Microprobes for Life Sciences, 2. Ag/AgCl reference electrode. The Ag/AgCl reference electrode was fabricated from a Ag wire that was briefly rinsed in HCl to remove the oxide layer. Then the wire was placed in ethanol to rinse the electrode. Lastly, the wire was submerged in sodium hypochlorite bleach for 15 minutes until it turned a dull grey.

There is some risk of leaks when sandwiching wires between the glass and PDMS layers. One strategy that was attempted was to carefully pipette a small amount of Sylgard 184 onto the chamber/wire interface. This strategy did prevent leaks in some cases but led to Sylgard 184 backfilling into the chamber and plugging the microfluidic device. Figure 2.7 and figure 2.8 show the effects of the PDMS sealing process on the chamber integrity. Figure 2.8 shows clear signs of PDMS backfilling, rendering the microfluidic chamber nonfunctional. Leaks were instead minimized by optimizing the plasma bonding process and placing 2 kg weights on the finished chambers, applying pressure uniformly over the PDMS/glass bonding area.

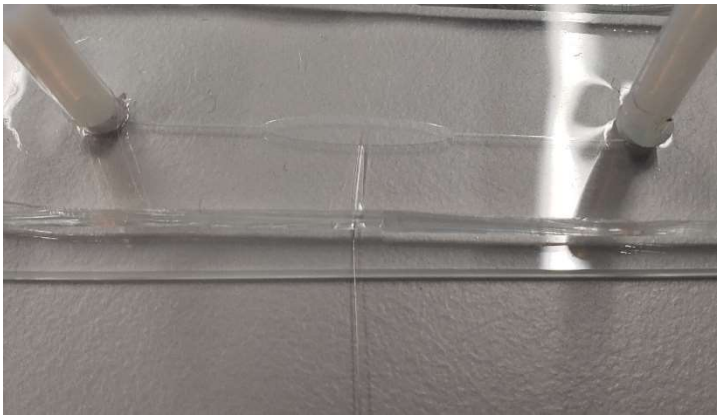

Figure 2.6. Final microfluidic chamber

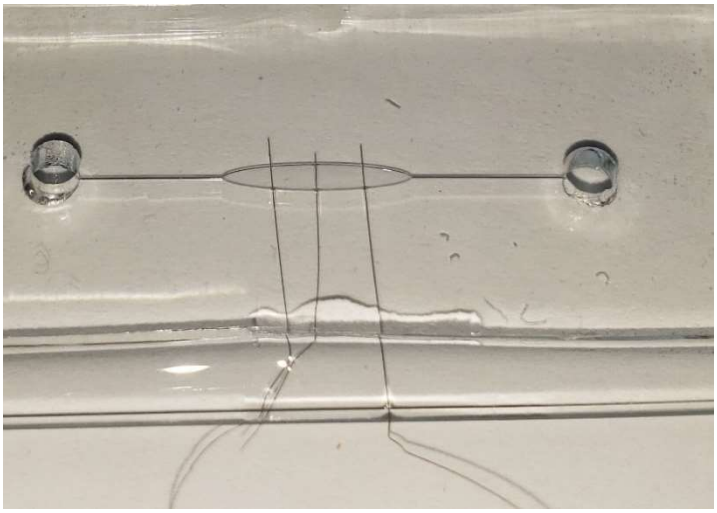

Figure 2.7. Microfluidic chamber with successful PDMS sealing

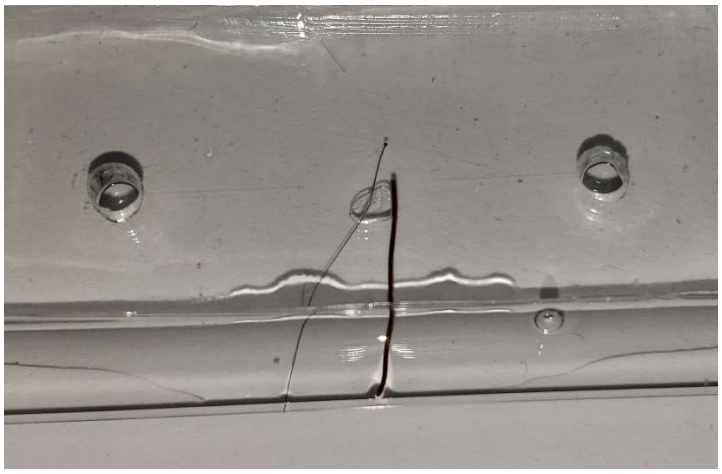

Figure 2.8. Microfluidic chamber with unsuccessful PDMS sealing (backfilled)

2.2.3 Chamber Shape

The initial design was a rectangular chamber from [3]. This chamber suffered from significant bubble formation. A multifactorial experiment was designed to evaluate the appropriate chamber shape. For elliptical chambers, the factors were elliptical ratio, presence of an external bubble trap, and fluid flow rate. The responses were bubble density and cell density. For the hexagonal chambers, the factors and responses were the same with elliptical ratio replaced by chamber entrance angle. The goal of this experiment was to determine the chamber shape that limited bubble formation without significant cell density disruption. The results of this experiment suggested that increasing elliptical ratio decreased bubble density with a p-value < .05. The other factors, hexagonal chamber entrance angle, presence of a bubble trap, and flow rate did not have a significant impact on the presence of bubbles or the cell density. A chamber with a high elliptical ratio was chosen for final bioreactor design. Figure 2.9 shows a selection of the chamber designs that were evaluated for the microfluidic bioreactor. Figure 2.10 includes data from different flow rate and bubble trap configurations plotted solely as a function of elliptical ratio, demonstrating the improvements from using a high elliptical ratio. As this chamber is intended to operate as a microreactor and not a channel, higher elliptical ratios were not evaluated.

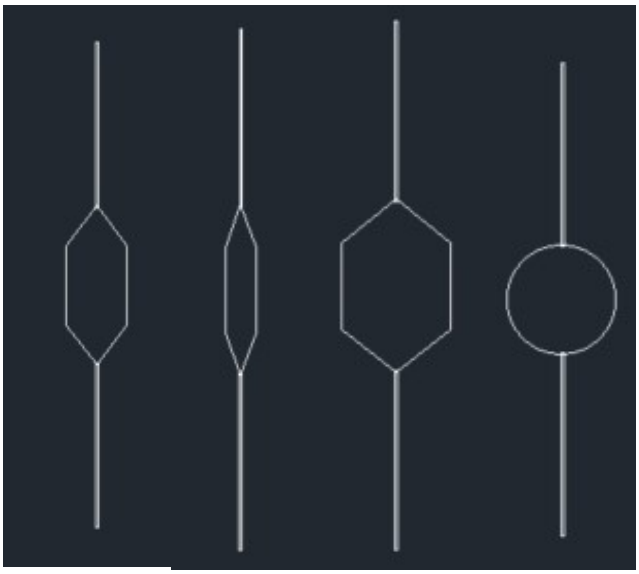

Figure 2.9. Hexagonal and elliptical chamber designs

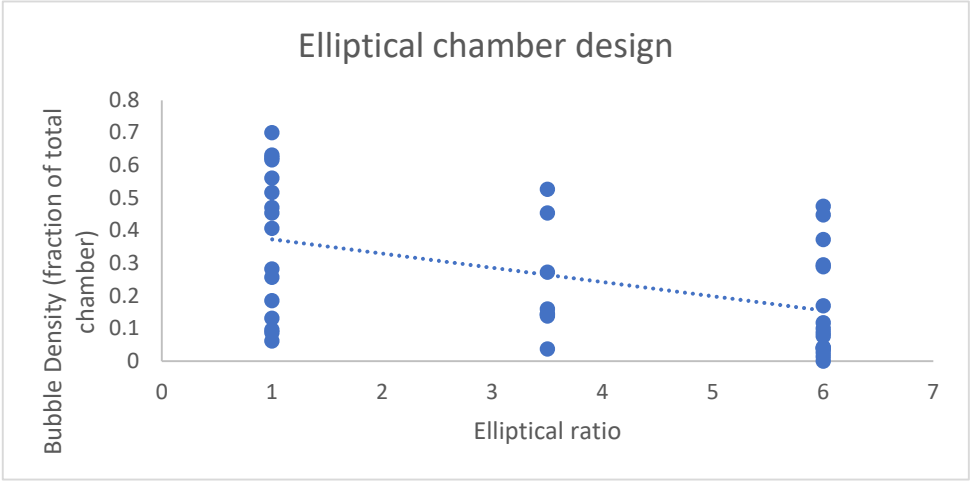

Figure 2.10. Increasing elliptical ratio decreased bubble density observed in microfluidic bioreactors

2.3 Peroxide Maintenance

Figure 2.1 showed a lab setup for active maintenance of hydrogen peroxide in a heated saline bath. The experimental setup for hydrogen peroxide maintenance in a microfluidic chamber is a syringe pump connected to a microfluidic chamber placed on a hotplate, shown in figure 2.11c. In order to determine a suitable flow rate under which hydrogen peroxide concentration could be maintained, a colorimetric method was employed. Titanium(IV) Oxysulfate turns a yellow-brown color upon introduction to hydrogen peroxide. In this experiment, the goal was to select a flow rate where the hydrogen peroxide concentration going into the chamber was the same as the hydrogen peroxide concentration leaving the chamber. While a perfect match would be ideal, a variation of 3 mM was deemed adequate as this value is on par with the state-of-the-art technique.

Phosphate buffered saline with hydrogen peroxide at concentrations of 5-40 mM was mixed with Titanium (IV) Oxysulfate at a 2:1 sample:oxysulfate ratio. This 2:1 ratio solution is too dark to show usable sensitivity to hydrogen peroxide concentration at the concentrations evaluated, shown in figure 2.11a. Increasing the ratio to 10:1 or even 20:1 did not solve the problem. Instead, a precipitate formed, shown in figure 2.11b. The correct procedure is to make the 2:1 ratio solution and then dilute the entire sample 10x with deionized water. This diluted solution shows good sensitivity to hydrogen peroxide concentration. The range of expected colors is shown in figure 2.11d. A Beer's law concentration standard was established using UV-Vis (figure 2.12). The absorbance at 407 nm was measured and compared across concentrations (figure 2.13). Using the concentration curve, the concentration of hydrogen peroxide was measured before and after flowing through the chamber at different flow rates at an elevated temperature of 87 °C (table 2.1). No condition showed unacceptable levels of deviation from the initial concentration. A flow rate of .005 mL/min was chosen to minimize the solution used for aging. At this flow rate, 7.2 mL of PBS/hydrogen peroxide solution is required per day and a 1 L bottle of PBS will last for 2 weeks of aging 10 separate chambers without the use of active monitoring of the hydrogen peroxide concentration. Thus, there is a significant peroxide consumption reduction benefit to using the microfluidic platform proposed herein vs the conventional systems used for peroxide aging.

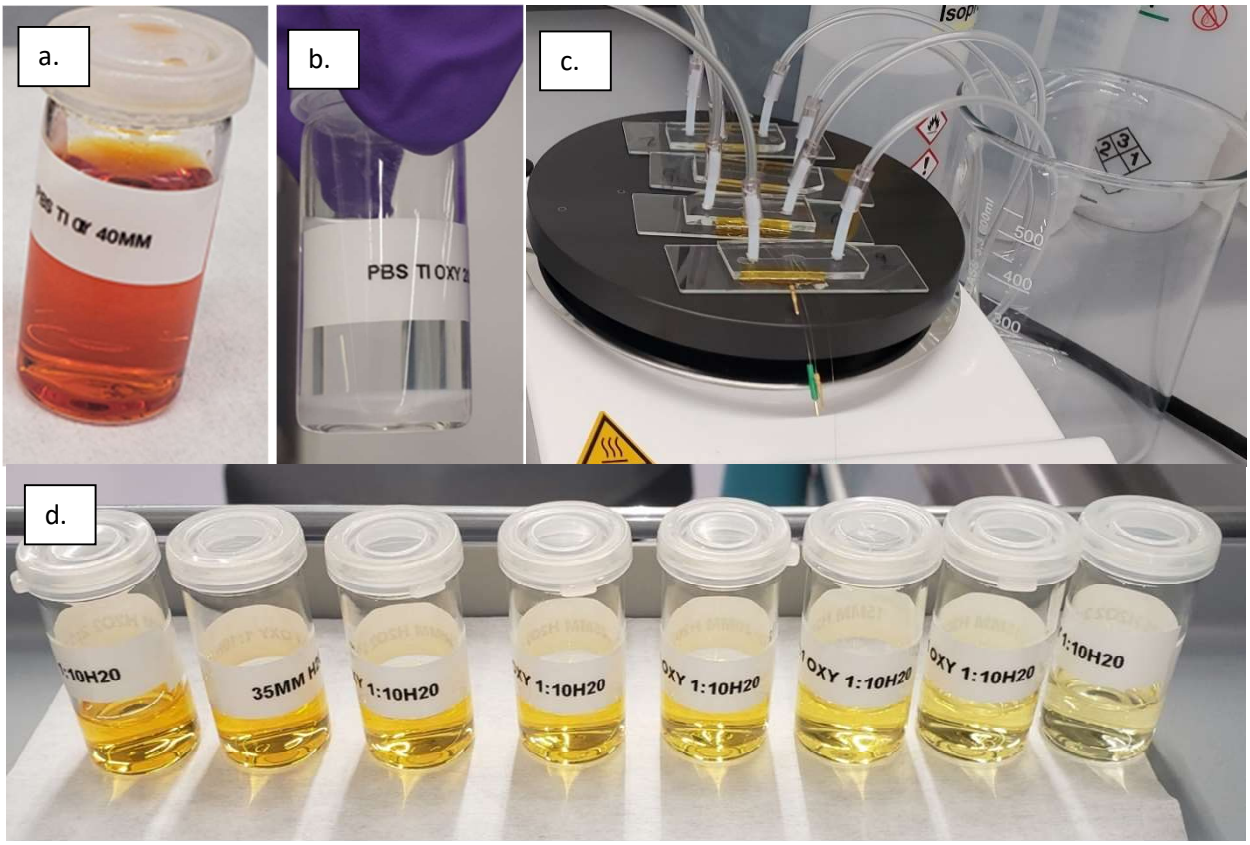

Figure 2.11. Colorimetric hydrogen peroxide concentration quantification a. 2:1 PBS/H_2O_2: Titanium oxysulfate solution. b. 20:1 PBS/Peroxide: Titanium oxysulfate solution. c. H_2O_2 aging setup. H_2O_2

concentration was measured before and after flowing through the chamber. d. Left to right: 40 mM H_2O_2 to 5 mM H_2O_2 after 10x dilution

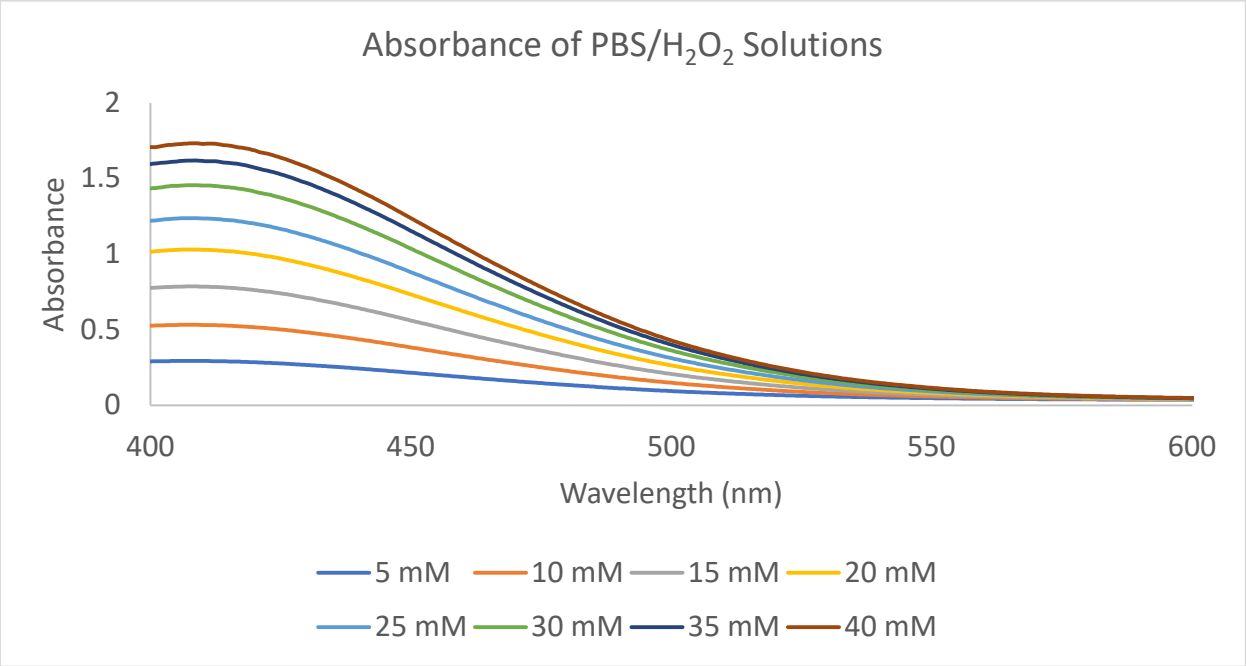

Figure 2.12. UV/Vis spectrum measured from varying concentrations of hydrogen peroxide solutions

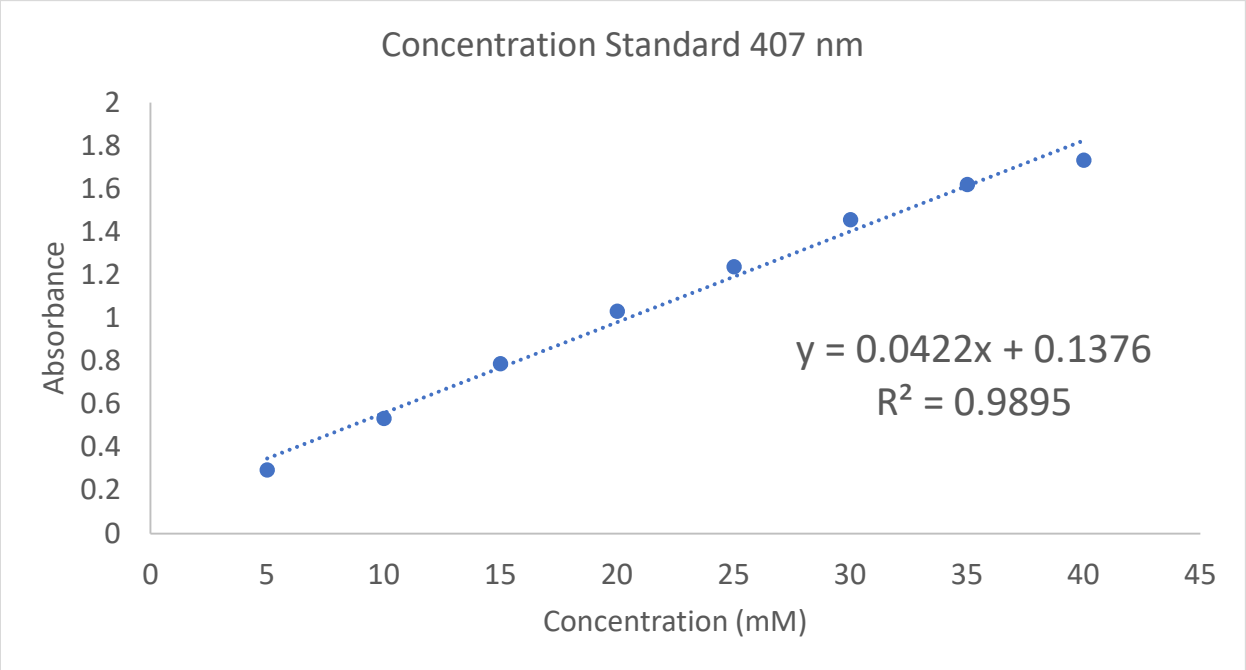

Figure 2.13. Absorbance at 407 nm was used to build a concentration standard for H_2O_2 concentration in solution

Table 2.1. Hydrogen peroxide concentration change before and after flowing through the chamber as a function of flow rate and concentration

Change in concentration after flow				
		Flow rate		
		.005 mL/min	.01 mL/min	.02 mL/min
Initial peroxide concentration	5 mM	2.021	-0.156	-0.0189
	20 mM	2.512	-1.735	1.699
	35 mM	1.372	1.777	-3.413

2.4 Immune Cell Culture

Section 2.3 showed that the microfluidic platform can be used to maintain a consistent hydrogen peroxide concentration to replicate the heated saline/hydrogen peroxide aging method of accelerated aging. In section 2.1, the idea of using immune cell-generated reactive oxygen as an alternative to hydrogen peroxide was introduced. For this method, instead of aging with hydrogen peroxide, neural implants will be attacked by reactive oxygen species generated by immune cells. This section describes the cells chosen, their handling methods, and the validation of the reactive oxygen they generate.

J774a.1 cells were chosen for the immune cells in the microfluidic bioreactor. J774a.1 is an adherent mouse monocyte cell line. These cells were chosen because they are immune cells that are able to repeatedly generate reactive oxygen and they adhere to the microfluidic chamber surface. These features are critical as non-adherent cells would be flushed from the chamber upon cell culture media replacement and repeat activation is essential to achieve acceleration of the reactive oxygen attack. Cells were cultured in 10% FBS DMEM complete media. Upon delivery, the cell vial was removed from dry ice and placed directly into a vapor phase liquid nitrogen storage vessel (Dewar with aluminum cryogenic vial cane). The cells were thawed according to ATCC procedure. Upon removal, cells were thawed in a 37 °C bath for 2-3 minutes. Under antiseptic conditions and in a biosafety hood, the cell vial contents were emptied into a 12 mL centrifuge tube with 9 mL of complete cell culture media. The tube was centrifuged for 8 minutes at 125 x g. The supernatant was removed with an autopipette, and the cell bundle was resuspended and transferred to a 100 mm tissue culture polystyrene dish with 12 mL of complete media. Reculturing was performed by removing media from the dish with an autopipette, adding 2 mL of fresh complete media, scraping cells with a sterile cell scraper, and transferring scraped cells to a new dish with 12 mL of fresh complete media. Reculturing was done at a 10:1 ratio. To refreeze cells for later use, a second dish was prepared during the reculturing step. Once cells were confluent in this dish, the media was removed and replaced with 5% DMSO complete media. The cells in the DMSO media were then placed into a cryo tube. The cryo tube was placed in a Styrofoam cell freezer and

stored at -80 °C overnight. The next day, the cryo tube was placed into the vapor phase liquid nitrogen storage vessel.

For any experiments involving microfluidic cell culture, microfluidic chambers were sterilized for 20 minutes with UV C light. After sterilization, the microfluidic chamber is placed into a biosafety hood. During the reculturing step of dish cell culture, 100 µL of cells suspended in cell culture media at a density of 3.5-4.5 x 10^6 cells/mL were injected into the microfluidic bioreactor using a micropipette. The microfluidic chamber was then placed in the incubator.

2.4.1 Cell Counting

Cell density was characterized using several methods: hemacytometer, coulter cell counter, and image-based visual cell counting. The hemocytometer and coulter counter methods both require a representative volume of solution for measurement. Due to the adherent nature of the cell lines, removing viable cells from the microfluidic chamber was difficult. Therefore, representative solution volumes are only accurate when cells are first introduced to the chamber. In order to get more accurate cell counts as a function of time, image-based visual counting methods were used. For this method, a microscope image was taken of the microfluidic chamber with cells inside. The image was then imported into the CellProfiler software shown in figure 2.14. The area of the image and of the entire chamber is known so the estimated total cell count in the chamber can be calculated assuming a uniform distribution of cells. In this work, cell counts in microfluidic chambers were determined using CellProfiler and cell counts before loading cells into microfluidic chambers were determined primarily using hemocytometry.

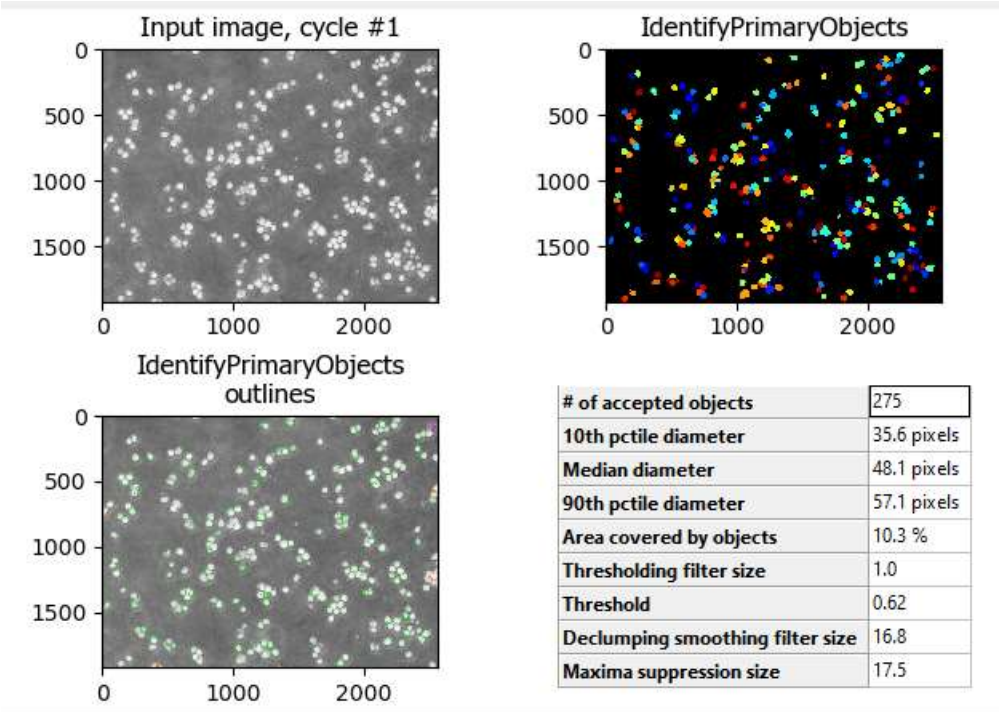

Figure 2.14. CellProfiler software used to count cells in microfluidic device

2.4.2 Amperometry

Amperometry has been used in cell culture to measure reactive oxygen species generated by immune cells [3]. For this method, a 3-electrode approach was used. Pt was used for the counter and working electrodes. Ag/AgCl was used for the reference electrode. J774a.1 cells were stimulated via micropipette with varying concentrations of PMA in serum-free DMEM. During measurement, a constant voltage of .2 V was applied on the chamber. 50 µL of PMA/serum-free DMEM was introduced into the chamber repeatedly. The charge generated per activation was recorded and compared across PMA concentrations. Cells were seeded at a consistent density of 3.5-4.5 x 10^6 /mL. Figure 2.15 shows the signal generated by repeated stimulating J774a.1 cells at a PMA concentration of 100 ng/mL. This process was repeated for PMA concentrations from 50 ng/mL to 200 ng/mL. The I-T curve was integrated for each activation event and plotted by activation number in figure 2.16. This data acts as a guide for the amount of reactive oxygen introduced to the neural implants when determining the acceleration factor achieved by immune cell accelerated aging. 100 ng/mL was chosen for accelerated aging experiments because it showed significant reactive oxygen generation without significant reduction as a function of number of activations, making it ideal for consistent, aggressive accelerated aging.

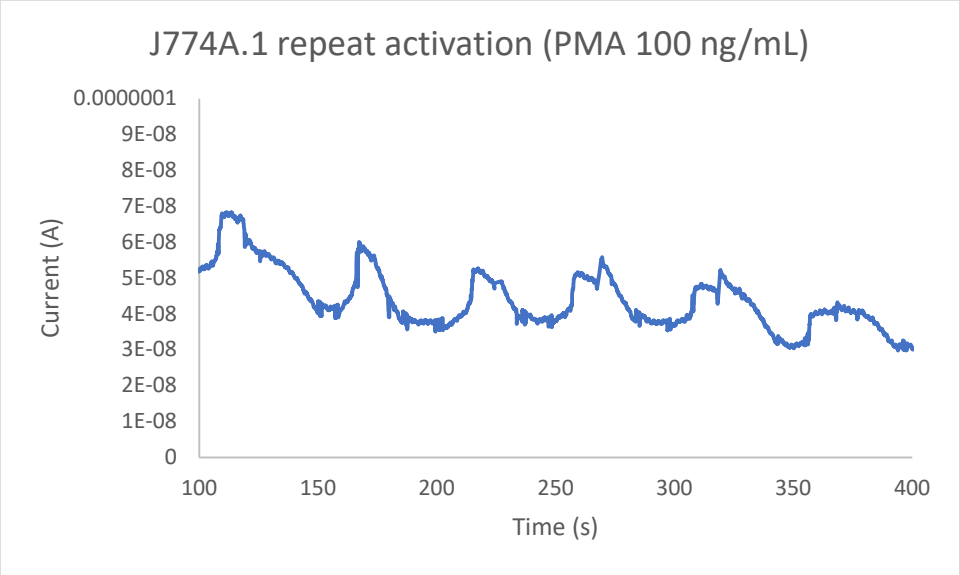

Figure 2.15. J774a.1 cells were repeatedly stimulated with PMA and the resulting current was measured.

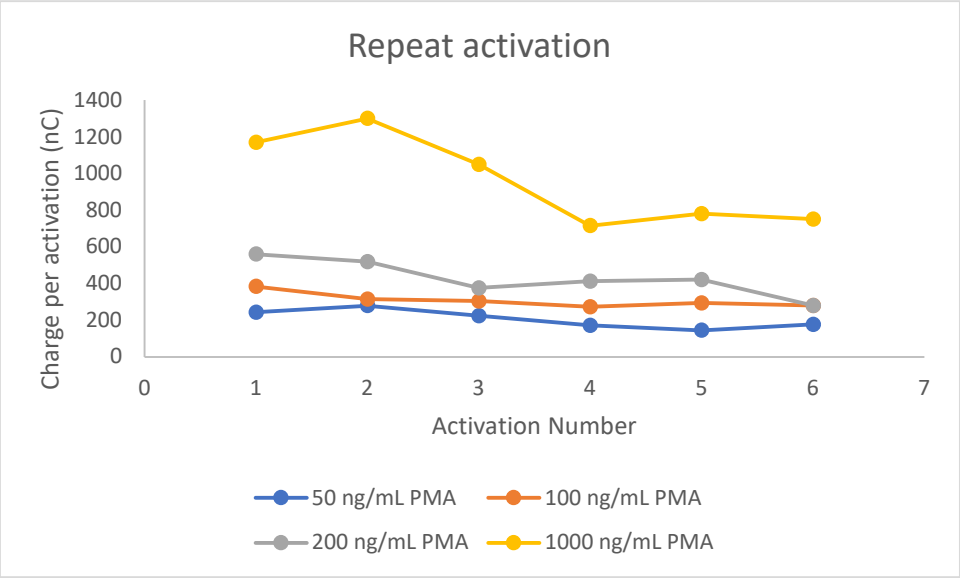

Figure 2.16. Total charge generated per activation was determined by integrating the I-T amperometry curve.

2.4.3 Fluorescence

Dihydroethidium was used to detect the presence of superoxide upon the introduction of PMA into the cell culture. Dihydroethidium was prepared according to [5]. Deoxygenated DMSO and Dihydroethidium were mixed to create a 20 mM stock solution in a glovebox in darkroom conditions. Stock solution was separated into 20 µL aliquots in amber vials and stored at -80 °C. For fluorescence measurements, a 10 µM solution of dihydroethidium in complete cell culture media was prepared by combining one 20 µL aliquot with 40 mL of complete cell culture media. Cells were cultured in the 10 µM solution for 30 minutes before being rinsed with complete media. Cells were imaged at 518/606 nm excitation and emission before and after introduction to PMA. Figure 2.17 shows the presence of dihydroethidium fluorescence after activation of the J774a.1 cells with PMA.

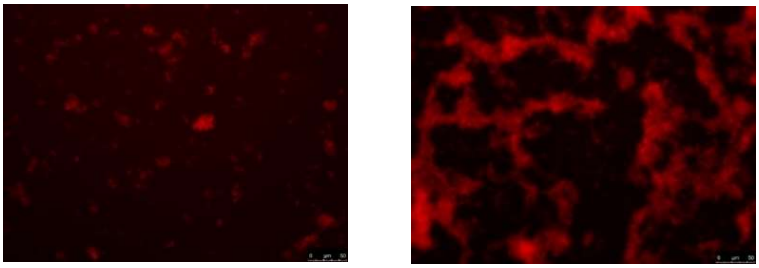

Figure 2.17. Dihydroethidium fluorescence of J774A.1 cells

Left: J774A.1 before activation with 100 ng/mL PMA

Right: J774A.1 after activation with 100 ng/mL PMA

2.4.4 Discussion

This section demonstrated the microfluidic platform's utility in immune cell-generated reactive oxygen accelerated aging. The microfluidic device can be sterilized prior to cell loading. Once cells are in the chamber, cell density can be quantified. The cells in this chamber can be stimulated to generate reactive oxygen that is quantifiable using amperometry and qualifiable as superoxide using fluorescence. These features provide a pathway towards representative immune response acceleration that is currently unavailable. In chapter 4, intracortical recording devices will be placed in the microfluidic bioreactor with J774a.1 cells. These cells will be stimulated to generate reactive oxygen and the degradation experienced by the neural probes will be characterized.

2.5 Conclusion

In this chapter, a microfluidic platform for accelerated aging was introduced. The chamber material selection, fabrication process, and design were described, an elliptical chamber fabricated from PDMS and glass using soft lithography. In addition, this platform was shown to be suitable for cell culture, immune cell reactive oxygen generation, and peroxide concentration control. The cell culture method, cell activation, and repeatability of microfluidic culture and activation were demonstrated.

2.6 References

1. Matthew G. Street, Cristin G. Welle, and Pavel A. Takmakov , "Automated reactive accelerated aging for rapid in vitro evaluation of neural implant performance", Review of Scientific Instruments 89, 094301 (2018) https://doi.org/10.1063/1.5024686
2. Rapid Prototyping of Arrayed Microfluidic Systems in Polystyrene for Cell-Based Assays. Edmond W. K. Young, Erwin Berthier, David J. Guckenberger, Eric Sackmann, Casey Lamers, Ivar Meyvantsson, Anna Huttenlocher, and David J. Beebe. Analytical Chemistry 2011 83 (4), 1408-1417. DOI: 10.1021/ac102897h
3. Amatore, Christian, Stéphane Arbault, Yong Chen, Cécile Crozatier, and Issa Tapsoba. "Electrochemical Detection in a Microfluidic Device of Oxidative Stress Generated by Macrophage Cells." Lab on a Chip 7, no. 2 (January 31, 2007): 233–38. https://doi.org/10.1039/B611569A.
4. K. Shen, A. Yau, S. Panchavati and M. M. Maharbiz, "An Automated System for Reactive Accelerated Aging of Implant Materials with In-Situ Testing," 2020 42nd Annual International Conference of the IEEE Engineering in Medicine & Biology Society (EMBC), 2020, pp. 4466-4469, doi: 10.1109/EMBC44109.2020.9176443.
5. Zielonka, J., Vasquez-Vivar, J. & Kalyanaraman, B. Detection of 2-hydroxyethidium in cellular systems: a unique marker product of superoxide and hydroethidine. Nat Protoc 3, 8–21 (2008). https://doi.org/10.1038/nprot.2007.473
6. Takmakov, Pavel, Kiersten Ruda, K. Scott Phillips, Irada S. Isayeva, Victor Krauthamer, and Cristin G. Welle. "Rapid Evaluation of the Durability of Cortical Neural Implants Using Accelerated Aging with Reactive Oxygen Species." Journal of Neural Engineering 12, no. 2 (January 2015): 026003. https://doi.org/10.1088/1741-2560/12/2/026003.
7. Hukins, D. W. L., A. Mahomed, and S. N. Kukureka. "Accelerated Aging for Testing Polymeric Biomaterials and Medical Devices." Medical Engineering & Physics, Special issue to commemorate the 30th anniversary of Medical Engineering & Physics, 30, no. 10 (December 1, 2008): 1270–74. https://doi.org/10.1016/j.medengphy.2008.06.001.
8. Zheng, X. Sally, Noah R. Snyder, Kevin Woeppel, Jenna H. Barengo, Xia Li, James Eles, Christi L. Kolarcik, and X. Tracy Cui. "A Superoxide Scavenging Coating for Improving Tissue Response to Neural Implants." Acta Biomaterialia 99 (November 1, 2019): 72–83. https://doi.org/10.1016/j.actbio.2019.08.032.
9. Whitesides, George M. "The Origins and the Future of Microfluidics." Nature 442, no. 7101 (July 2006): 368–73. https://doi.org/10.1038/nature05058.

Chapter 3. Peroxide-assisted reactive accelerated aging in a microfluidic device

3.1 Background

Accelerated aging is an extremely valuable tool for longevity assessment of many products. The ability to predict the functional lifetime of a device, material, or machine at a shortened timescale provides significant cost and time savings. In the case of biomedical implants, in vitro accelerated aging provides additional benefits over in vivo aging. The time and cost benefits are still present, but the additional resources required to maintain living creatures also need to be considered. Test subjects need space to live and qualified handlers. There is also significant experimental variation between test subjects. A particularly active or aggressive subject may cause wear on a device that would not be present in the majority of human patients. They may cause failure modes that are exceedingly rare in human patients. In chapter 1, some of these "mechanical" failure modes, like picking at the implant or smashing the implant into walls, were discussed. Due to the limitations of in vivo aging, there has been increasing interest in chronic durability testing for biomedical implants.

As previously discussed, the state of the art in vitro accelerated aging technique is submersion in heated phosphate buffered saline with persistent introduction of hydrogen peroxide. The increased temperature is intended to increase the rate of reaction via an Arrhenius relationship. The general rule used for determining the acceleration factor for biomedical polymers is the "double the rate of reaction for every 10°C hotter than the operating temperature" relationship from [1]. This same relationship will be used for peroxide aging in a microfluidic chamber in this work. Currently, 20-30 mM is the standard peroxide concentration used for accelerated aging. The acceleration factor achieved by this concentration of hydrogen peroxide is currently unknown and most report the temperature-based acceleration factor.

This chapter and the next are paired. This chapter will demonstrate the benefits of the microfluidic chamber for current state of the art aging methodology. The next will demonstrate the benefits of the platform for immune cell assisted accelerated aging. Both chapters will use nearly identical techniques for characterization of the neural probes. The goal of these chapters is to showcase the value in using microfluidics for accelerated aging of neural implants as well as to compare the two techniques and give an idea of how both techniques relate to what has been observed in other accelerated aging methods as well as in vivo aging. There is no good dataset on the chronic material performance of a range of neural implant designs in human test subjects. There are significant ethical, financial, and scale roadblocks to acquiring a dataset of this nature so a comparison with other imperfect techniques is appropriate.

This chapter acts as validation for existing acceleration techniques while expanding the experimental space to consider the effects of variable hydrogen peroxide concentrations. It also establishes a clear benchmark against which the immune cell aging technique may be measured. One issue with comparing accelerated aging results between studies is the minor deviations in experimental procedure, aging conditions, and sample handling. By keeping as many of these

variables constant as possible, a more direct comparison between aging techniques is possible. Additionally, by recreating the aging conditions used in previous studies [3,4,5] and observing similar results, the microfluidic chamber platform itself is removed as a source of experimental error when considering the results of the immune cell aging technique.

3.2 Experiment design

The goal of this chapter is twofold. First, this chapter aims to validate the microfluidic chamber as platform for accelerated aging by using the same aging techniques that have been demonstrate in bath-style aging experimental setups. Second, this chapter aims to understand the effect of varying hydrogen peroxide and temperature on implant degradation. This second point is valuable as a benchmark against which to measure the results of the immune cell aging technique and to motivate the need for aging techniques that can accelerate the foreign body response degradation experienced by electrodes in vivo.

To meet these two goals, a 4 factor, 2 level partial factorial experiment was designed. The 4 factors were aging time, implant material, hydrogen peroxide concentration, and aging temperature. These factors and their ranges were selected to produce data that could be compared to previous study results while expanding the scope of those studies[3,4,5]. The 2 implant styles were W and Pt/Ir probes, both insulated with Parylene C. These materials were selected to act as a model system for any style of implant. Tungsten probes experience dissolution in vivo[11,12]. Dissolution is a critical failure mechanism that should be avoided in vivo so any accelerated aging method should have the ability to accurately recreate the dissolution that occurs in vivo. At the same time, Pt/Ir probes do not experience any significant dissolution in vivo[14] and it is critical to evaluate a system that does not experience this failure mode as an accelerated aging method that does cause dissolution of Pt/Ir probes would not be a representative method. The aging time ranged from 1 week to 2 weeks. The tungsten probes were aged for 1 week and the Pt/Ir probes were aged for 2 weeks. These time points were chosen for several reasons. First, multiple time points provide time course data for any characterization techniques that require the implant to be removed from the microfluidic chamber (in this experiment, SEM and EDS). Second, previous experiments showed very little visible degradation of Pt/Ir probes after 1 week of aging but showed significant dissolution of W probes. A longer aging time for Pt/Ir probes may provide insight into degradation mechanisms that were not detectable after just 1 week of aging.

The hydrogen peroxide concentration was varied from 15 mM to 30 mM, and the temperature was varied from 67°C to 77°C. The peroxide and temperature conditions were consistent across materials systems. Using a 10°C difference between aging conditions should double the rate of degradation according to Hukins [1]. Therefore, enabling the Parylene C of the 1 week aged probes at 77°C to be directly compared to the 2 week probes at 67°C to test the validity of this assumption. This range was chosen to significantly increase the rate of degradation, 8x and 16x for 67°C and 77°C respectively, without crossing a critical phase transition of the polymer. One of the key assumptions of most accelerated aging techniques is that the material does not undergo any

phase transition or degradation mechanism during accelerated aging that is not present at its operating temperature. Parylene C is a chlorinated parylene that is frequently used in biomedical applications because it is biocompatible and can be conformally deposited as a coating in very thin films using vapor deposition at low temperatures. As with any polymer, there are a range of reported temperatures under which a phase transition may occur. The microprobes for life sciences catalog states that their probes are stable under 150°C sterilization for a short time. [6] The continuous service temperature of Parylene C has been reported to be 80°C [7] so 77°C was chosen to avoid any phase transitions or degradation mechanisms that may begin to occur at higher temperatures. A similar issue related to degradation mechanisms not present under operating conditions begins to arise when considering the concentration of hydrogen peroxide to use while aging. There may be a material that is an excellent moisture barrier or is highly corrosion resistant in saline solutions but is more sensitive to reactive oxygen attack. The reverse situation is also possible. The ability to scale up the reactive oxygen attack similar to the thermal acceleration is valuable. Currently, the prevailing aging method is to use the same hydrogen peroxide concentration across temperature conditions. This leaves space to address the interaction parameter of hydrogen peroxide and temperature. Therefore, this experiment compares 15 mM hydrogen peroxide in PBS with 30 mM hydrogen peroxide in PBS at both temperature conditions.

The final experimental design breaks the 4 factor, 2 level partial factorial experiment into 2 separate, simultaneous experimental designs. The first experiment is a 2 factor, 2 level full factorial experiment on W probes for 1 week. The full factorial space of 67°C/77°C and 15 mM/30 mM hydrogen peroxide was explored. The second experiment is a full factorial, 2 factor, 2 level experiment on Pt/Ir probes for 2 weeks consisting of 67°C/77°C and 15 mM/30 mM hydrogen peroxide aging. This is a total of 16 conditions. Each condition contains 4 samples in order to establish the statistical significance of the findings for a total of 48 probes.

3.2.1 Experimental Procedure

The microfluidic platform described in chapter 2 was used for peroxide-assisted reactive accelerated aging. The Microprobes for Life Sciences were removed from their packaging and immediately imaged using SEM and EDS to characterize their condition as received from the manufacturer. Any probes that were damaged were removed from the aging experiment. After initial imaging, the probes were placed in the microfluidic chamber with a counter electrode. This process was outlined in chapter 2 section 2.2.2. The microfluidic chamber was then filled with PBS and initial EIS measurements were taken to characterize the electrochemical impedance of the probe before aging. The probes were then connected to a syringe pump with the desired hydrogen peroxide concentration and placed on a hotplate at the desired temperature. The syringe pump was programmed to run continuously with a flow rate of .005 mL/min, as determined in chapter 2 section 2.3, using the same hotplate method shown in figure 2.11c. At the desired intervals, the chamber was removed from the hotplate and flushed with PBS without hydrogen peroxide for EIS measurements. After EIS measurement, the chamber was returned to the syringe pump/hotplate to continue aging. After the experiment ended, a final EIS measurement was recorded and then

the probe was removed from the chamber by cutting the chamber open with a scalpel, paying careful attention not to interact with the aged electrode tip. The probe was then gently rinsed in warm deionized water for 15 minutes to remove any salt deposits that may have formed. The probes were dried for 24 hours in a desiccator and then placed in a SEM for post aging SEM and EDS measurements.

3.3 Results and discussion

3.3.1 Scanning Electron Microscopy

Both secondary electron and backscatter electron microscopy were used to evaluate the integrity of the microprobes. Images were taken before aging began to ensure that electrodes were not compromised before the aging process. SEM was chosen to characterize electrode integrity because it is the most direct observation technique of visually observable electrode degradation. Broken tips, corroded electrodes, film cracking, and measurements of changes in electrode geometry are all detectable using SEM. This technique is commonly used to evaluate changes in electrodes for in vivo measurements, making it a good choice for identification of similarities and differences in electrode degradation between accelerated aging techniques and explanted electrodes aged in vivo. Most images were taken on uncoated electrodes, mounted using copper tape, at 15 KV with a working distance of 7.2 mm. Images were occasionally taken at 3 KV to minimize charging effects or 20 KV to intentionally induce charging in an attempt to visualize insulation cracking. Most SEM images were taken on the Zeiss 5000 SEM.

Figure 3.1 shows a selection of SEM images for the probes before and after aging. The Pt/Ir probes show very little visual degradation across all aging conditions. The W probes show full corrosion of the W after 1 week. This result is consistent with findings from in vivo studies of W and Pt/Ir probes[11,12,13]. Figure 3.2 shows one such in vivo study where Pt/Ir probes show little to no dissolution in 6 months of aging. Pt/Ir resists dissolution in the neural environments and shows the same resistance to dissolution in the heated saline/hydrogen peroxide aging chamber. Figure 3.3 is from a study of W probes aged in vivo for 7 days[11]. In this study, the tungsten recessed into the Parylene C insulation after just 7 days in vivo. This same dissolution and receding of tungsten probe tips was observed in probes that were aged in the heated saline/hydrogen peroxide chamber in figure 3.1. The SEM results suggest that heated saline and hydrogen peroxide are successful at reproducing the dissolution conditions experienced by electrodes in vivo.

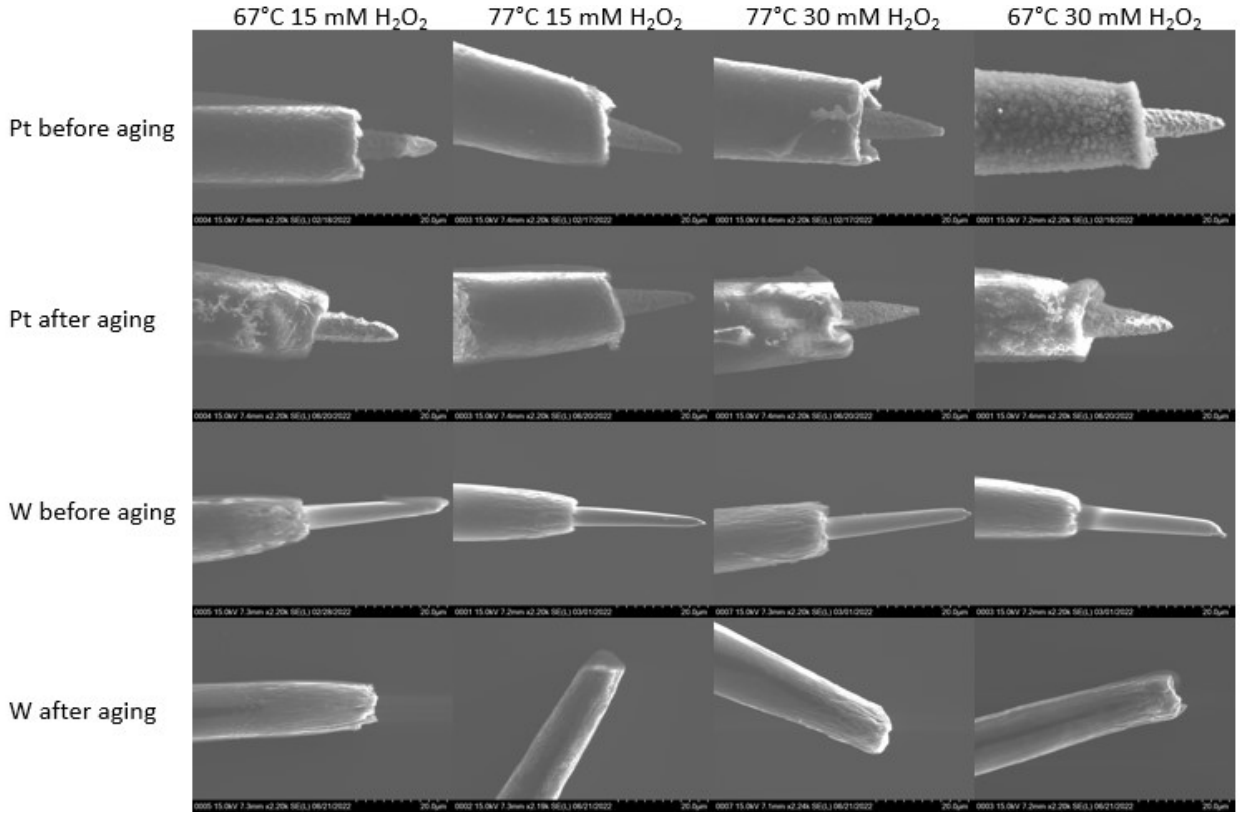

Figure 3.1 SEM images of W and Pt/Ir probes before and after aging at elevated temperatures and H_2O_2 conditions.

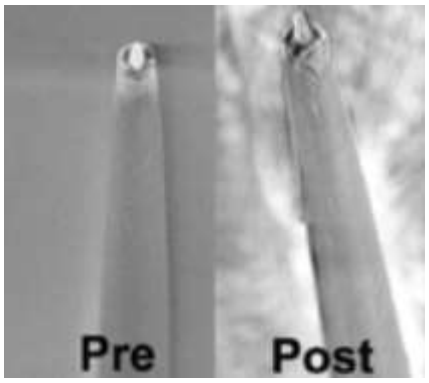

Figure 3.2 SEM images of Pt/Ir probes before and after 6 months of aging in vivo [13]

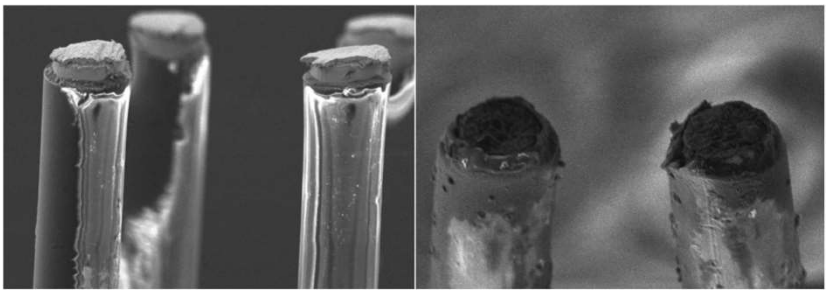

Figure 3.3 SEM images of tungsten probes. Left: Tungsten probe before implantation Right: Tungsten probe after 7 days in vivo[11]

3.3.2 Electrochemical impedance spectroscopy

Impedance is the primary in situ technique used in human trials of neural implants. The equipment available in the hospitals where these experiments are performed allows the experimenter to do impedance measurements, typically only at 1 kHz. 1 kHz impedance measurements have been used to attempt to ascertain the integrity of an implanted device in many studies [9,10]. The ubiquity of in situ impedance measurements in human clinical trials and their use for electrode integrity evaluation mean that an aging prediction technology that can give definitive information about the viability of an electrode without removing that electrode from the brain using only impedance data would be extremely valuable for rapid electrode integrity evaluation in vivo. There have been numerous studies showing why 1 kHz impedance is insufficient for electrode evaluation so most impedance analysis in the last several years has been on full frequency sweep impedance data[3,5].

This data has been represented many different ways, but the conclusions drawn from it have been largely specific to the electrode design analyzed. If a large enough dataset could be generated, there is potential that a machine learning algorithm could be an appropriate solution to evaluating which changes in this impedance sweep show critical implant failures. Until that dataset can be generated, fitting an equivalent circuit model to the impedance data is an attractive prospect. The equivalent circuit model compresses the full impedance sweep to just a few circuit parameters that have a physical meaning. The large samples sizes required to have any degree of confidence about reliability data can quickly snowball into huge datasets that are indecipherable. A single recording for a single day of a single sample is a frequency sweep across 61 individual frequencies. Each frequency will output a real and imaginary component of impedance. That is 122 data points for each measurement. In this experiment, there were 48 samples, and each sample was measured an average of 4 days. That is 23,424 datapoints for the EIS portion of this study. The study in chapter 4 has 80 samples. Using EIS as a tool for implant evaluation is not realistic without some sort of information compression. An equivalent circuit model, the Randles circuit, was used in this experiment to gain insight into the physical changes experienced by tungsten microprobes by treating them as model electrodes in solution.

Impedance was measured against a Ag/AgCl reference electrode for all EIS measurements. Recordings were taken from 1-10^6 Hz at 10 points per decade, with a 25 mV RMS excitation signal. Measurements were taken on the MG204 Autolab multichannel potentiostat with FRA32M module. The resulting measurements were then fit to a Randles equivalent circuit model using nonlinear least squares fitting code Zfit [8]. The components of the equivalent circuit model were used to compare the degradation of the probes.

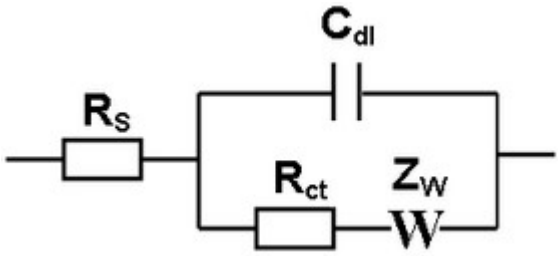

Figure 3.4 Randles equivalent circuit model used for EIS fitting[2]

The Randles equivalent circuit model shown in figure 3.4 has 4 main components. Rs is the solution resistance. This circuit parameter describes the resistance of the solution between the probe and the sensing wire. This resistance shouldn't vary dramatically with implant degradation as the solution (PBS) will not be changing significantly. In eq 1. for Rs, ρ is the solution resistivity, l is the distance between electrodes, and A is the area between electrodes.

Rct is the charge transfer resistance and Zw is the Warburg element, a constant phase element with a phase angle of 45°. These two elements describe the mass transport components of the circuit. The diffusion of any species present at the solution-electrode interface will contribute to the Warburg circuit component. The dissolution of the metal electrode will contribute to the charge transfer resistance. These circuit components should change as the implant degrades. Both components have an inverse relationship with exposed electrode area. Equations 2 and 3 describe the Warburg component. In these equations, Aw is the Warburg coefficient. ω is the frequency. R is the ideal gas constant. T is the temperature. F is the Faraday constant. n is the valency. D is the diffusion coefficient of the species. R and O signify the reduced and oxidized diffusion coefficients. C_O and C_R are the concentration of the reduced and oxidized species. A is the surface area of the exposed electrode. Eq. 4 describes the current density, i, associated with the charge transfer resistance. In this equation, i_0 is the exchange current density. C_O is the concentration of oxidant at the electrode surface. C_O* is the concentration of oxidant in the bulk. C_R is the concentration of reductant at the electrode surface. C_R* is the concentration of reactant in the bulk. η is overpotential. F is Faraday's constant. T is the temperature. R is the gas constant. α is the reaction order. N is the number of electrons involved. This equation details the concentration gradient current, which is helpful in understanding where this resistance comes from. However, eq. 5 and 6 show how Rct relates to exposed electrode area. Eq. 5 is ohms law: voltage equals current multiplied by resistance. Eq. 6 is the definition of current: current equals current density multiplied

by area. The inverse relationship between Rct and I is also an inverse relationship between Rct and exposed electrode area.

The last component is Cdl, the double layer capacitance. The double layer capacitance is the capacitance associated with the electrical double layer, a region that forms at the interface of the electrode and solution. The electrical double layer consists of two layers of charged species of opposite polarity. On the electrode interface, the charged species are electrons. In the electrolyte, the charged species are ions. The result of this double layer is a single layer of solution molecules that acts as a dielectric between the two oppositely charged layers, completing the conditions required for a capacitance to form. The double layer capacitance will change as the implant degrades. An increase in exposed electrode area should correspond to an increase in double layer capacitance. Eq. 7 shows that the double layer capacitance depends on ε the permittivity, A the exposed electrode area, and D the thickness of the double layer.

$$R_S = \rho \frac{l}{A} \quad (1)$$

$$Zw = \frac{Aw}{\sqrt{\omega}} + \frac{Aw}{j\sqrt{\omega}} \quad (2)$$

$$Aw = \frac{RT}{An^2F^2\sqrt{2}}\left(\frac{1}{D_O^{1/2}C_O} + \frac{1}{D_R^{1/2}C_R}\right) \quad (3)$$

$$i = i_0\left(\frac{C_0}{C_{0*}}\exp\left(\frac{\alpha nF\eta}{RT}\right) - \frac{C_R}{C_{R*}}\exp\left(\frac{-(1-\alpha)nF\eta}{RT}\right)\right) \quad (4)$$

$$Rct = V/I \quad (5)$$

$$I = i * A \quad (6)$$

$$Cdl = \varepsilon A/D \quad (7)$$

The linear relationship between double layer capacitance and electrode area shown in eq 7. is used to convert changes in double layer capacitance to changes in area for in situ electrode area measurements. Ideally, area measurements would be taken at regular intervals during the aging process using SEM. However, the time required to image every electrode every day using SEM is unsuitable for scaling the implant characterization process to the large sample sizes required for statistically significant conclusions to be drawn from the data. The relationship between double layer capacitance and exposed electrode area was determined by comparing measured double layer capacitance values from aged tungsten probes to SEM images of the electrode tips of those same probes. This trend is shown in figure 3.5a and indicates that measuring double layer capacitance is a viable strategy for exposed electrode area prediction.

In eq. 2-7, care was taken to describe how each component of the Randles circuit relates to exposed electrode area. The “model” data points shown in figures 3.5b and 3.5c show how the charge transfer resistance and Warburg coefficient would change with exposed electrode area if all other factors affecting these circuit components were held constant. During the aging process for

each probe plotted in figures 3.5b and 3.5c, the tungsten electrode tip dissolved to some degree. This dissolution process will cause changes in the concentrations of the reducing and oxidizing species at the electrode tip, making exposed electrode area just one of many relevant factors influencing the charge transfer resistance and Warburg coefficient that will change with electrode aging. As dissolution of the electrode occurs, the C_O, C_R, C_O*, C_R*, and even the diffusion coefficients are likely to change. The solution near the electrode tip will experience an increase in W ions, reducing the driving force for dissolution of the tip as well as the concentration gradient driving ionic current in this region. Additionally, any intermediate layers formed at the electrode surface in the process of aging will change the diffusion coefficients. As a result of these changes, the charge transfer resistance fit, and Warburg coefficient fit as a function of exposed electrode area are poor in figures 3.5b and 3.5c. As will be discussed later, the results of the multiday, multifactorial experiment described in figures 3.7 and 3.8 also show that the electrode area change experienced by tungsten electrodes was not the dominant factor in determining the change in charge transfer resistance and Warburg coefficient. Therefore, these circuit components are reported but will not be used to evaluate changes exposed electrode area.

Figures 3.6-3.9 show the results of the multiday, multifactorial heated saline/hydrogen peroxide aging experiment. Figure 3.6 shows the double layer capacitance trend for tungsten probes over 2 days of aging. All conditions showed a significant reduction in double layer capacitance after 1 day of aging. This data was normalized to the initial capacitance value for each sample in figure 3.7. The y-axis on this plot is unitless and represents the fractional loss of capacitance per day. Importantly, it was shown in eq. 7 that the area of the electrode-solution interface varies directly with the double layer capacitance value, Cdl $\propto$ A. Therefore, the y-axis on figure 3.7 can also be thought of as area/area initial. This relationship shows the rate of reduction in electrode area.

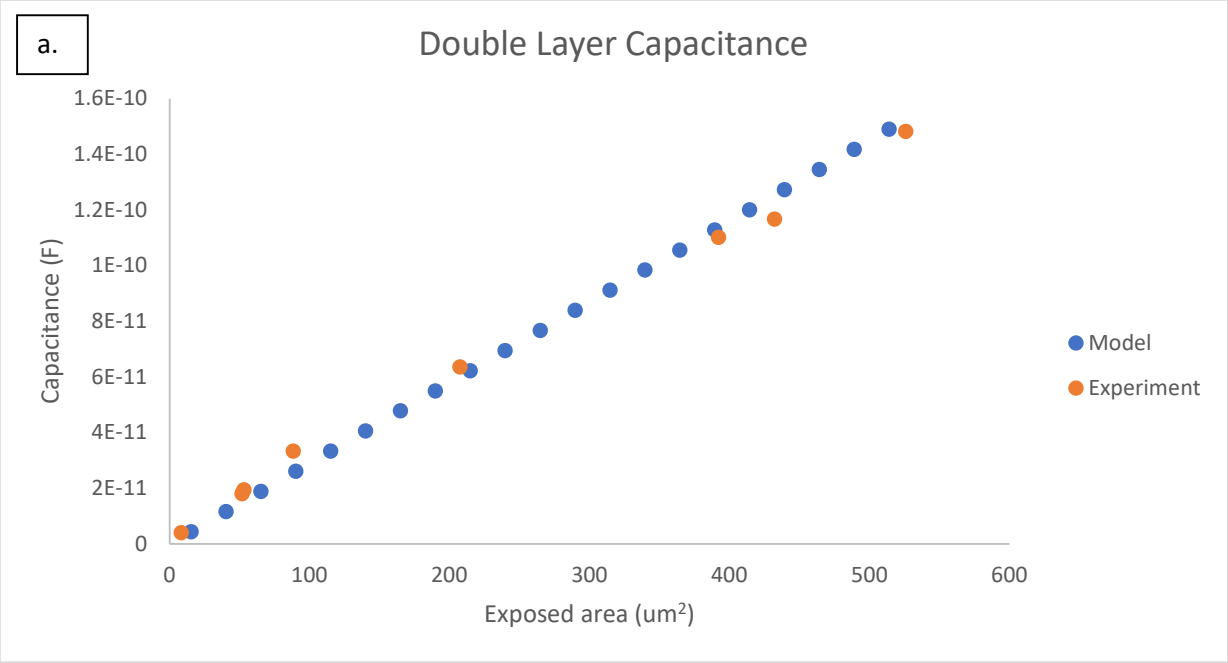

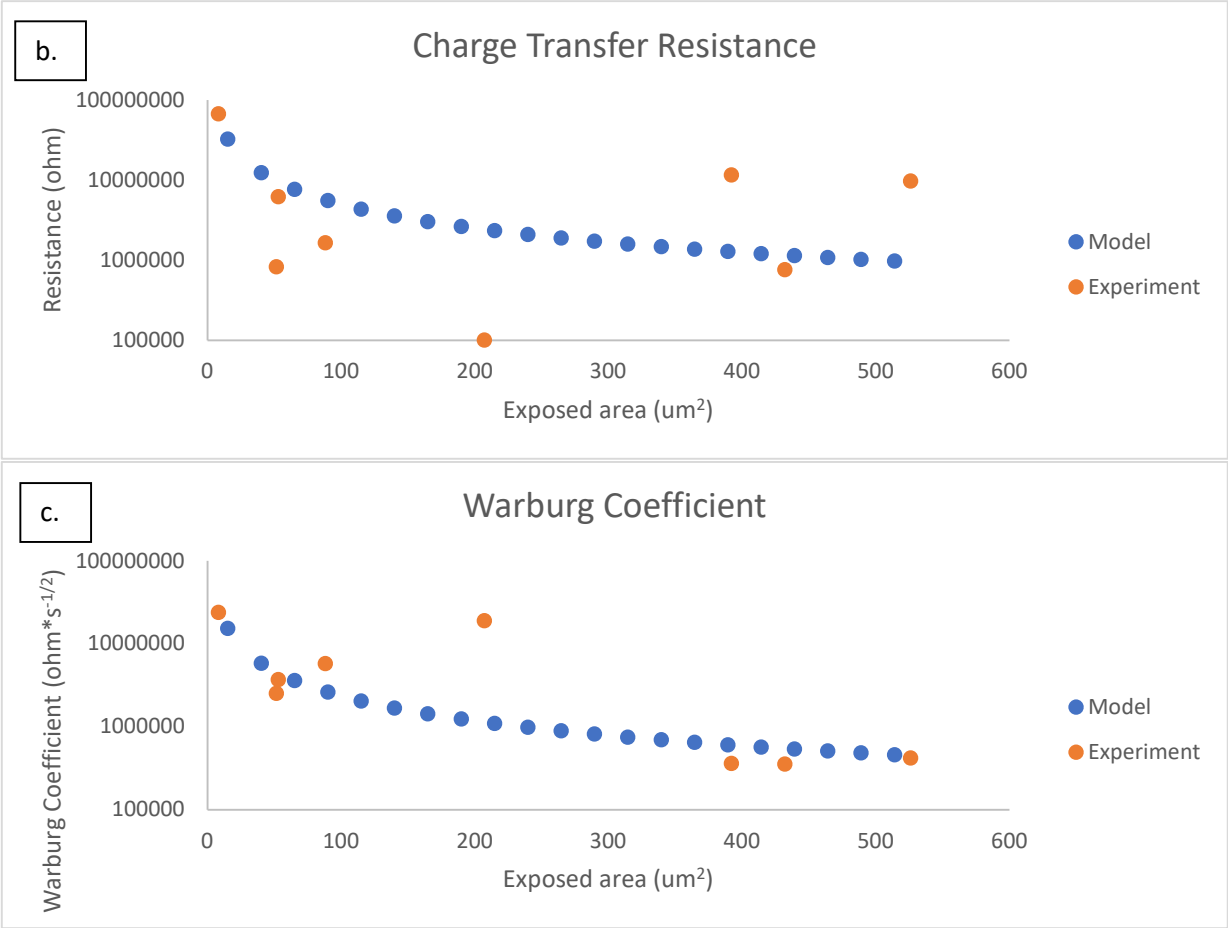

Figure 3.5 a. Double layer capacitance fit for tungsten microprobe EIS data as a function of exposed electrode area. b. Charge transfer resistance fit for tungsten microprobe EIS data as a function of exposed electrode area. c. Warburg coefficient fit for tungsten microprobe EIS data as a function of exposed electrode area

In the case of hydrogen peroxide-assisted heated PBS aging of W, the rate of corrosion is fast enough that the entire exposed area is corroded in 1 day at all conditions. Each condition shows a non-zero capacitance in its fully corroded state. This capacitance arises from the solution reaching the receded electrode by penetrating the open end of the Parylene C. The capacitance in this case is determined by the circular area of tungsten at the bottom of the Parylene C "cup". The open ended Parylene C can be seen in figures 3.1 and 3.3.

Figure 3.8 and 3.9 show the charge transfer resistance and Warburg coefficient as a function of time for W probes. Earlier in this section, it was hypothesized that a reduction in electrode area would lead to an increase in both of these circuit components if all other variables remained constant. In figure 3.5, the experimental data did not show a strong correlation with the predicted data, suggesting that other variables were affecting the Rct and Zw. This trend continued when analyzing the EIS data from the multiday, multifactorial experiment. No trend can be predicted with confidence from figure 3.8 or 3.9. Figure 3.1 shows the area of the exposed electrode visually

decreasing for tungsten probes, indicating that the impedance measurements are likely influenced by changes in the local environment of the electrode.

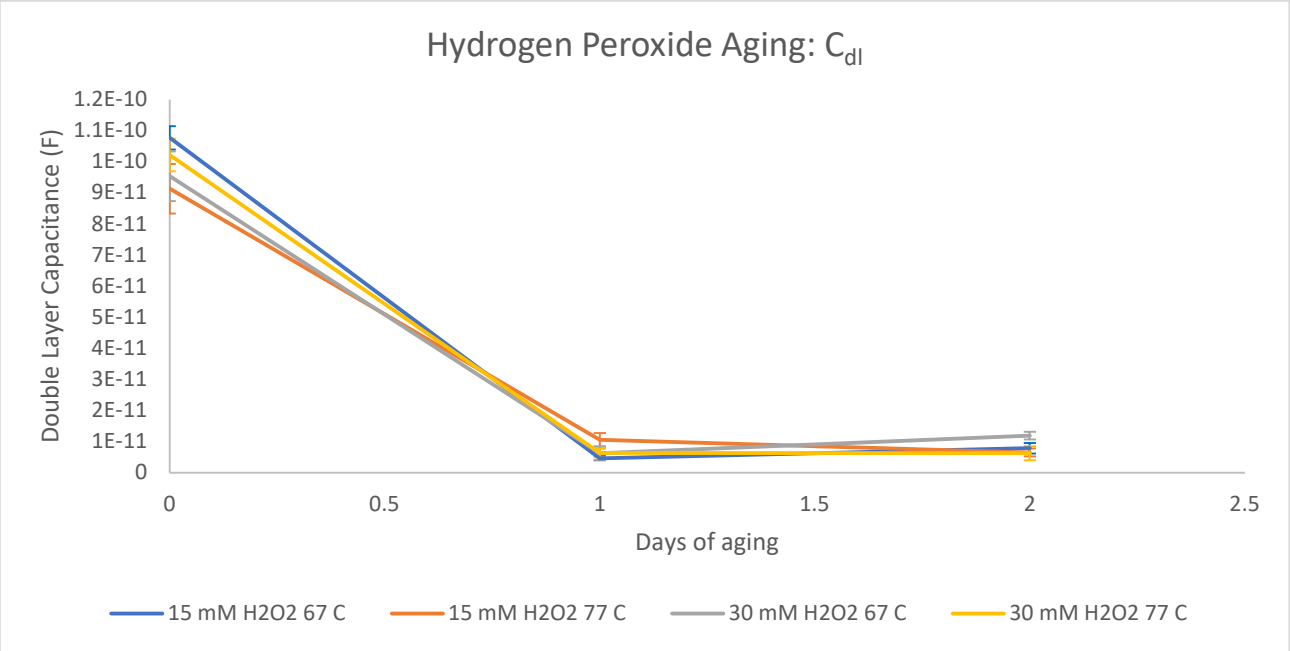

Figure 3.6 Double layer capacitance trend over time for W microprobes

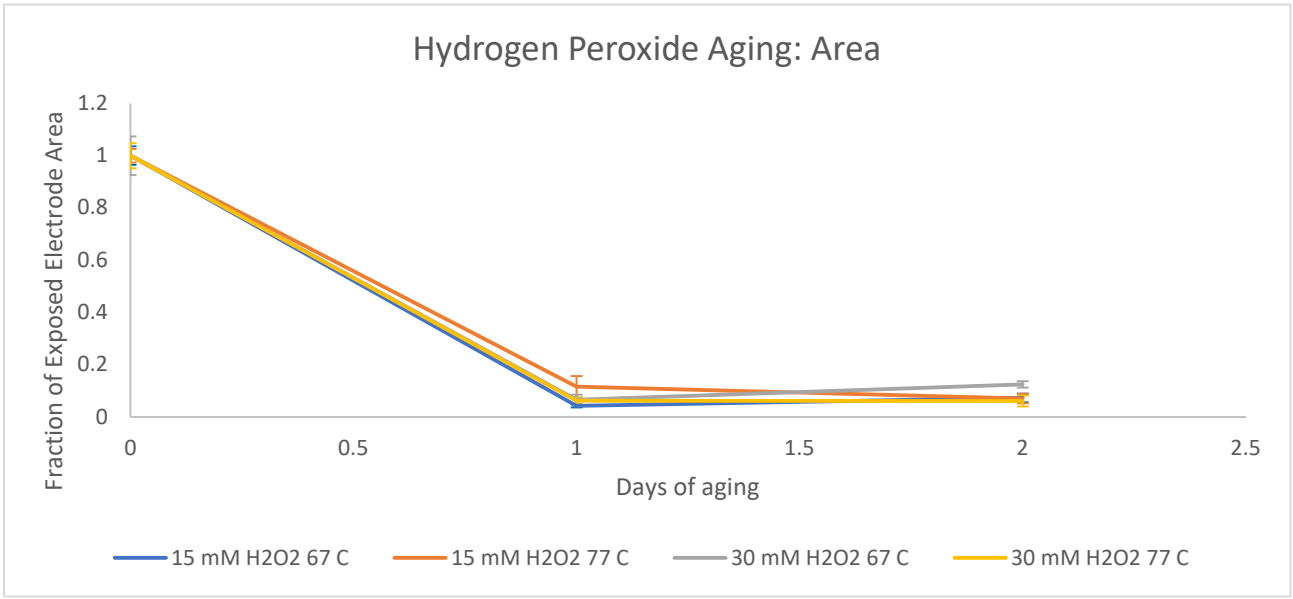

Figure 3.7 Normalized double layer capacitance trend over time for W microprobes normalized to the initial capacitance value. Y-axis is reported as "exposed electrode area" because Cdl $\propto A$ through eq. 7.

One possible explanation for this response is the presence of electrode dissolution under measurement. While effort was made to remove hydrogen peroxide from the chamber before measurement, there is a risk that the PBS flush was unable to remove all the hydrogen peroxide from the chamber, causing measurements to be taken under more aggressive corrosion conditions

than expected from pure PBS. Included hydrogen peroxide is more likely to affect mass transport components than double layer capacitance calculations as double layer capacitance depends only on the area, thickness, and permittivity of the double layer, none of which will change dramatically upon the inclusion of a low concentration of hydrogen peroxide whereas an increased corrosion condition would manifest itself in variable mass transport coefficients that dominate changes in charge transfer resistance and Warburg coefficient.

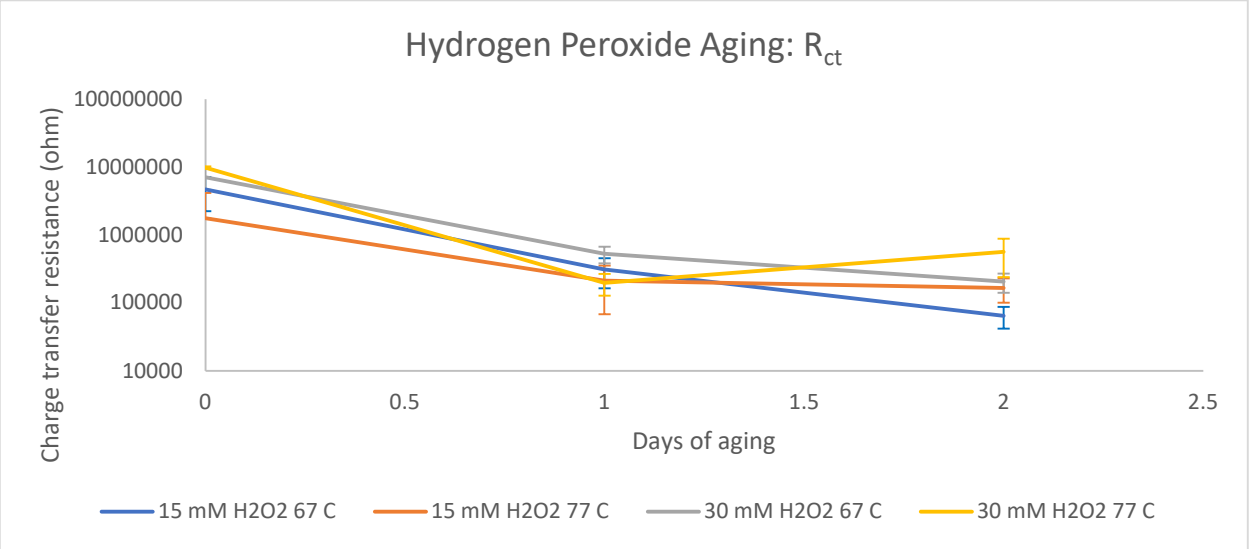

Figure 3.8 Charge transfer resistance trend over time for W microprobes

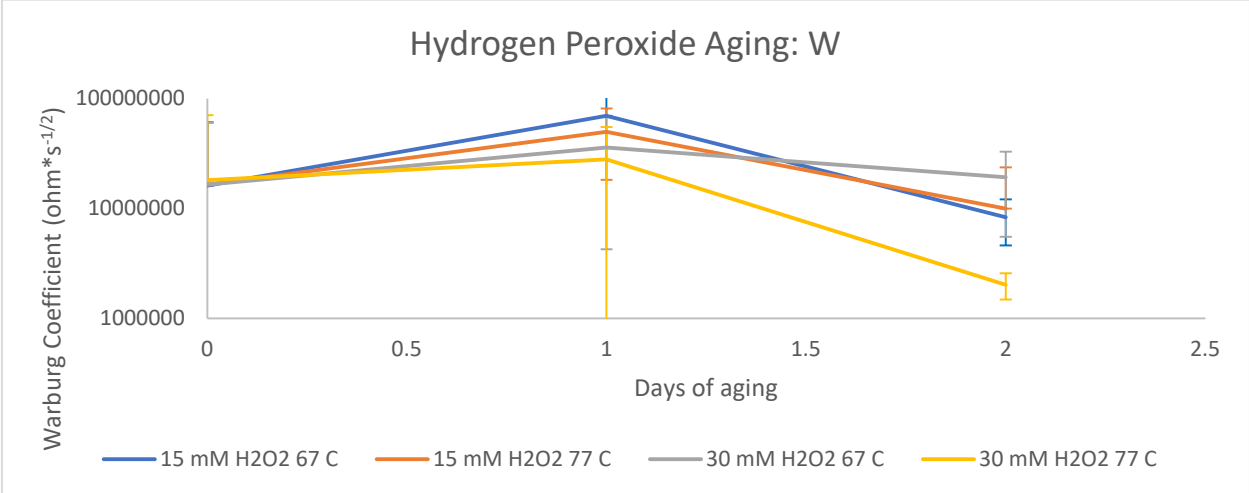

Figure 3.9 Warburg coefficient trend over time for W microprobes

3.3.3 Energy Dispersive X-ray Spectroscopy

SEM and EIS measurements in sections 3.3.1 and 3.3.2 were able to measure the dissolution of tungsten probes. However, neither of these techniques detected degradation of the Parylene C insulation or Pt/Ir electrodes. As shown in figure 3.2, no degradation of Pt/Ir is expected during in vivo aging. The absence of detectable Pt/Ir degradation in heated saline/hydrogen peroxide aged probes indicates that this technique isn't causing a nonrepresentative degradation mechanism.

However, Parylene C has been shown to experience degradation in vivo in the form of reactive oxygen-induced polymer chain scission, a process where oxygen radicals attack polymer bonds, cleaving them and forming C=O bonds, breaking the polymer chain and weakening the polymer film. This degradation mechanism can eventually lead to insulation failure due to delamination or pinhole formation. Semiquantitative EDS has been used to evaluate the degree of reactive oxygen-induced polymer chain scission experienced by Parylene C films implanted in vivo[4]. EDS measurements do not give absolute elemental concentrations, but instead give relative values. For this data, the y-axis is reported as "oxygen concentration relative to carbon concentration." The carbon concentration of the film is assumed to be constant in this technique so cleaning of the electrodes is important to remove any carbon that may have attached during the aging process. EDS scans were taken at a working distance of 12.2 mm, zoom of 3000x, and an operating voltage of 20 KV. EDS rectangular area scans were used for elemental characterization.

Figure 3.10 shows the average and standard error of the O:C ratio measured in the Parylene C insulation of all probe types. The 7 day experiments are W probes and the 14 day experiments are Pt/Ir probes. While the error bars are large for some of the data points, a few clear trends can be observed. The probes aged at 67°C show less oxygen uptake than the probes aged at 77°C with a p-value of <.05. The probes aged at 15 mM show less oxygen uptake than the probes aged at 30 mM with a p-value of <.05. The probes aged for 7 days show less oxygen uptake than the probes aged for 14 days with a p-value of .0669. While this p-value does not make the typical .05 cut off, it does suggest that time may be a statistically significant factor.

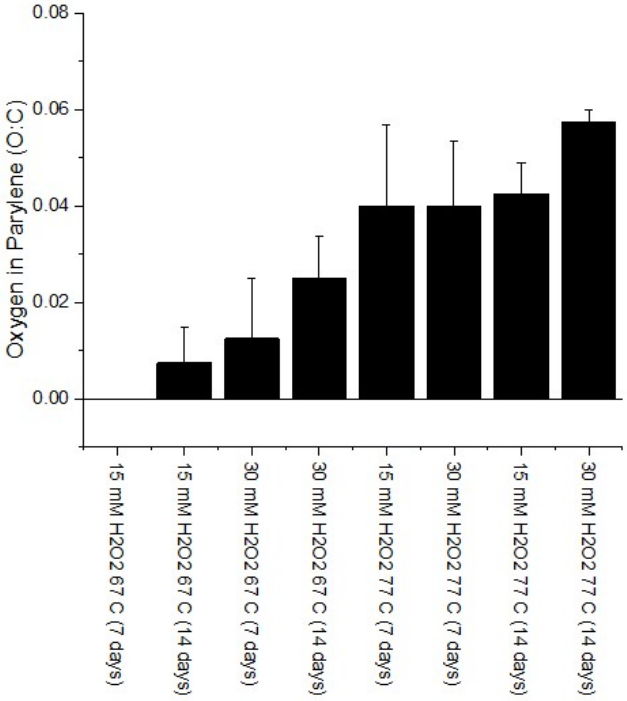

Figure 3.10 EDS scan average O:C ratios for Parylene C films aged in PBS+H_2O_2

The EDS measurements shown indicate something that most researchers expect, do not measure, and ignore: peroxide concentration affects the acceleration factor achieved in accelerated aging. A study of explanted, 3.25 years aged in vivo, Parylene C coated neural implants was characterized by semiquantitative EDS and found to have a O:C ratio of .08±.025[4], shown in figure 3.11. This indicates that the reactive oxygen attack of even the most aggressive condition, 77°C and 30 mM hydrogen peroxide for 2 weeks, does not cause as much polymer chain scission as 3.25 years of in vivo aging. This is consistent with the expected accelerated aging time of 32 weeks, ignoring any influence that hydrogen peroxide has on the acceleration factor. Additionally, in the [4] work, Parylene C coated implants aged at 20 mM peroxide at 67°C and 87°C were analyzed using semiquantitative EDS. Their results are consistent with this work, showing a O:C ratios between .02 and .06 and a dependance on aging temperature.

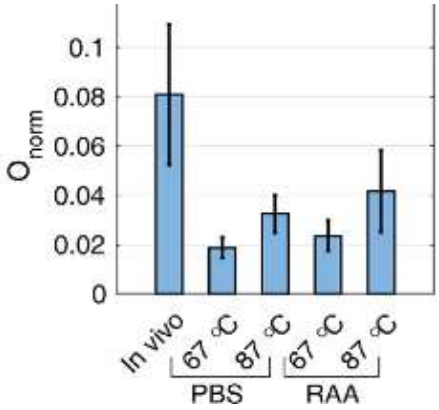

Figure 3.11 O_{norm} or O:C ratio is reported as a function of aging condition. In vivo samples were explanted after 3.25 years. PBS samples were aged at temperature for 28 days at 67°C and 7 days at 87°C. RAA samples underwent the same aging conditions with the addition of 20 mM hydrogen peroxide.[4]

3.4 Conclusion

This chapter demonstrated the utility of the microfluidic platform for PBS/hydrogen peroxide aging. The results of this study are consistent with those found in literature [3,4,5]. Tungsten corrodes quickly in heated saline/hydrogen peroxide environments, as observed by SEM and EIS data. Pt/Ir resists this type of attack. This was confirmed with SEM measurements. Additionally, Parylene C undergoes reactive oxygen-induced polymer chain scission, a result that was measured using EDS area scans of oxygen content in the Parylene C film. One key finding of this study is that the concentration of hydrogen peroxide used in aging is a statistically significant factor, suggesting a reevaluation of the acceleration factor used when adding hydrogen peroxide to heated saline baths. While the 2x/10°C rule is suitable for temperature-based acceleration, ignoring the role of hydrogen peroxide in acceleration is not appropriate. The next chapter outlines a pathway to a reactive oxygen acceleration factor, immune cell assisted accelerated aging.

3.5 References

1. Hukins, D. W. L., A. Mahomed, and S. N. Kukureka. “Accelerated Aging for Testing Polymeric Biomaterials and Medical Devices.” Medical Engineering & Physics, Special issue to commemorate the 30th anniversary of Medical Engineering & Physics, 30, no. 10 (December 1, 2008): 1270–74. https://doi.org/10.1016/j.medengphy.2008.06.001.

2. “File:Randles Circuit.Png.” In Wikipedia, March 21, 2012. https://en.wikipedia.org/w/index.php?title=File:Randles_circuit.png&oldid=483215956.

3. Street, Matthew G., Cristin G. Welle, and Pavel A. Takmakov. “Automated Reactive Accelerated Aging for Rapid in Vitro Evaluation of Neural Implant Performance.” Review of Scientific Instruments 89, no. 9 (September 2018): 094301. https://doi.org/10.1063/1.5024686.

4. Caldwell, Ryan, Matthew G. Street, Rohit Sharma, Pavel Takmakov, Brian Baker, and Loren Rieth. “Characterization of Parylene-C Degradation Mechanisms: In Vitro Reactive Accelerated Aging Model Compared to Multiyear in Vivo Implantation.” Biomaterials 232 (February 1, 2020): 119731. https://doi.org/10.1016/j.biomaterials.2019.119731.

5. Takmakov, Pavel, Kiersten Ruda, K. Scott Phillips, Irada S. Isayeva, Victor Krauthamer, and Cristin G. Welle. “Rapid Evaluation of the Durability of Cortical Neural Implants Using Accelerated Aging with Reactive Oxygen Species.” Journal of Neural Engineering 12, no. 2 (January 2015): 026003. https://doi.org/10.1088/1741-2560/12/2/026003.

6. Microprobes for Life Sciences Catalog. 2019

7. VSi Parylene C. “Parylene C Properties.” Accessed December 2, 2022. https://vsiParyleneC.com/ParyleneC-properties/.

8. Jean-Luc Dellis (2022). Zfit (https://www.mathworks.com/matlabcentral/fileexchange/19460-zfit), MATLAB Central File Exchange. Retrieved December 8, 2022.

9. Woeppel, Kevin, Christopher Hughes, Angelica J. Herrera, James R. Eles, Elizabeth C. Tyler-Kabara, Robert A. Gaunt, Jennifer L. Collinger, and Xinyan Tracy Cui. “Explant Analysis of Utah Electrode Arrays Implanted in Human Cortex for Brain-Computer-Interfaces.” Frontiers in Bioengineering and Biotechnology 9 (2021). https://www.frontiersin.org/articles/10.3389/fbioe.2021.759711.

10. Barrese, James C., Naveen Rao, Kaivon Paroo, Corey Triebwasser, Carlos Vargas-Irwin, Lachlan Franquemont, and John P. Donoghue. “Failure Mode Analysis of Silicon-Based Intracortical Microelectrode Arrays in Non-Human Primates.” Journal of Neural Engineering 10, no. 6 (November 2013): 066014. .

11. Streit, Wolfgang J., Qing-Shan Xue, Abhishek Prasad, Viswanath Sankar, Eric Knott, Aubrey Dyer, John R. Reynolds, Toshikazu Nishida, Gerald P. Shaw, and Justin C. Sanchez. “Electrode

Failure: Tissue, Electrical, and Material Responses." IEEE Pulse 3, no. 1 (January 2012): 30–33. https://doi.org/10.1109/MPUL.2011.2175632.

12. Prasad, Abhishek, Qing-Shan Xue, Viswanath Sankar, Toshikazu Nishida, Gerry Shaw, Wolfgang J. Streit, and Justin C. Sanchez. "Comprehensive Characterization and Failure Modes of Tungsten Microwire Arrays in Chronic Neural Implants." Journal of Neural Engineering 9, no. 5 (September 2012): 056015. https://doi.org/10.1088/1741-2560/9/5/056015.

13. Prasad, Abhishek, Qing-Shan Xue, Robert Dieme, Viswanath Sankar, Roxanne Mayrand, Toshikazu Nishida, Wolfgang Streit, and Justin Sanchez. "Abiotic-Biotic Characterization of Pt/Ir Microelectrode Arrays in Chronic Implants." Frontiers in Neuroengineering 7 (2014). https://www.frontiersin.org/articles/10.3389/fneng.2014.00002.

Chapter 4. Immune cell-assisted reactive accelerated aging in a microfluidic device

4.1 Background

The goal of accelerated aging is to predict device performance in real conditions at an accelerated rate. A key component of accelerated aging is that the aging process is representative. In the previous chapter, a heated PBS and hydrogen peroxide accelerated aging strategy was described. As previously discussed, hydrogen peroxide is not the only reactive species present during aging. The immune response generates other reactive species like superoxide (O_2-)[1]. In order to predict aging, the ability to generate reactive species from immune cells will be valuable. This chapter will describe the process of aging neural probes using reactive species generated by immune cells in vitro.

In chapter 2, the basis for this experiment was described. The activation of J774a.1 cells generates a quantifiable amount of charged species, measurable using amperometry. In the brain, reactive species are generated in the form of superoxide[1]. Dihydroethidium fluorescence was performed in chapter 2 to confirm the presence of superoxide upon activation of the J774a.1 cells used for accelerated aging. This chapter describes a large experiment evaluating the effects of different intensities of reactive oxygen attack on neural probes. The goal of this work is to propose an alternative acceleration mechanism to heated saline. Chapter 3 showed that the concentration of hydrogen peroxide used for aging affects the degree of reactive oxygen-induced polymer chain scission. It was hypothesized that by varying the reactive oxygen attack provided by immune cells, implant failure due to reactive oxygen attack could be accelerated. If such an acceleration could be achieved, it would serve as a valuable complement to the heated saline method, which is able to accelerate the portion of implant degradation that results from prolonged exposure to the saline environment of the brain.

The use of cells for accelerated aging is an unexplored field and this work is a first step in showing it as a viable method. The key to this method is the microfluidic platform that enables sterile handling of the aging chamber, a requirement for the maintenance of cell culture. As mentioned in chapter 2, the cell type used for this technique is a mouse cell line, J774a.1. This cell line is not brain specific or human, but it is adherent and able to repeatedly produce reactive oxygen, important features for its use in the repeat activation microfluidic bioreactor. Chapter 6 outlines potential alternative cell choices that may more accurately recreate the composition of the immune response present in the human brain.

The motivation behind using immune cells for accelerated aging is to provide a more representative immune response attack. The introduction of hydrogen peroxide into a heated PBS bath was a step towards a more representative attack, but it has been known that the oxygen species generated by immune cells and microglia are oxygen radicals before they are converted to hydrogen peroxide by enzymes like superoxide dismutase[1]. The degree to which the degradation of an implant is affected by the substitution of hydrogen peroxide for the range of oxygen radicals generated in vivo has not been well studied. Any accelerated aging technique attempts to predict

the dominant failure mechanisms present in the target environment. This ability of this platform to test both methods of aging in the same test chamber provides an avenue for researchers to compare the performance of their device under several acceleration schemes to determine which method most accurately recreates the degradation observed in vivo.

4.2 Experiment design

The goal of this experiment is to provide a pathway towards acceleration of the implant failure mechanisms caused by the immune response of the brain to intracortical devices. To this end, the main experiment of interest for immune cell accelerated aging was a 3 factor, multi-level partial factorial experiment. The 3 factors were aging time, implant material, and activation frequency. The aging time ranged from 2 days to 2 weeks, the 2 implant styles were W and Pt/Ir probes, both insulated with Parylene C, and the activation frequency was varied from 0 to 48 activations per day.

Previous weeklong experiments predicted that W probes would corrode completely after just a few days. Early versions of this experiment attempted on unoptimized chambers showed unreliable results as a function of input variables, but a consistent result was that impedance analysis predicted that W probes were corroding before day 3 of aging. Therefore, the first time condition for W probe aging was chosen to be 2 days of aging to attempt to visually observe the rate of corrosion using SEM. At the same time, there appeared to be very little impact on the Parylene C integrity after just 2 days so a second, more common in literature, time period of 1 week was chosen for W aging[3]. These early experiments showed almost no detectable degradation of Pt/Ir probes after 1 week. For this reason, a longer time period of 2 weeks was chosen for Pt/Ir probes. The second time period for Pt/Ir probes was 1 week. These time period selections targeted relevant time frames for each metal system while providing a large dataset of 1 week aged Parylene C to compare across metals to determine if electrode material influenced Parylene C degradation.

The 3 factor experimental design was divided into 2 separate experimental designs. The first experiment is a 2 factor, 2 level experiment on W probes. The full factorial space of 0/6/12/24/48 activations per day and 2 day/7 day aging was explored. The second experiment is a full factorial, 2 factor, 2 level experiment on Pt/Ir probes consisting of 0/6/12/24/48 activations per day and 7 day/14 day aging. This is a total of 20 conditions. Each condition contains 4 samples in order to establish the statistical significance of the findings for a total of 80 probes. The range of activation frequency was also selected by considering the results of preliminary experiments that suggested that the 0 activation condition caused significantly less degradation than the “1 activation per day” condition, but there was not much difference between “5 activations per day” and “10 activations per day”. By doubling the aging time and doubling the activation frequency, it is possible to distinguish whether the total number of activations was the only factor influencing device degradation by comparing the “6 activations over 2 weeks” condition with the “12 activations over 1 week” condition.

4.2.1 Experimental timeline

Day 1

1. Thaw J7741.a cells into 100 mm tissue culture polystyrene dish according to ATCC protocol

Day 2-4

1. Reculture J774a.1 cells until 80% confluent

Day 5

Microfluidic chambers were sterilized for 20 minutes with UV C light prior to cell culture. After sterilization, the microfluidic chambers were placed into a biosafety hood. All PVC tubing and connectors were sterilized with ethanol before use. The syringes were removed from sterile packaging in a sterile biosafety hood. The syringes were then filled with complete cell culture media with 100 ng/mL PMA. Next, the tubing was connected to the syringes. The syringes were then loaded on syringe pumps sitting on top of the incubator. The tubing was fed through the cord port in the side of the incubator. Cell culture media was pumped to the end of the tube before the tubing was connected to the microfluidic chamber. Figures 4.1 and 4.2 show the experimental set up for immune cell accelerated aging. Once the syringes were prepared, the procedure continued as follows:

1. Scrape J774a.1 cells into cell culture dish
2. Swirl dish to suspend cells
3. Using a micropipette, inject cells into microfluidic chamber
4. Place microfluidic chambers with cells in incubator at 37 °C 5% CO_2
5. Wait 4 hours for cells to attach
6. Record electrochemical impedance spectroscopy for day 0 of aging
7. Return chambers to incubator
8. Connect chamber to syringe pump containing PMA-cell culture medium using PVC tubing
9. Start syringe pump programming

Syringe pump programming:

1. Hold for 18 hours
2. Evenly space injections of 50 µL of PMA-cell culture medium over 4 hours (ex. For the 12 activations per day condition, cells were activated once every 20 minutes)
3. Repeat

Day 6

1. Replace media in microfluidic chamber with complete cell culture media
2. Record electrochemical impedance spectroscopy for day 1
3. Return cells to incubator
4. Connect chamber to syringe pump containing PMA-cell culture medium using PVC tubing

5. Start syringe pump programming

Day 7 until end of experiment

1. Repeat day 6, recording impedance at desired intervals

Figure 4.1 Syringe pumps were placed on top of incubator to avoid contamination of the chamber. Tubing was fed through the cord port in the side of the incubator.

Figure 4.2 Syringe pump tubing was connected to microfluidic chambers inside of the incubator. Microfluidic chambers were transported in tissue culture polystyrene dishes to reduce contamination.

After the experiment ended, a final EIS measurement was recorded and then the probe was removed from the chamber by cutting the chamber open with a scalpel, paying careful attention not to interact with the aged electrode tip. Each probe was then gently rinsed in warm deionized water for 15 minutes to remove any salt deposits that may have formed. The probes were dried for 24 hours in a desiccator and then placed in a SEM for post aging SEM and EDS measurements.

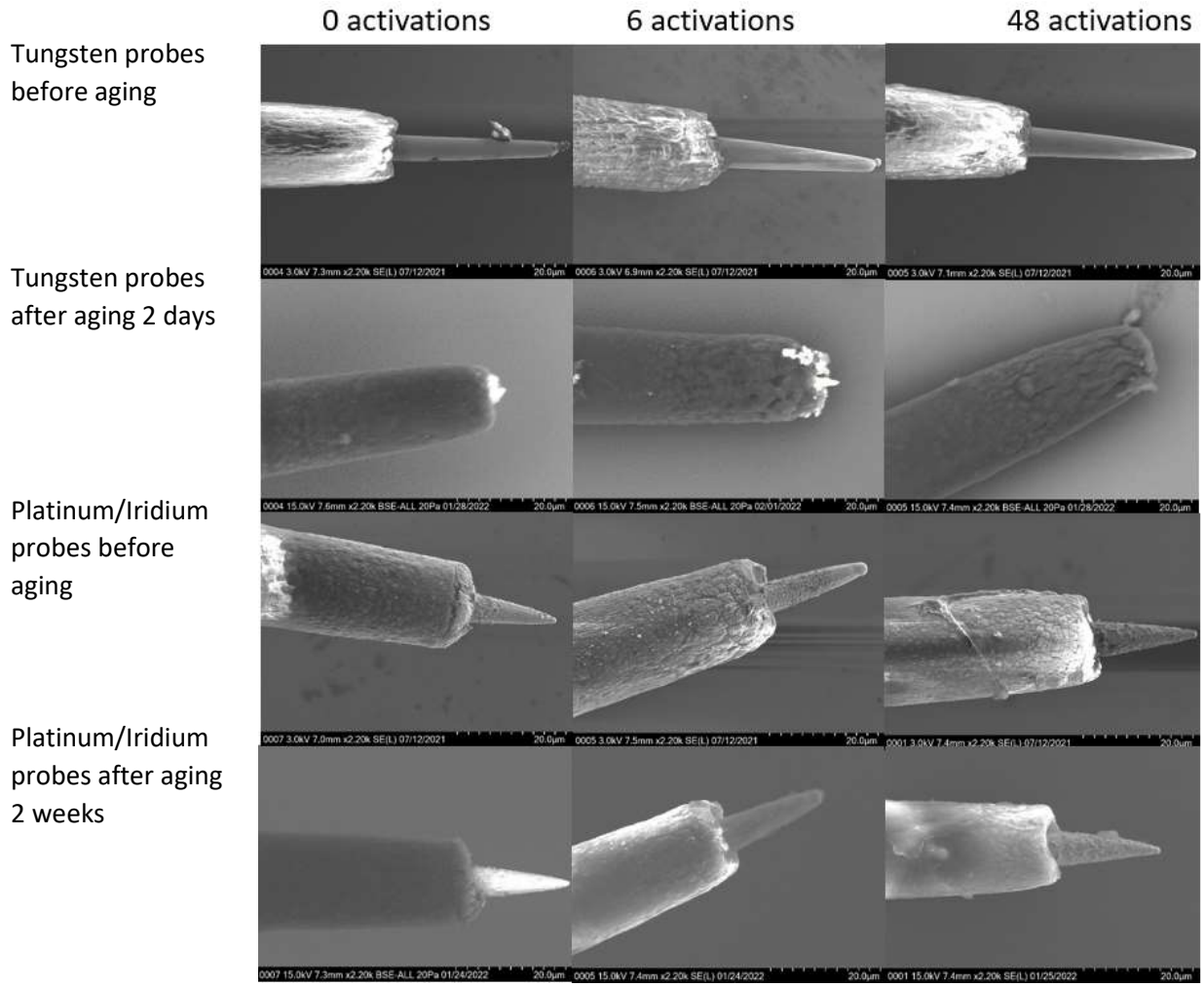

Figure 4.3 A selection of SEM images of W and Pt/Ir probes aged under varying J774a.1 activation conditions

4.3 Results and discussion

4.3.1 SEM

The predicted response to a reactive oxygen attack on tungsten probes is dissolution. Dissolution was observed in tungsten probes aged in hydrogen peroxide in figure 3.1 and in vivo in figure 3.3. In figure 4.3, a selection of SEM images show similar dissolution was observed visually in tungsten probes aged in the immune cell activation chamber. As was observed in the peroxide chamber and in vivo in figures 3.1 and 3.2 respectively, no dissolution occurred for the platinum/iridium probes. The immune cell accelerated aging method was able to accurately recreate the visual degradation observed in vivo. Of interest in figure 4.3 are the W probe after aging images. All W probes imaged after 2 days of aging at 24+ activations per day showed complete electrode dissolution, but O activation probes showed incomplete electrode dissolution. Only one of the four probes aged at 6 activations per day and one of the four probes aged at 12 activations per day showed incomplete dissolution. The dependance on activation frequency suggests that increasing immune cell activation increases the rate of W probe dissolution.

4.3.2 Electrochemical impedance spectroscopy

In chapter 3, EIS double layer capacitance data was used to estimate the reduction in exposed electrode area experienced by tungsten electrodes in a heated saline/hydrogen peroxide accelerated aging microfluidic chamber. The same method of area estimation is used in this section. Figure 4.4 shows the averaged double layer capacitance values for tungsten probes aged in J774a.1 cell-filled bioreactors over the course of 6 days. This figure shows a reduction in double layer capacitance over time, similar to what was observed in the hydrogen peroxide aging chambers in chapter 3. There is a clear trend in the rate of capacitance change as a function of activation frequency. As activation frequency increases, the capacitance decreases more quickly. Similar to section 3.3.2, this data was normalized to the capacitance value recorded on day 1 (figure 4.5). This unitless axis represents the change in double layer capacitance, but through the relation in equation 3.7, also represents the change in exposed electrode area. These plots suggest that increasing the frequency of J774a.1 cell activation increases the rate of corrosion of the exposed W electrode area. All electrodes corroded completely by day 6, settling at the same exposed electrode area, defined by the Parylene C “cup” described in section 3.3.2. Figure 4.6 includes data from both the 1 week and 2 day aging experiments normalized. Figure 4.6 contains 8 samples per datapoint and also suggests that increasing activation frequency increases the rate of corrosion of the exposed W tip. Figure 4.5 and 4.6 together show that the rate of tungsten dissolution experienced by the 0 activation condition is lower than for the 6 and 12 activation conditions which are lower than the 24 and 48 activation conditions. This data, in combination with the SEM images in figure 4.3 shows a clear acceleration of implant degradation that is achieved by increasing the rate of oxygen generation from J774a.1 cells. Figure 4.7 and 4.8 show the data for the charge transfer resistance and Warburg coefficients. This data, like the Rct and Warburg coefficient data from the hydrogen peroxide aging in chapter 3, shows no discernable

trend. In chapter 3, one explanation for the varying Rct and Warburg values was that measurements may have been occurring under active corrosion conditions. This explanation is even more likely to be true in the case of immune cell-based aging as these cells generate a small amount of reactive oxygen even without PMA stimulation.

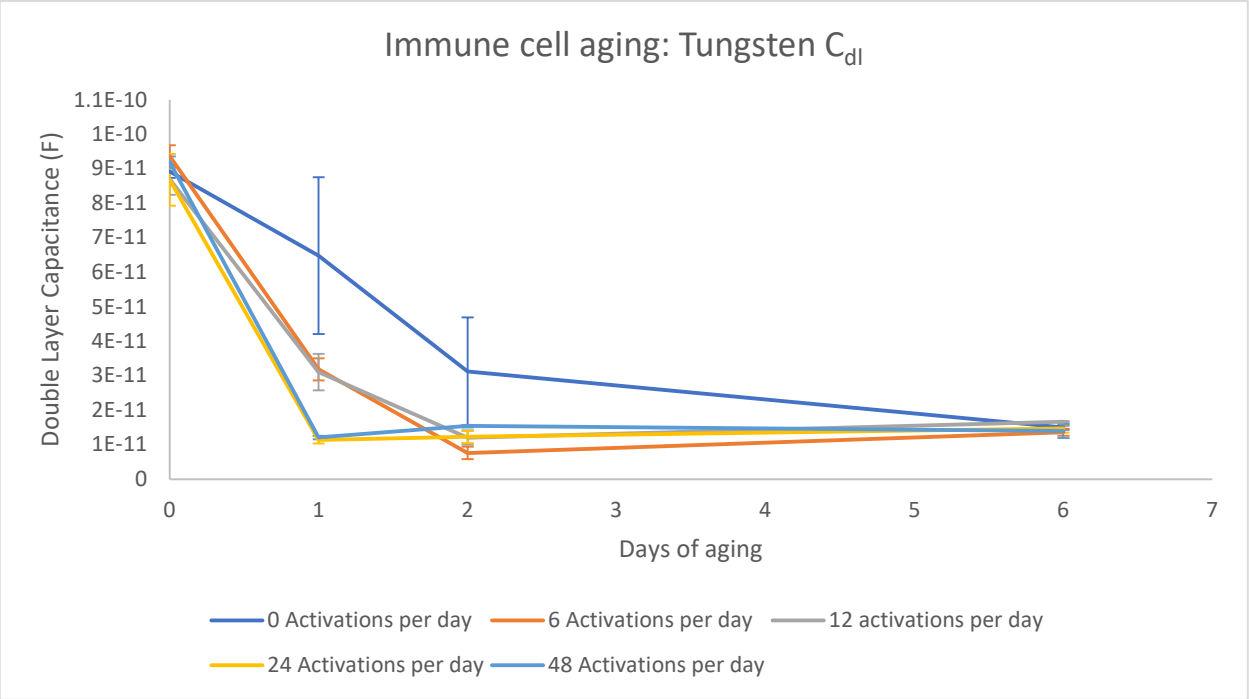

Figure 4.4 Double layer capacitance trend over time for W microprobes

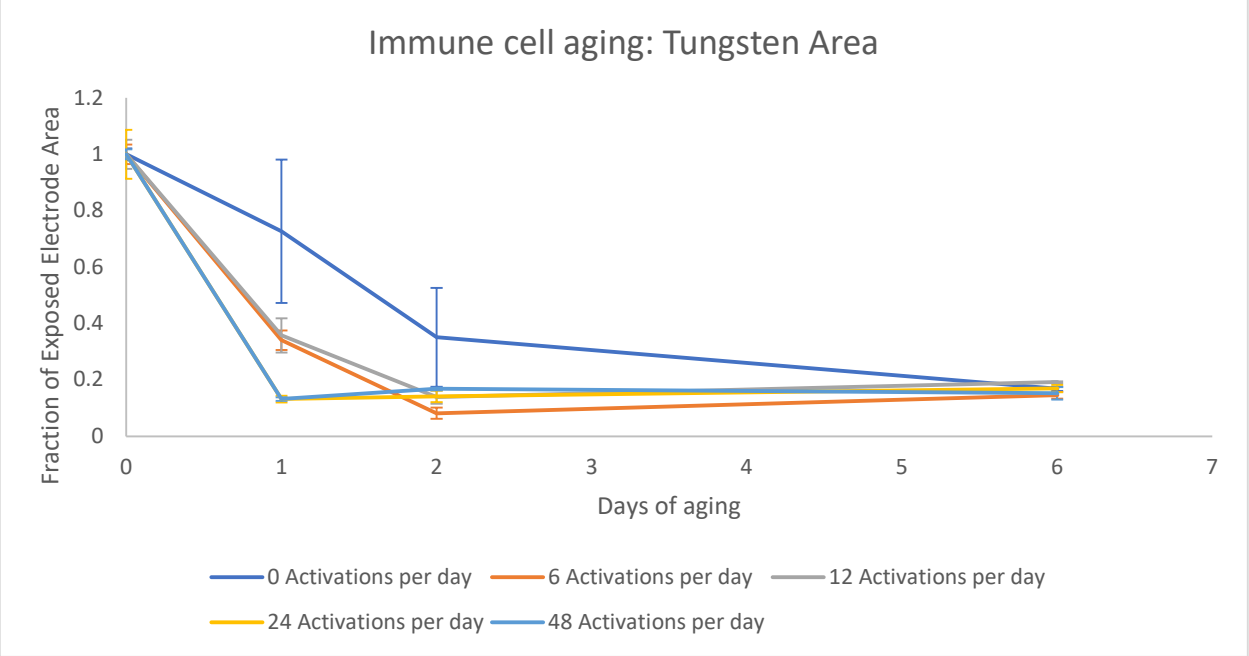

Figure 4.5 Normalized double layer capacitance trend over time for W microprobes

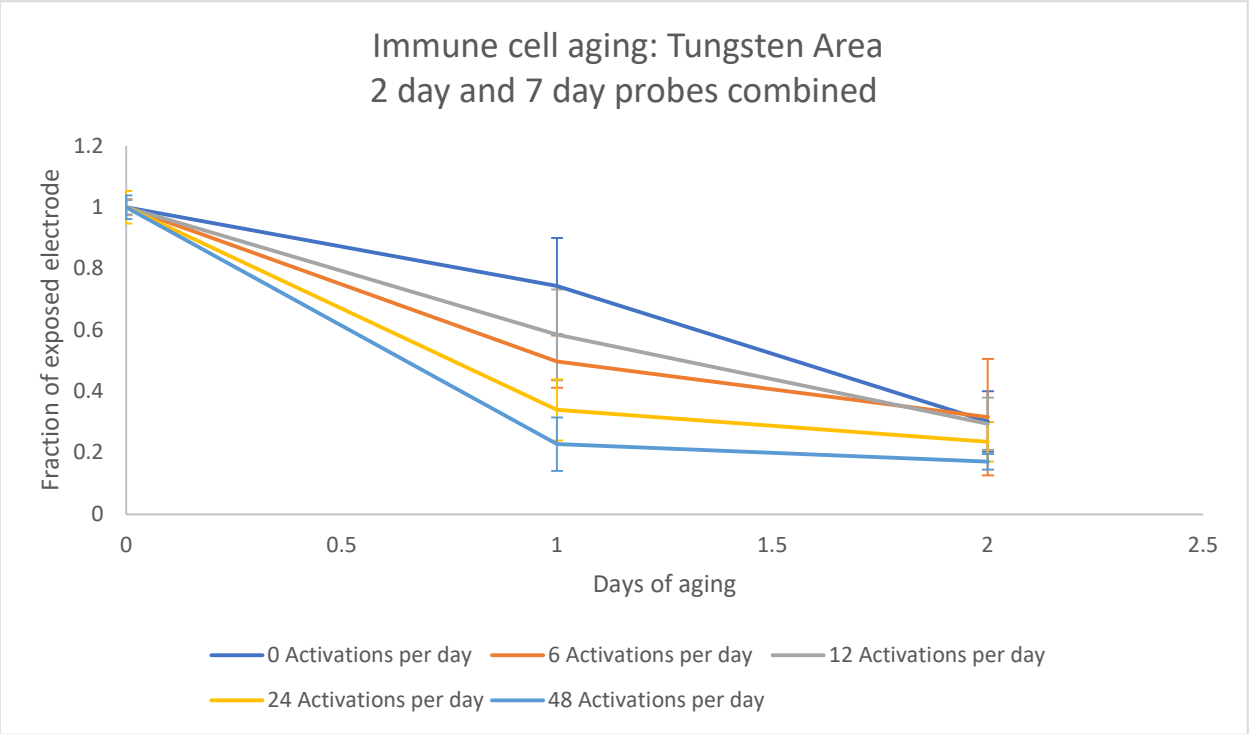

Figure 4.6 Normalized double layer capacitance trend over time for W microprobes aged for 2 days combined with the first 2 days of aging for 7 day aged W microprobes

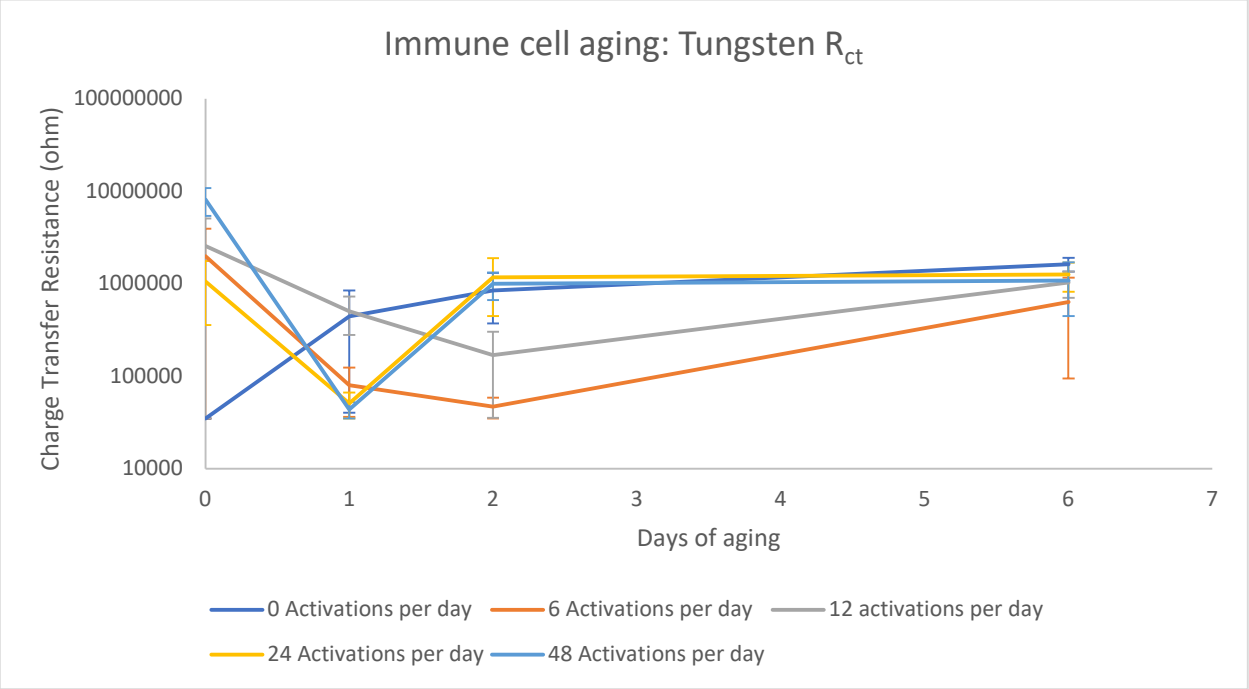

Figure 4.7 Charge transfer resistance trend over time for W microprobes

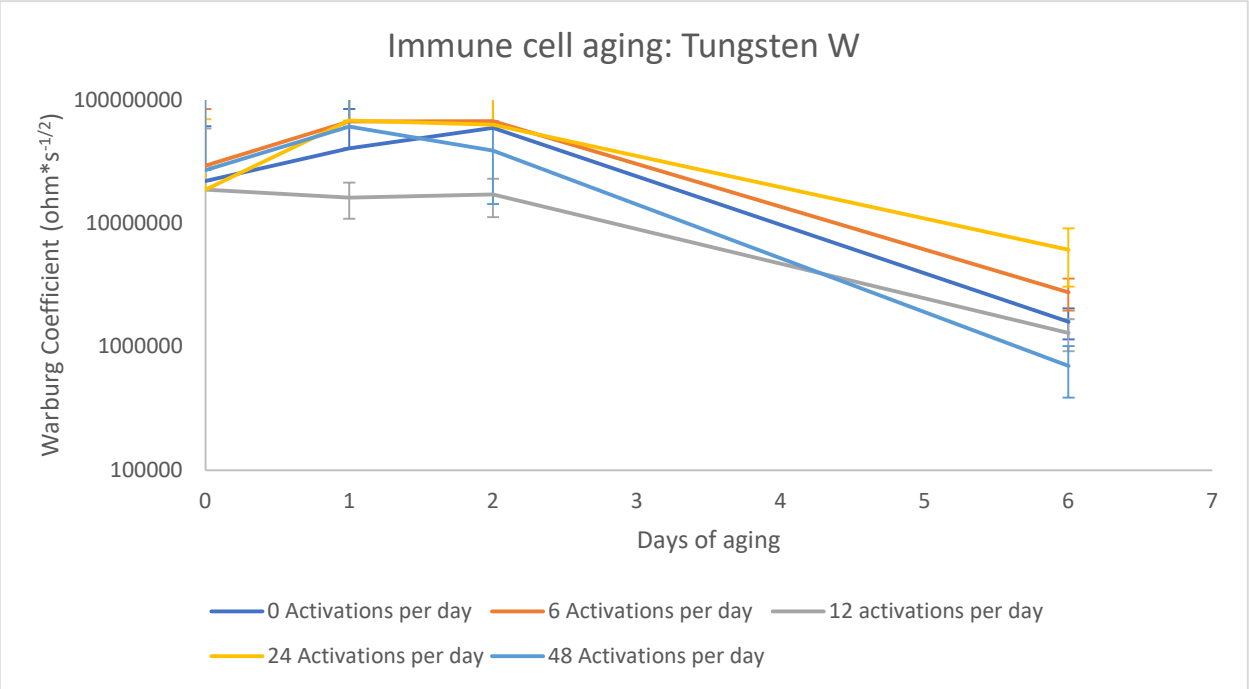

Figure 4.8 Warburg coefficient trend over time for W microprobes

The EIS results for immune cell accelerated aging of Pt/Ir probes over 2 weeks is shown in figures 4.9-4.11. This data suggests no significant trend in the double layer capacitance, consistent with the prediction in eq. 3.7 that the dominant contributor to a change in double layer capacitance is a change in exposed electrode area. Interestingly, there is a clear upward trend in the charge transfer resistance after the first day of aging. This result could indicate an increase in electrode area if all other contributors to charge transfer resistance were held constant. However, no increase in electrode area was observed by SEM. Without further testing, it is difficult to determine the mechanism behind this change in charge transfer resistance, but one explanation could be the removal of an easily dissolvable layer on the electrode surface. Day 0 measurements were taken immediately after the implant was submerged in cell culture media and any oxidation layer that may have formed during implant handling could have been in the process of dissolving during day 0 measurements, leading to a lower Rct. An easily removable oxide layer would lead to a lower Rct than expected because the i_0, ion exchange current density, a measure of the ease of dissolution, would be decreased. However, once this layer was removed, the electrode would stabilize at the i_0 value of the underlying Pt/Ir, as observed in figure 4.10. Further experiments were not performed to validate this hypothesis. The Warburg coefficient does not follow any monotonic trends in figure 4.11. The results of the Pt/Ir EIS measurements suggest that EIS is not highly indicative of electrode integrity for Pt/Ir probes coated in Parylene C, as has been reported in literature[4].

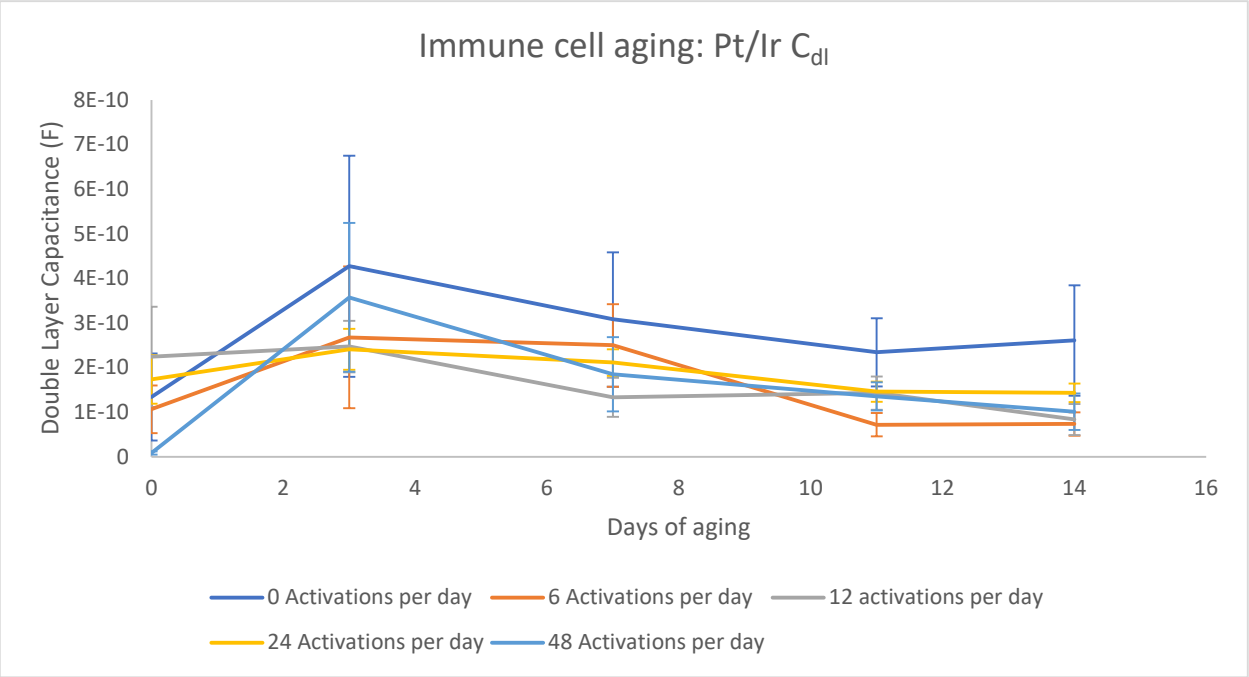

Figure 4.9 Double layer capacitance trend over time for Pt/Ir microprobes

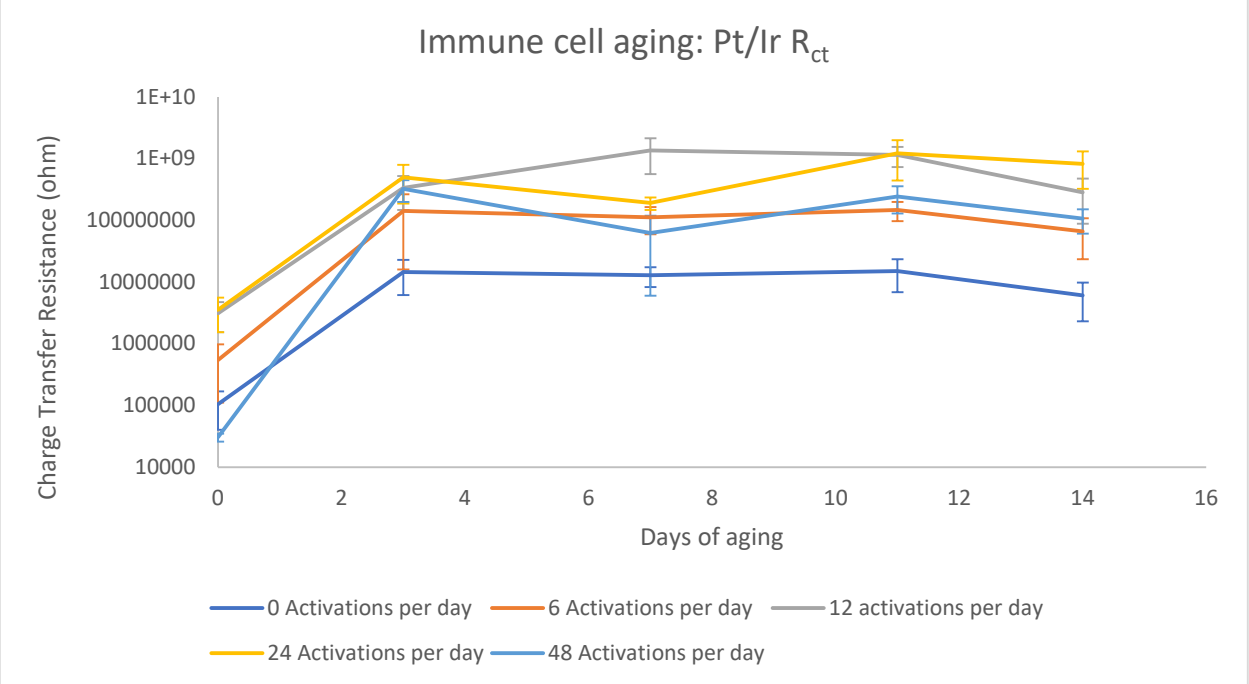

Figure 4.10 Charge transfer resistance trend over time for Pt/Ir microprobes

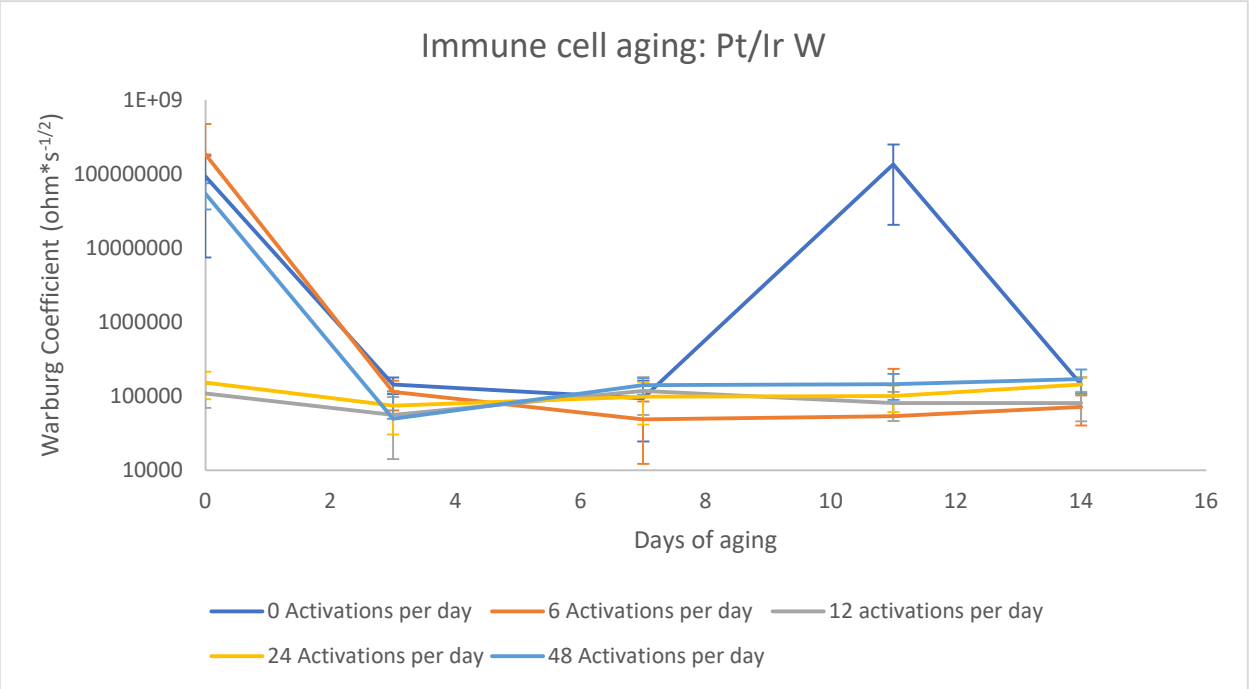

Figure 4.11 Warburg coefficient trend over time for Pt/Ir microprobes

4.3.3 Energy dispersive X-ray spectroscopy

In chapter 3, EDS was used to evaluate the reactive oxygen induced-polymer chain scission in Parylene C films. This section uses the same technique. Figure 4.12 and 4.13 show oxygen uptake in the Parylene C film increasing as a function of activation frequency. The increased oxygen uptake suggests an increase in reactive oxygen-induced polymer chain scission. Figure 4.12 shows the O:C ratio for each experimental condition evaluated with standard error from 4 replicates at each condition. Parylene C films on both W and Pt/Ir probes showed similar O:C ratios, indicating that electrode material did not influence O:C ratio. Figure 4.13 shows the amount of oxygen in the film as a function of the total number of activation events that the chamber was subjected to. Attention should be paid to the shape of this curve. A straight line would indicate that doubling the amount of reactive oxygen generated doubles the oxygen uptake in the film. It is not surprising that a straight line is not observed, as the number of available bonds to attack decreases as the amount of polymer chain scission increases. Figure 4.12 also gives critical insight about the degradation experienced by the polymer film. If the only factor affecting the oxygen uptake in the film was the total amount of reactive oxygen generated, doubling the rate of activation and halving the aging time should yield identical O:C ratios. Clearly, total reactive oxygen is not the only factor. Statistical analysis of this data yields a p-value of <.05 for both the total reactive oxygen and the aging time. Furthermore, the nonzero, increasing with aging time O:C ratio of the 0 activation samples suggests that there is some degree of reactive oxygen generation occurring without any activating species present, providing insight into why aging time is a statistically significant factor separate from total activations. Since this same reactive oxygen is generated in the body in response to the implantation of probes, the passive generation of reactive species observed in the

microfluidic bioreactor was expected and necessitated the inclusion of the zero activations condition.

Hydrogen peroxide aging has not been shown to increase reactive oxygen-induced polymer chain scission to the same degree as in vivo aging[3]. Thus far, hydrogen peroxide-assisted aging has been unable to accelerate this failure mechanism. In figures 4.12 and 4.13, reactive oxygen-induced polymer chain scission is observed beyond what is seen in vivo[3] (figure 3.11). Additionally, immune cell aging is able to achieve implant degradation acceleration without elevated temperatures. This feature is a benefit because it avoids any phase transition-related aging nonidealities and it is a drawback as immune cell aging is incompatible with elevated temperatures, making the Arrhenius-style acceleration method impossible.

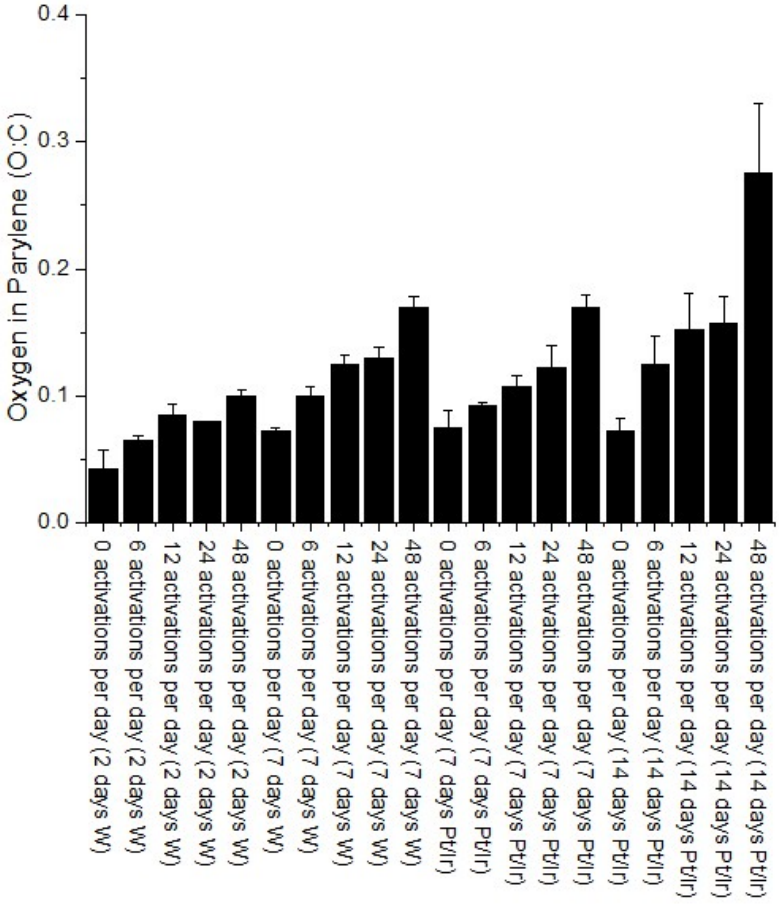

Figure 4.12 O:C ratio of Paryene C film as a function of aging condition

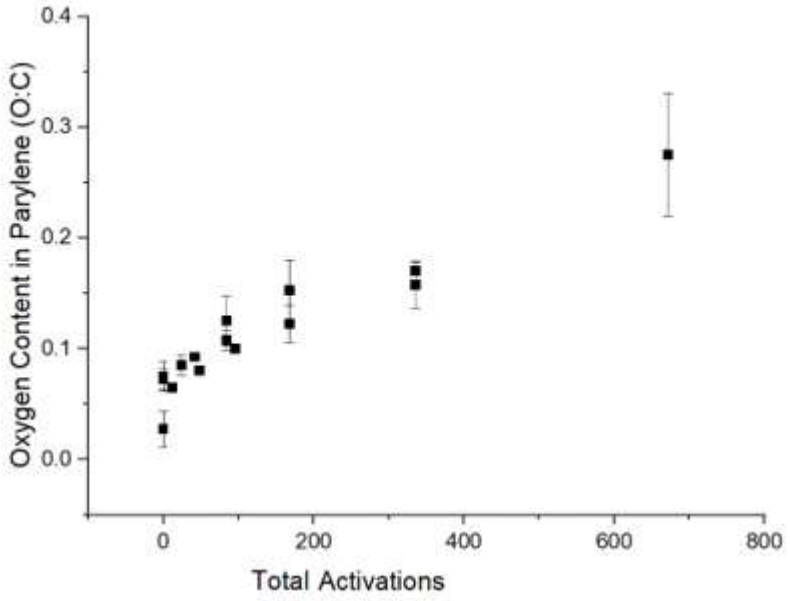

Figure 4.13 O:C ratio as a function of total J774a.1 cell activations a sample was subjected to. W and Pt/Ir samples have been combined.

The exact acceleration factor achieved by immune cell acceleration can be calculated several ways. The ideal solution would be to perfectly quantify the number of moles of each reactive species present at an implant site over time and determine the appropriate in vitro activation frequency that achieves the desired acceleration. This solution is currently unavailable as no such quantification of reactive species has been successfully attempted. Additionally, as implant designs change, the intensity of the immune response is likely to change as well.

An alternative method is to compare the damage observed on explanted in vivo implants to the damage observed on in vitro accelerated aged implants. With only one time point, 3.25 years[3], measured using the O:C ratio EDS technique, this method does not provide a pathway towards a quantitative acceleration factor.

A third method, and the one chosen, is a comparison between the rate of oxygen uptake for the 0 activations samples and the activated samples. A power law relationship between O:C ratio and days of aging in the 0 activation chamber was determined to be the best fit (figure 4.14 and eq. 1). The O:C ratios of the activated chamber samples were converted to “days of aging in the 0 activation chamber” using this power law relationship. The converted “days of aging in the 0 activation chamber” were divided by the actual number of days aged at the activation condition of the sample to determine an acceleration factor (eq. 2). This acceleration factor is shown in Table 4.1. The acceleration follows a trend of “doubling the activation frequency doubles the acceleration factor” for all conditions except 24 activations per day. This table indicates that activating 6 times per day gives an acceleration of ~4.5x, going up to ~36x (39.7x) at an activation frequency of 48 activations per day.

This acceleration factor is relative to a cell culture of mouse immune cells, not a human brain, but does show the potential of the immune cell aging technique to accelerate degradation of neural implants using cell-generated reactive oxygen species. Acceleration of implant aging provides a pathway towards a prediction of implant lifetime. Using the "2x per 10°C" acceleration model for thermal aging described in chapter 3, the maximum acceleration that a thermal method could achieve without facing significant water boiling issues is achieved at 87°C. This is 50°C warmer than the human body and should provide a 32x acceleration. This places the acceleration factor of 39.7x for reactive oxygen-induced polymer chain scission achieved by immune cell acceleration very close to the acceleration achieved by thermal aging. At this acceleration, an implant would have to resist degradation for 46 days in a microfluidic chamber undergoing 48 J774a.1 activations per day to reach a prediction of 5 years lifetime in vivo. This is valuable as an early step in the implant evaluation process, as any implant that fails the accelerated aging test should not be considered for in vivo evaluation until durability improvements have been made.

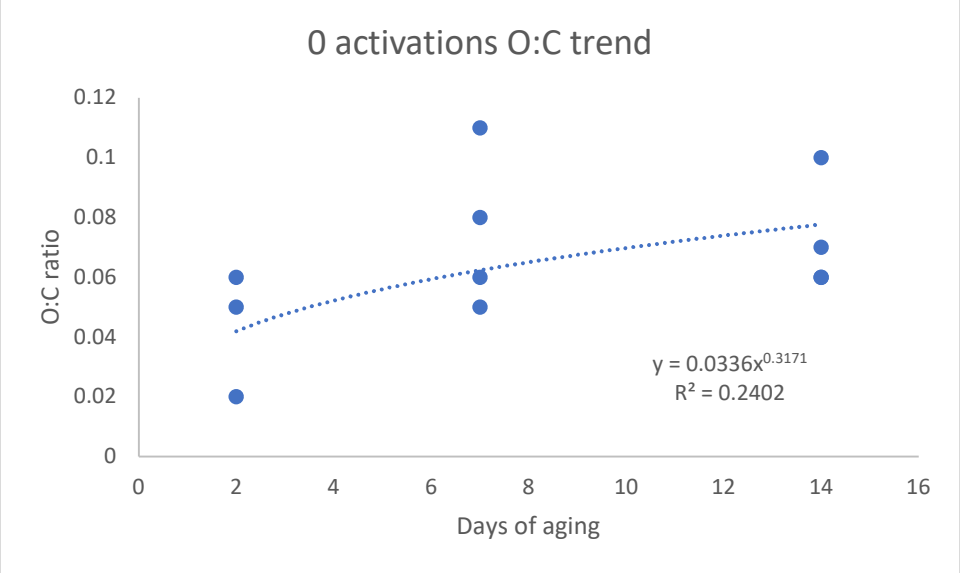

Figure 4.14 Power law relationship describing the O:C trend over time for the 0 activations condition

$$O{:}\,C\ ratio_{0\ activations} = 0.0336 * time\ in\ days_{0\ activations}^{0.3171} \quad (1)$$

$$acceleration\ factor_{x\ activations} = \frac{\sqrt[0.3171]{\frac{O{:}C\ ratio_{x\ activations}}{0.0336}}}{time\ in\ days_{0\ activations}} \quad (2)$$

Table 4.1 Acceleration factor of J774a.1 cell aging

Activations per day	Average acceleration factor	Standard error
6	4.53	0.94
12	9.06	1.62
24	9.59	1.812
48	39.68	16.84

4.3.4 Heated saline/hydrogen peroxide aging compared to immune cell aging

While the previous chapter showed the benefits of using a microfluidic chamber for accelerated aging using previously described aging methods, this chapter introduced an entirely new aging technology. This new technology is able to produce degradation in neural probes similar to what has been observed in vivo. The relative rates of degradation between accelerated aging mechanisms were not the same. Comparing figure 3.7 to figures 4.5 and 4.6, the heated saline/hydrogen peroxide aging method caused complete dissolution of the exposed tungsten probe tips after 1 day, while the tungsten probes aged using the immune aging method took up to 6 days to fully recede into the insulation. Clearly, the heated saline method was more aggressive than the immune aging method. Figure 3.3 indicates that tungsten fully recedes in vivo very rapidly so neither method showed a significant advantage in accurately predicting failure.

However, when comparing figure 3.10 to figure 4.12, the immune aging method caused greater reactive oxygen-induced polymer chain scission. Figure 3.11 showed that heated saline/hydrogen peroxide methods have not achieved the same degree of reactive oxygen-induced polymer chain scission as is observed in implants after 3.25 years in vivo. The reactive oxygen-induced polymer chain scission observed in immune cell aged probes exceeds what has been observed in vivo for the most aggressive aging conditions. The immune chamber may be too aggressive when predicting this failure for some aging conditions, but the heated saline/hydrogen peroxide method is not aggressive enough. Aging devices using both accelerated aging methods has the potential to be extremely valuable. For instance, an implant that can resist the reactive oxygen-induced polymer chain scission attack from the immune cell method and can resist the dissolution attack from the heated saline/hydrogen peroxide chamber should be resilient enough to resist the neural environment in vivo. An expansion of the experiments described in chapters 3 and 4 to a greater range of implant materials and designs is likely to further highlight the value in using multiple acceleration methods to evaluate implant durability.

4.4 Conclusion

This chapter demonstrated the use of a microfluidic bioreactor for immune cell assisted accelerated aging of neural implants. This technique aims to accelerate the degradation of neural implants that arises from the foreign body response attack on implanted devices. Using SEM and EIS, dissolution of tungsten microprobes was observed. The rate of dissolution, as determined by in

situ EIS, was dependent on the intensity of the reactive oxygen attack on the neural implant. This finding suggests that increased J774a.1 cell activation accelerates the dissolution of tungsten microprobes at physiological temperature. Additionally, EDS measurements showed that the degree of oxygen uptake in Parylene C films was statistically significantly dependent on total number of J774a.1 cell activation events and time of aging. This result suggests that reactive oxygen-induced polymer chain scission was accelerated by increased immune cell attack. Finally, using the rate of reactive oxygen-induced polymer chain scission experienced by Parylene C films in microfluidic chambers with immune cells that were not introduced to PMA, an O:C ratio vs time power law relationship was proposed. This relationship was used to determine the acceleration factor achieved by different immune cell activation frequencies. The acceleration achieved for reactive oxygen-induced polymer chain scission in immune cell aging chambers was comparable to what is possible using thermal acceleration methods, 39.7x and 32x respectively.

4.5 References

1. Zheng, X. Sally, Noah R. Snyder, Kevin Woeppel, Jenna H. Barengo, Xia Li, James Eles, Christi L. Kolarcik, and X. Tracy Cui. “A Superoxide Scavenging Coating for Improving Tissue Response to Neural Implants.” Acta Biomaterialia 99 (November 1, 2019): 72–83. https://doi.org/10.1016/j.actbio.2019.08.032.

2. Prasad, Abhishek, Qing-Shan Xue, Viswanath Sankar, Toshikazu Nishida, Gerry Shaw, Wolfgang J. Streit, and Justin C. Sanchez. “Comprehensive Characterization and Failure Modes of Tungsten Microwire Arrays in Chronic Neural Implants.” Journal of Neural Engineering 9, no. 5 (September 2012): 056015. https://doi.org/10.1088/1741-2560/9/5/056015.

3. Caldwell, Ryan, Matthew G. Street, Rohit Sharma, Pavel Takmakov, Brian Baker, and Loren Rieth. “Characterization of Parylene-C Degradation Mechanisms: In Vitro Reactive Accelerated Aging Model Compared to Multiyear in Vivo Implantation.” Biomaterials 232 (February 1, 2020): 119731. https://doi.org/10.1016/j.biomaterials.2019.119731.

4. Prasad, Abhishek, Qing-Shan Xue, Robert Dieme, Viswanath Sankar, Roxanne Mayrand, Toshikazu Nishida, Wolfgang Streit, and Justin Sanchez. “Abiotic-Biotic Characterization of Pt/Ir Microelectrode Arrays in Chronic Implants.” Frontiers in Neuroengineering 7 (2014). https://www.frontiersin.org/articles/10.3389/fneng.2014.00002.

Chapter 5. Modelling for Chronic-Minded Design of Neural Implants

5.1 Introduction and Motivation

5.1.1 Outline

The goal of this chapter is to model implant lifetime using available data from literature. This chapter will outline the primary mechanisms of failure of intracortical devices and then propose a model of a neuron in solution generating a signal to be detected by an equivalent circuit model of a neural implant. The neural signal will provide an avenue toward lifetime estimation through the use of the signal-to-noise ratio. SNR will be used as the metric for device viability because the ability distinguish individual neurons from each other is one of the main benefits of intracortical recording when compared to other neural recording techniques and this ability is lost when the signal of an individual neuron cannot be distinguished from the noise of the neural environment. Finally, the results of the model will be used to provide guidelines for intracortical implant designers.

5.1.2 Intracortical Implant Background

Intracortical recording electrodes implanted in the surface of the brain to record single neuron action potentials have been proposed to treat a variety of neurological and physical disorders. Patients with full paralysis have shown operation of robotic limbs[1]. There is a push from DARPA to look at implants as a method to treat psychiatric disorders like depression and post-traumatic stress disorder[2]. These projects rely on the potential for chronic neural recording on the single neuron scale.

For a brain surgery to be the best option, these implants must operate in the brain for upwards of five to ten years. Unfortunately, current devices fail on the order of weeks or months, with very few devices operating for five years or more. Devices fail for a variety of reasons. In order to understand these, we must first understand what constitutes an operating device. The device must be able to detect a single action potential. It must be able to separate that action potential from background noise, and it must be able to relay this information to a location of interest, typically outside of the skull.

A typical device consists of an array of conductive electrode shanks that are insulated from the body by an electrically insulating coating and exposed at their tip for recording. A perfect device would not disturb its surrounding area and would be immune to any kind of chemical or physical attack, we will call these requirements “biological” and “material” considerations respectively. The

biological response is often quite complex, shown in figure 5.1. First, the puncture of the meninges can cause bleeding and clotting, leading to damage to the host. This puncture can allow foreign agents into the brain and cause infection, also damaging the host. If the host survives, the neural recordings can be inhibited by glial scarring and fibrous tissue. Glia are cells that support the brain by protecting neurons. These glial cells respond to attack, such as an implantation event, by rushing to the affected area in a process called gliosis. As a part of this response, astrocytes, a subtype of glial cell that is large and star shaped, are recruited to the area. These astrocytes aim to surround the implant and insulate the surrounding neurons from its presence by forming a glial scar. If the glial cells fail to protect the neurons from the implant, the neurons can suffer from neuronal death and no longer fire. All of these failures lead to a device which functions properly in its goal to have the capability to record action potentials but is incapable of distinguishing the nearest neuron from background noise.

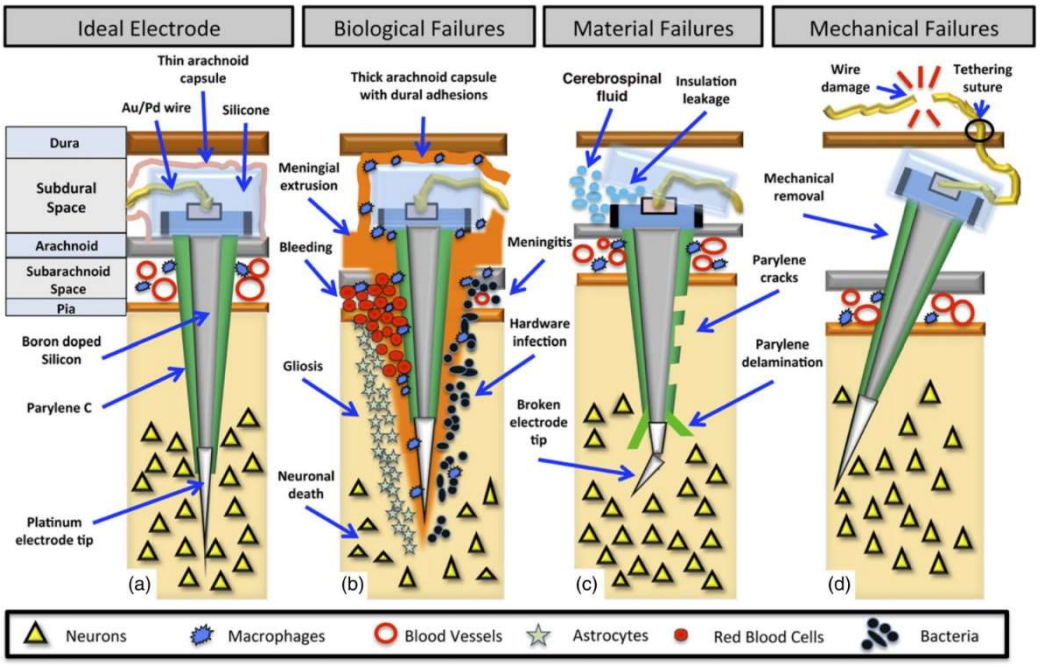

Figure 5.1: Possible failure mechanisms for an ideal shank of a Utah Electrode Array[3]

In order to build a model of the biological response, we employ the general biomaterial response scheme, shown in figure 5.2. No matter where in the body a device is implanted, the first thing that happens to it is that proteins adsorb to its surface. These proteins present themselves such that cells attach. Once these cells attach, they will begin to release signaling compounds that recruit foreign body defense cells. These defense cells will eventually form an encapsulation that protects the body from the perceived threat of the device. This encapsulation is formed by gliosis, astrocytes, fibrous tissue, and a finite thickness of dead neurons in the brain's response. This

encapsulation layer serves to prevent the recording of healthy neurons, limiting the lifetime of implants by how long they will be near enough a single neuron to properly record its activity.

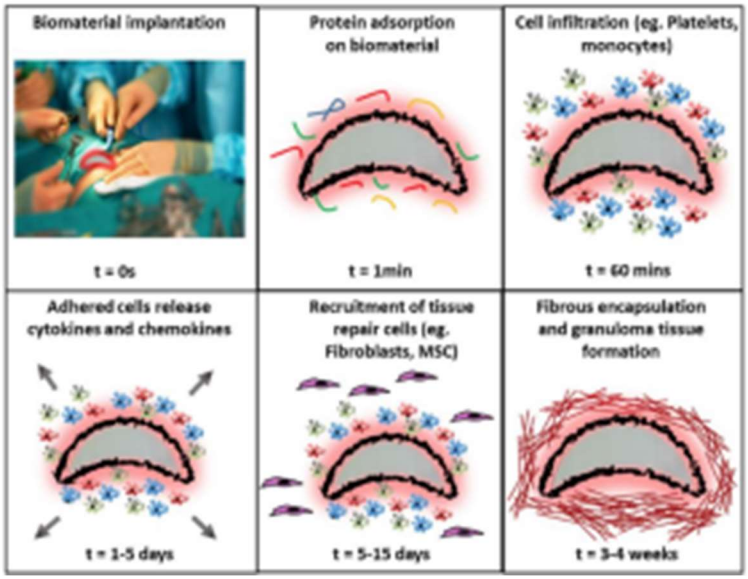

Figure 5.2: All implants follow a similar biological response upon implantation. Proteins attach, they promote cell adhesion, the cells signal for the foreign body response, the foreign body response arrives and encapsulates the implant[4].

If the brain does not reject the device, the device can also fail due to the response of the implant to the brain environment. The environment that an implant sees in the brain is cerebrospinal fluid, a saline solution that contains the necessary proteins to promote cell growth in the brain. It is no secret that many materials, particularly metals, experience corrosion and dissolution in saltwater environments. Devices can fail due to interconnect corrosion or electrode corrosion. Additionally, the brain experiences a finite amount of motion in everyday life called micromotion. There are a few millimeters of space between the brain and the skull that the brain can move around in. This motion can cause mechanical failure of a brittle device in the event of a head trauma or concussion. If the tip of the device breaks, the device can no longer serve its function of recording neural activity. The insulation surrounding the electrode shank can fail via delamination if it is not properly bonded to the electrode. It can also crack in the saline environment in a process known as stress corrosion cracking. Additionally, processing of the insulating layer can create pinholes in the coating. All of these insulation failures allow electrical noise to poison the device recording and saline to attack the unprotected electrode shank leading to shorting and electrode crosstalk. Both material and biological failure have to be prevented in order for chronic recording to be achievable.

The goal of this chapter and indeed, of much of this overall work is to build a model framework that incorporates prediction of both material and biological failure in order to inform chronic-minded implant design.

5.2 Review of Implant Design

5.2.1 Animal Models

Animal models have historically been used to test a hypothesis about how the brain works. Much of this work has focused on short term (<1 year) experiments. This has led to a neglect of the long-term performance of recording implants. In an effort to understand the long-term performance of the Utah Electrode Array (UEA), Baresse et al. performed a review of 78 arrays implanted in 27 monkeys over 16 years[3] (figures 5.3 and 5.4). This review focused on the failure of the implants and employed a failure criterion that every electrode on an array must be unable to distinguish neural activity for that array to have failed. Of the 78, 16 implants were in animals that were sacrificed at a specified time point for study. Of the remaining 62, 70% of the devices failed before one year and none lasted beyond year six. A large portion of these failures was due to mechanical failure associated with the tethering portion of the implant, a problem we hope to avoid by using wireless implants. Of the other failures, they were split between material and biological. The review is the most comprehensive consideration of chronic recording in live subjects to date.

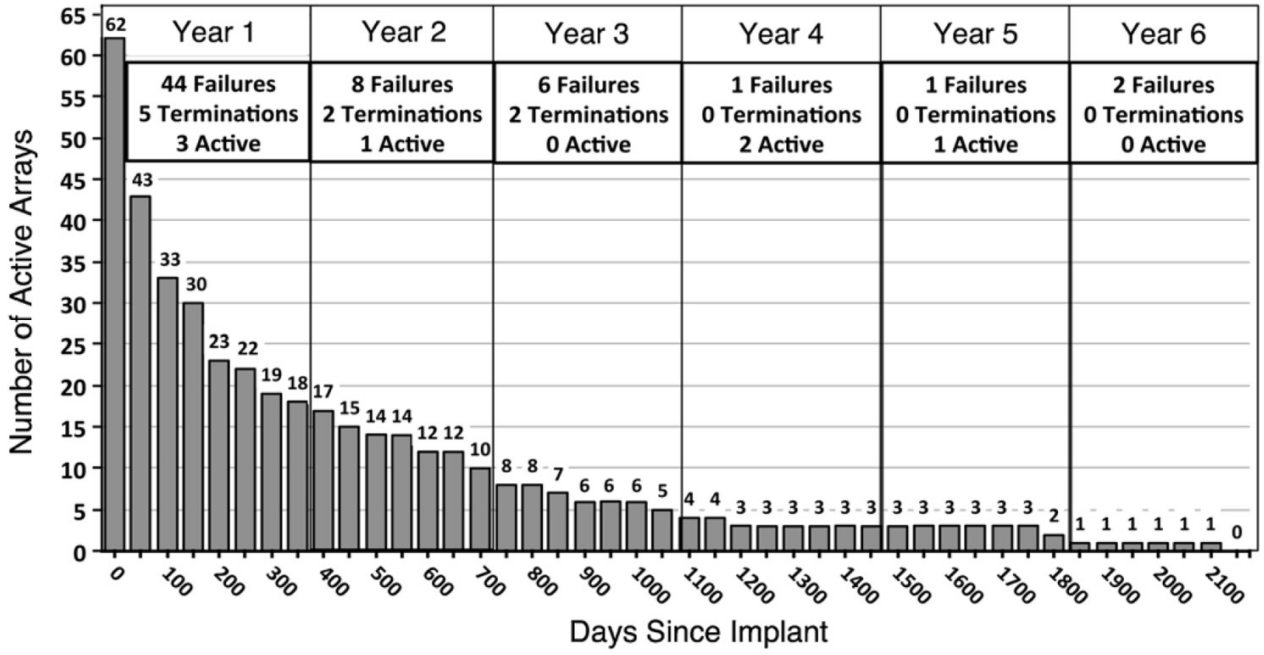

Figure 5.3: Number of active arrays implanted in non-human primates as a function of time. An array is active if any of its electrodes is recording a single neuron[3].

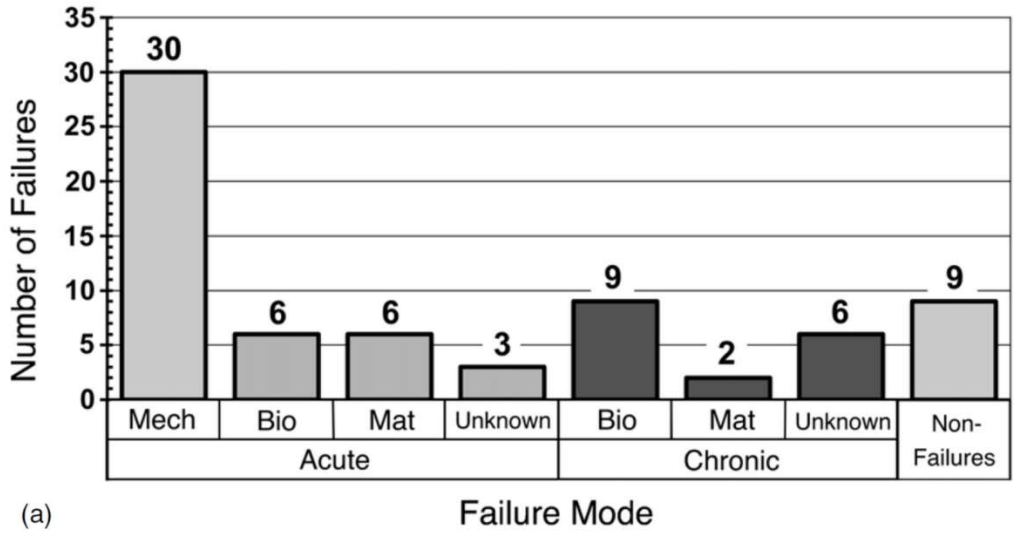

Figure 5.4: Arrays sorted by failure mode. Failure modes correspond to the failures presented in figure 5.1. Failure is split evenly between biological and material failure with mechanical failure dominating due to the implants being tethered[3].

5.2.2 In Vitro Models

Many have attempted to predict device failure by testing in an analogous in vitro environment. Most of these attempts use an increase in temperature of 10^{o}C to represent a doubling of the aging rate in an estimate of Arrhenius behavior. Often these models don't consider whether a material undergoes a phase transition in the operation range of the experiment. A recent FDA study uses temperature to accelerate aging and hydrogen peroxide to simulate the biological response of the body[5] (figure 5.5). A typical macrophage response to an implant consists of a frustration stage where the macrophages release reactive oxygen species to attack the foreign body. The reactive oxygen quickly decays into hydrogen peroxide in a process facilitated by the enzyme superoxide dismutase. It is this hydrogen peroxide response that the study hopes to imitate. This type of modelling can give an idea of implant lifetime but fails to capture the biological response and any synergistic effects that could degrade the recording capability of the implant. One example of the shortcomings of this style of device analysis is that it can predict lifetimes of >70 years when in vivo testing shows lifetimes of <1 year[6,7].

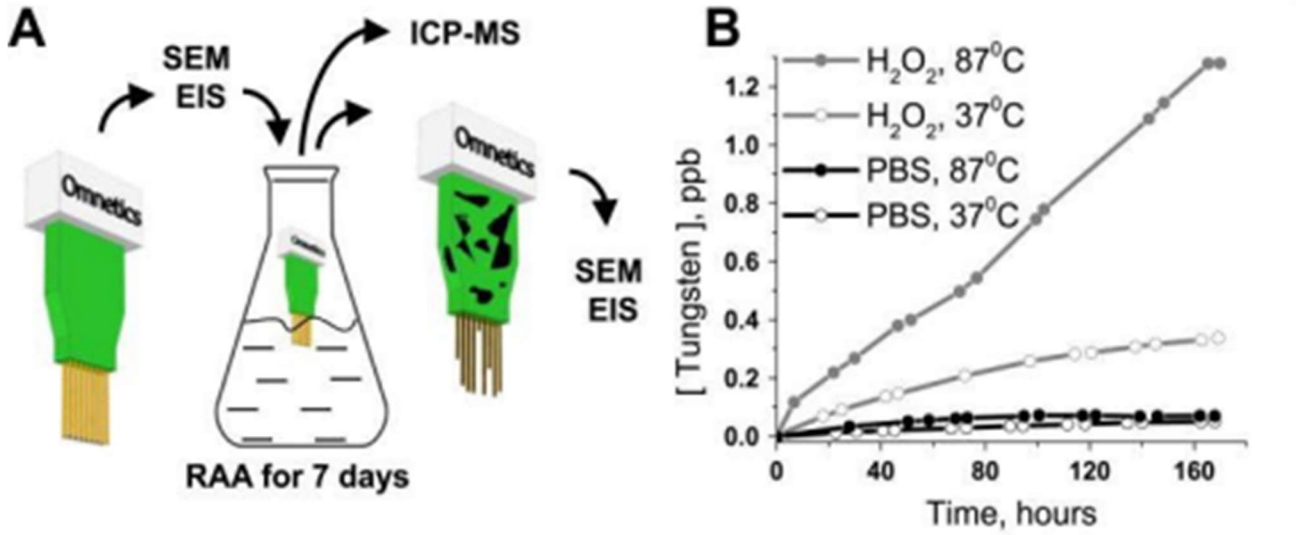

Figure 5.5: Devices were submerged in phosphate buffered saline (PBS) and exposed to hydrogen peroxide. The dissolution of the wires was measured using inductively coupled mass spectrometry. The combination of hydrogen peroxide and temperature was most damaging[5].

5.2.3 State of the Art Implants

For the first few decades, all neural implant work was done with metal electrodes, first with single shank implants, and then later moving towards metal microwire arrays to accommodate multichannel recording. From these studies conducted with the metal microwire systems, the research community began to understand the failure mechanisms at play in neural implants, which built the foundation for the most widely used designs in use today.

The rise of the neural implant field has seen the commercialization of several designs, which are commonly used because they are available off the shelf and allow research groups to skip the detailed, labor-intensive fabrication processes that were once mandatory to do neural implant research. The Utah array, now owned by Blackrock Microsystems, remains one of the most widely used design today because of its approval from the FDA for human trials. Consisting of 96-128 Pt-coated silicon electrodes, these electrodes are coated in Parylene C, and are roughly 1mm in length. The TDT design (from Tucker-Davis Technologies), utilizes 50um tungsten microwires coated in polyimide. Available designs from NeuroNexus implement a multi-site recording configuration, which positions multiple iridium recording sites along a single silicon probe, increasing the number of channels that can be recorded from at a time.

These devices in commercial production are very similar: a hard probe material roughly 20-80um in diameter, a soft encapsulation material that is designed to conform to the probe surface, and a small exposure region at the probe tip that is coated in a low-resistivity metal. The research

community works with these materials (electrode: tungsten, silicon, insulation: polyimide, SiO_2, Parylene C, tip coating: platinum, iridium) because they are commonly used in microelectronics fabrication, and we have considerable knowledge and tooling to support building neural implants. However, studies in recent years have uncovered several important failure mechanisms, namely the effect of high Young's modulus on glial scarring[8], modulus mismatch between electrode and insulation as a cause of delamination[9], and the difficulties of using Parylene C in biologically imitating testbeds[5].

These works highlight the need to explore materials which may have drastically different properties, and a few examples are presented here. Carbon fibers are one new material being explored, having diameters <5um and a stiffness orders of magnitude lower than hard silicon/metal electrodes[10]. While the conductivity is lower and insertion remains an open problem, the less intrusive fibers are less likely to provoke a strong glial response. Taking the goal of smaller and more flexible even farther, Luan et. al fabricated 10x10x1um electrodes out of thin gold/platinum electrodes and SU-8 photoresist and demonstrated negligible glial scarring with their devices[11]. Diaz-Botia et. al have fabricated an all-silicon carbide device, the benefits of which include modulus-matched electrode and insulation for reduced delamination, high chemical resistance from the SiC outer layer, and ease of fabrication by use of the same material for both electrode and insulation[12].

The takeaways from state-of-the-art research are that softer, smaller, and wireless devices are seen as device traits to strive for. We ignored the wireless/wired design constraint in this model, as it is well known that wired devices leave a patient vulnerable to breakage and infection. Implantable wireless devices have been demonstrated, and we expect that wireless transmission will be possible for future neural implants[13]. We see this modelling effort not as identifying the high-level attributes which should guide device design, but as a detailed quantitative analysis of the various tradeoffs which are inevitable in complex designs. By understanding and quantifying these tradeoffs with respect to device lifetime, the field of neural implants will be able to more rapidly screen out infeasible designs and focus their resources on testing designs that meet the broad set of attributes required for long lifetimes.

5.3 Screening

Before a device is considered for in vivo or accelerated lifetime testing, it must be screened for obvious incompatibility. This step of this model works to define the viable design space for chronic neural implants, enabling the assumption that any device that would be evaluated using this model has already passed the screening phase.

5.3.1 Cytotoxicity

Cytotoxicity tests are common to assess the biocompatibility of a compound or material. In a cytotoxicity test, the device of choice is placed in a tissue culture dish of relevant cells. After a set time, the device is removed, and the dish is counted to determine the number of dead or unhealthy cells. If this number is statistically significantly different than a control dish, the device is determined to be cytotoxic and unacceptable for implantation[14].

5.3.2 Galvanic Corrosion

Galvanic corrosion occurs when two dissimilar metals contact and are allowed to exchange ions and electrons. This might occur in an implant at wiring contacts or even at the electrode tip as in the UEA. The rate of reaction depends on the environment the metals are placed in and their separation on the anodic index. For saltwater environments, like the human brain, a separation of less than 0.15 V is recommended[15].

5.3.3 Swelling and Delamination

In order to assess the impact of swelling and delamination on the viability of an implant design, we use a simple relationship between the strength of the bond between the implant and insulation and the stress applied on the interface due to swelling. Figure 5.6 shows an example of Parylene C delamination.

$$\varepsilon_{swelling} * E_{insulation} < Adhesion\ Strength \quad (1)$$

Where $\varepsilon_{swelling}$ is the strain due to swelling and $E_{insulation}$ is the modulus of elasticity of the insulation.

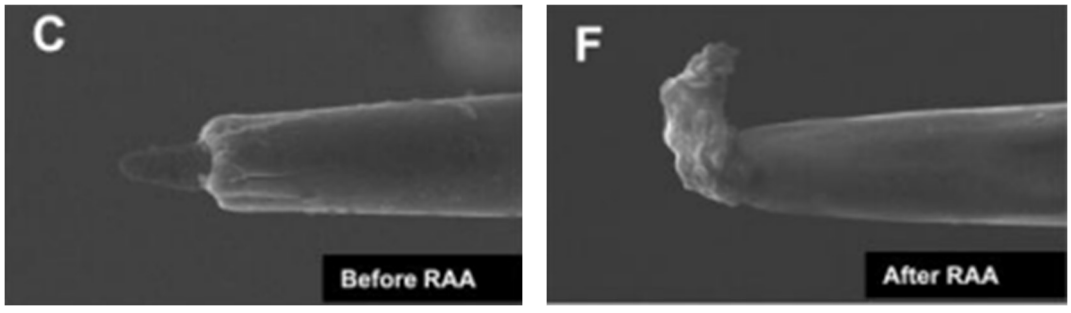

Figure 5.6: Delamination of Parylene C from tungsten microwires was observed after reactive accelerated aging. This delamination was likely influenced by the temperature of aging, 87C, approaching the glass transition temperature of Parylene C[5].

5.4 Modelling Basis

5.4.1 Physical Model

In order to quantify the effect of various electrode and insulation properties on recorded signal, we first recreated a physical model from literature[16] that describes signal amplitude as a function of distance from a given neuron. This physical model assumes a perfect electrode and provides the foundation for the circuit model that is described in the next section.

When a neuron fires, electrons conduct through its axons. These electrons are described as a current, and we are able to detect this current by detecting the resulting electric field, which is measured as a voltage.

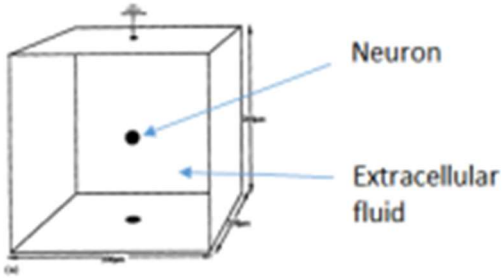

Figure 5.7: Physical setup for distance-amplitude model[16]

We describe the problem as shown in figure 5.7, with a singular neuron surrounded by a resistive fluid, and the far edge of the setup at ground potential. A recording electrode exists at a given distance away from the neuron.

$$J = \sigma E = -\sigma \frac{d\phi}{dr} \tag{2}$$

Eq. 2 relates how the conductivity of the fluid surrounding the neuron, which we label "extracellular fluid", relates the current density of the neuron to the electric field produced by this current flow. As we know electric field can be calculated as a function of distance and voltage, we show this relation as well.

$$\phi = -\int_a^b \frac{J}{\sigma} dr = -\int_a^b \frac{I}{4\pi r^2 \sigma} = \frac{I}{4\pi\sigma r} \tag{3}$$

We are interested in measuring a voltage for this setup, so we rearrange eq. 2 and integrate to solve for phi. The final result demonstrates a simple relation between current (neuronal current density * neuronal surface area), extracellular fluid conductivity, and distance from the center of the neuron to the recording electrode. For this model, a neuron with a radius of 5um was used[16], and neuronal surface area was calculated from this value. Values for neuronal current density (10E-12 A/um^2) and extracellular fluid conductivity (3.3E-7 S/m) were extracted from the same literature[16].

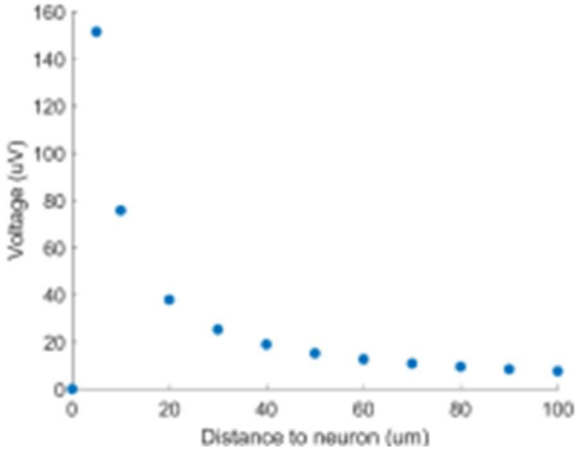

Figure 5.8: V_{sig} vs distance from measured neuron

To confirm the values produced by this model, we plot the distance to the neuron against the peak voltage amplitude in Figure 5.8. The decay is described by a 1/r relationship with distance and a peak amplitude of 150uV, with around 40-80 µV signal at a distance of 10-20um, within the 10-100 µV typically seen in intracortical recording[22].

This peak voltage represents the maximum voltage that the recording electrodes can measure at a given distance, as we have assumed an ideal electrode with perfect insulation. The following section now investigates non-idealities, using the physical model described above as the foundation.

5.4.2 Equivalent Circuit Model

To quantify the lifetime of a device, it was clear that we had to characterize the decay in signal quality over time and find the time point at which the signal was no longer usable. In literature review, it became apparent that impedance is a common metric for signal quality, and frequently impedance, specifically at 1 kHz, is tied to changes in device performance, and then device lifetime[3,5] (figure 5.9).

It has been noted that many material and device factors affect impedance, some of which can increase impedance (electrode cracking, corrosion) and some of which decrease impedance (delamination, shorting). These effects confound the use of impedance as a lifetime metric and motivate the use of alternative metrics.

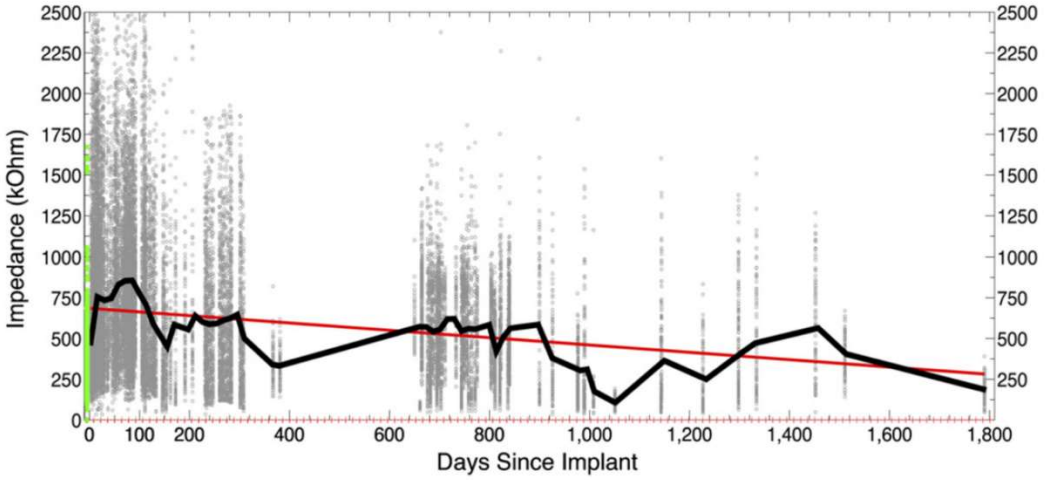

Figure 5.9: Weak correlation between electrode area and ratio of 1kHz impedance pre- and post-aging[5].

Fundamentally, a signal becomes useless to an observer when the signal can no longer be distinguished from the noise. (While impedance plays a role in signal-to-noise ratio, it doesn't explain the full picture, and that is why impedance has been shown to be a poor indicator of device lifetime.) We decided to model the signal produced by a neuron, and the noise produced by the electrode and the surrounding environment, and then establish a cutoff value for signal-to-noise ratio of these two models. Once the device has a SNR below this threshold, it is considered useless, and its lifetime is finished.

5.4.2.1 Signal Model

In section 5.4.1, we established the maximum voltage that can be recorded, assuming a perfect electrode. The situation in a real device is more complicated, and equivalent circuit models for recording electrodes have been described in the literature to understand these non-idealities.

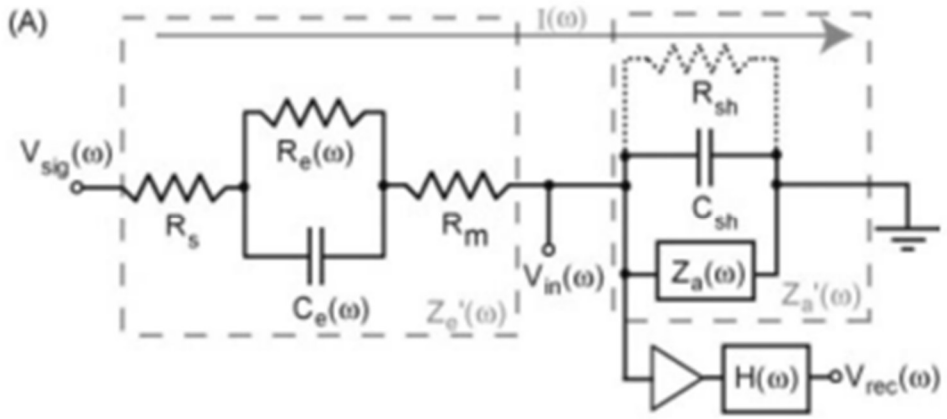

Figure 5.10: Equivalent circuit model for a recording electrode[17]

At a high level, we are interested in understanding how much of that maximum signal, labeled V_{sig} in figure 5.10, can be detected by the amplifier (impedance=Za), and measured as a signal, labeled V_{rec}. If we are able to start with the maximum signal, and calculate the loss, we can calculate the measured signal, making V_{sig} the "signal" in the signal-to-noise ratio.

The loss mechanism in the electrode can be understood as a voltage divider across two impedance elements, the electrode (Ze') and the amplifier (Za'), shown in grey boxes in Figure 5.10. The simplified picture is presented in Figure 5.11. This is quantitatively described in eq. 4, where the ratio of Za' to Za'+Ze' sets the percentage of V_{sig} that is reached V_{rec}. Ideally Za' >> Ze', and therefore no voltage is dropped across the electrode, and the signal maintains its maximum value until it is read by the amplifier circuit. If Za' decreases, or Ze' increases, some voltage gets dropped across the electrode, and this loss will decrease the measured signal, which is captured in the SNR value.

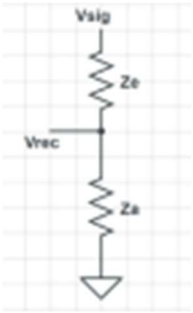

Figure 5.11: Simplified circuit model, highlighting the voltage divider present in the circuit model

$$V_{rec} = \frac{V_{sig} Z_a{}'}{Z_a{}' + Z_e{}'} \quad (4)$$

Describing each element of the equivalent circuit model:

Tip/solution resistance (Rs): the interface between electrode and biological solution in the brain has a resistance, dictated by the conductivity of the fluid and the geometry of the electrode tip. This is modeled in eq.5 as a thin semicircular shell of fluid with resistivity rho ((ρ=0.725E6 Ωμm[18]) around a semicircular electrode tip of diameter d.

$$R_s = \int_r^{\infty} dR_s = \frac{\rho_{solution}}{4\pi r} = \frac{\rho_{solution}}{2\pi d_{electrode\_tip}} \quad (5)$$

RC network at the input of electrode (Re, Ce): Figure 5.12 shows the geometry of an electrode tip. There is a resistance to the tip of the electrode, and a capacitance associated with the tip, and these are captured in the Re and Ce terms.

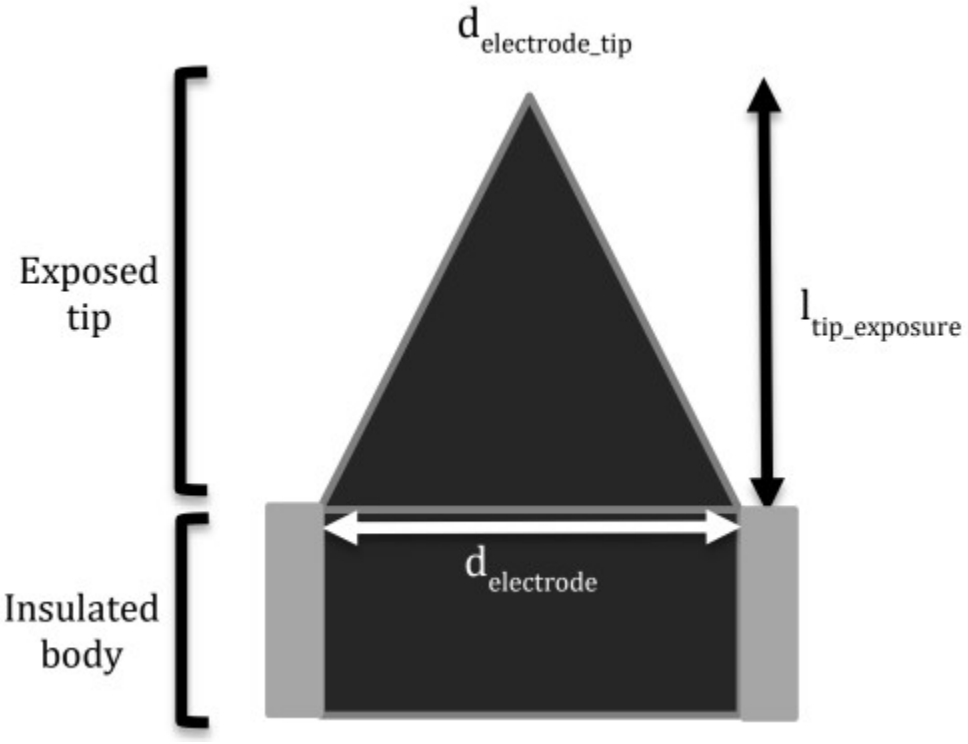

Figure 5.12: Geometry of electrode tip, with labels corresponding to the equation frameworks

$$R_e = \frac{\frac{\Delta V}{i}}{tip\_area} = \frac{\frac{0.06}{i_0}}{tip\_area} = \frac{\frac{0.06}{i_0}}{l_{tip\_exposure} * d_{electrode}} \quad (6)$$

$$C_e = C_{dbl} * \text{tip\_area} = C_{dbl} * l_{tip_{exposure}} * d_{electrode} \quad (7)$$

Eq. 6 shows the approximation for Re from literature[15], where i_0 = 4.5E-14 A/um^2. C_e makes use of a double layer capacitor measurement that has been previously made, resulting in C_{dbl} = 0.2pF/um^2.[15]

Electrode bulk resistance (Rm): the resistance of the material used as the electrode.

$$R_m = \frac{\rho L}{A} \quad (8)$$

where ρ is the resistivity of the electrode material (Ωμm), L is the length of the electrode(um), and A is the cross-sectional area of the electrode (um^2).

Amplifier impedance (Za): the amplifier is a high impedance element over which ideally very little voltage is dropped relative to the low-impedance electrode. This value is dictated by the circuit design of the amplifier, and while we investigate different impedance values later in this work, we do not model this value from first principles.

Shunt resistance and capacitance (Rsh, Csh): defects in the insulation allow new conduction paths directly between the electrode and surrounding fluid- and this new RC network effectively decreases the impedance across the amplifier, increasing losses in the voltage divider.

$$R_{sh} = \frac{\rho_{solution}}{2\pi d_{defect}} \quad (9)$$

$$C_{insulation} = \frac{\epsilon_0 k_{insulation} A_{insulation}}{t_{insulation}} \quad (10)$$

$$C_{defect} = \frac{\epsilon_0 k_{solution} A_{defect}}{t_{insulation}} \quad (11)$$

$$C_{sh} = C_{insulation} + C_{defect} \quad (12)$$

with $k_{insulation}$ as the dielectric constant of the insulation material, $A_{insulation}$ the surface area of the electrode that is covered by insulation, $t_{insulation}$ as the thickness of the insulation, $k_{solution}$ as the dielectric constant of the liquid surrounding the implant, and A_{defect} as the surface area of the electrode not covered by insulation. Further detail about the physical origins of Rsh and Csh can be found in section 5.5.2.

5.4.2.2 Noise Model

In a neural implant, the two main sources of noise are overlapping signal from nearby neurons, and thermal noise produced by the electrode material itself, known as Johnson noise[19]. To simplify the model, we ignored neighboring neurons, and do not consider the impact of their signal on the neuron of interest. While it would be possible to generate a random distribution of neurons within the measurement volume and use the current model to estimate the impact of nearby neurons, this avenue was not pursued in this work. We have focused on the thermal Johnson noise that arises from the agitation of electronic carriers due to temperature. Johnson noise is quantified in eq. 13, where kB is Boltzmann's constant, T is temperature in Kelvin, BW is bandwidth in Hz, and R is resistance in ohms. For the model, we assumed 37°C operation across a bandwidth of 7 kHz[16].

$$V_{RMS} = \sqrt{4k_B \cdot T \cdot R \cdot BW} \tag{13}$$

Using this formula, we calculate that a tungsten microelectrode (ρ=5.6E-2 Ωμm, L=1mm, r=25um) with 50um of tip exposed will result in 7uV of thermal noise. Reports from implanted systems registered 20-50uV of noise[3]. The model's inability to account for nearby neurons likely accounts for the remainder of noise that we should expect.

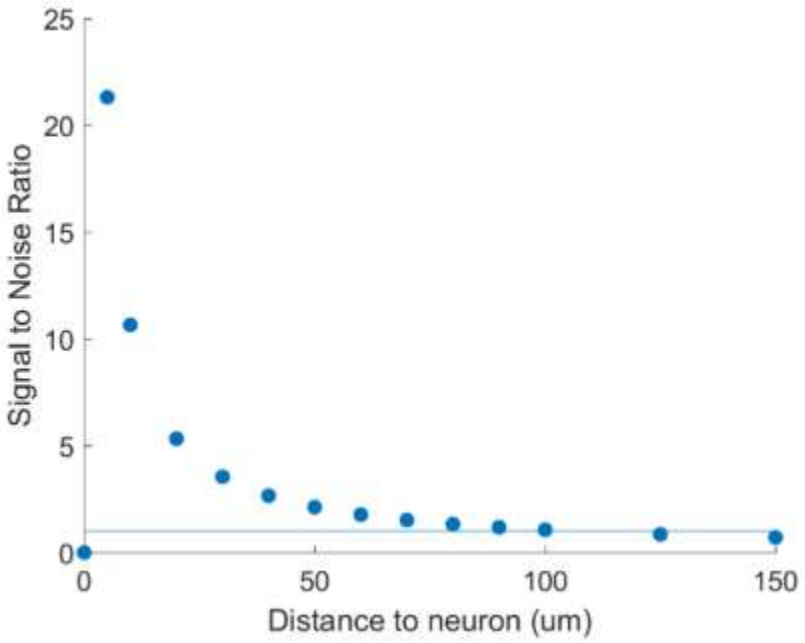

Figure 5.13: Plot of signal-to-noise ratio (SNR) vs distance, with a SNR=1 cutoff line shown

In Figure 5.13, we plot the SNR vs distance relationship for the baseline tungsten wire system. We observed that a distance 70-95um is where SNR decays very near the threshold of 1, which is in agreement with literature values that estimate 50-100um maximum distances for recording

electrodes[20]. We use this fact as validation that the model is reasonably approximating the signal and noise conditions of a recording electrode in the brain, and that using SNR as a metric is reasonable.

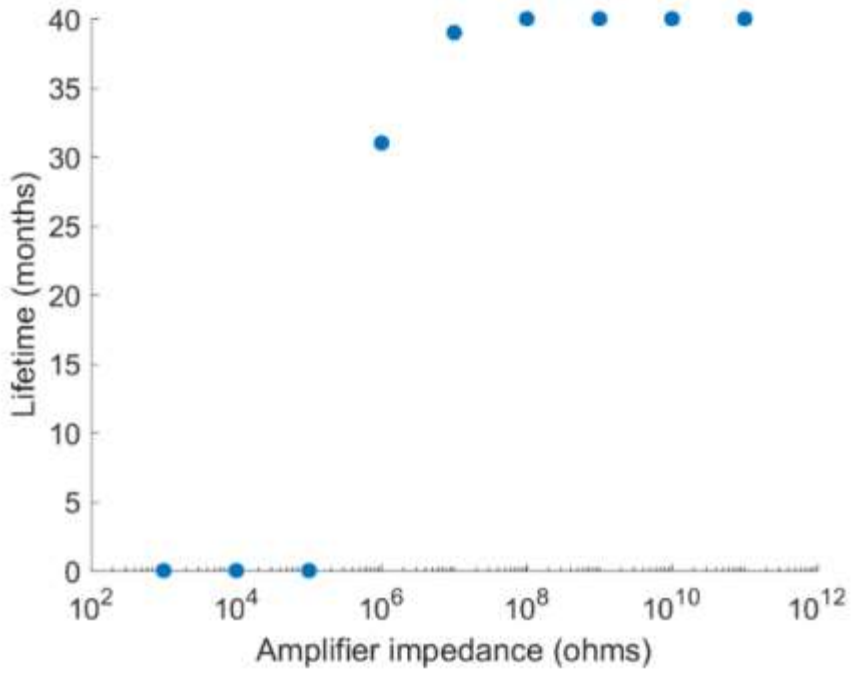

Figure 5.14: Plot of amplifier impedance vs device lifetime

Because the amplifier impedance is critical to the voltage divider-based model, we first investigate the sensitivity of the model to the assumed value of the amplifier impedance. Figure 5.14 shows that above 100MΩ, the benefits of increasing amplifier impedance are marginal. For the remainder of this work, we use 10GΩ as the starting Za value in the circuit model because it falls within the range of impedance values that do not degrade implant lifetime.

As shown in Figure 5.15, we find that electrode resistivity is not a critical parameter for the L=1mm, r=25um electrode geometry. The resistivity of most metals is around 1E-2 Ωμm, making the critical value of 1E4 equal to 6 orders of magnitude away. Even carbon fiber, which is 200 times more resistive than tungsten, is still well below the critical threshold derived with the model[10].

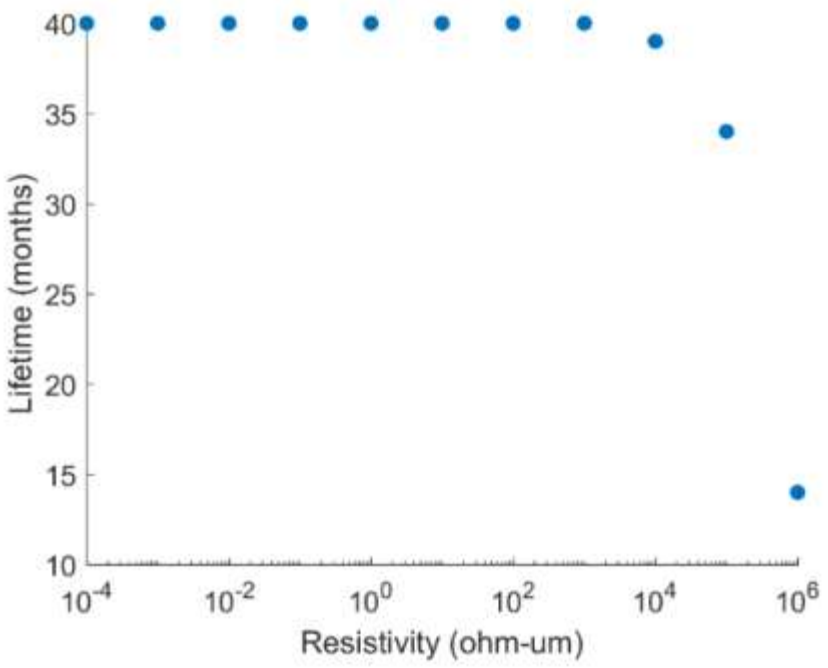

Figure 5.15: Plot of electrode material resistivity vs device lifetime

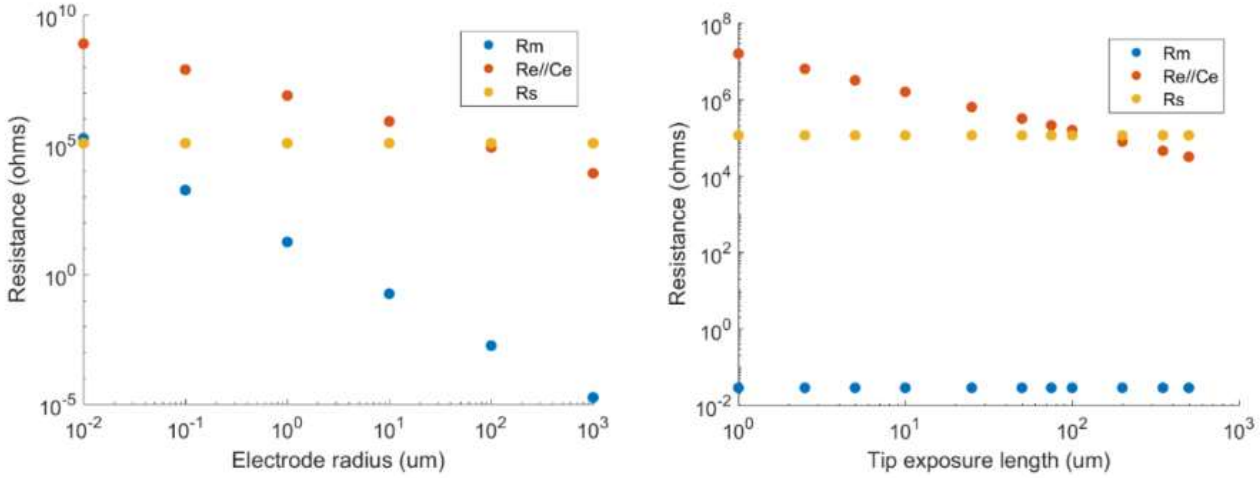

Figure 5.16: (a, left) Plot of electrode radius vs resistance (tip exposure = 50um), for each electrode component (b, right) Plot of tip exposure length vs resistance (electrode radius = 25um), for each electrode component

The equivalent circuit model comprises three components that describe the electrode resistance: the spreading resistance (Rs), tip resistance and capacitance (Re//Ce), and the bulk resistance (Rm). We investigated which of these terms was dominant, if any, after seeing the resistivity,

which mostly affects Rm, plays a minor role. The results in Figure 5.16 confirm that Rm is negligible but indicates that Re//Ce and Rs are both relevant.

Modern devices use a radius of 20-80um for their electrodes, with 5-10um in use for state-of-the-art devices. Around 10um electrode radius, Re//Ce dominate and because tip area is the main variable for Re//Ce, this suggests that increasing tip area (either increasing radius or tip exposure length) would reduce electrode resistance for small-radius electrodes. For radii where Rs dominates, making the tip of the electrode wider would help reduce spreading resistance. (For the model we have fixed tip width at 1um) These findings highlight an important device criterion: optimizing tip geometry, as opposed to focusing on the bulk electrode material, will dominate the electrode tip RC circuit.

However, the model does not yet incorporate the effect of electrode radius on the glial response or damage due to insertion. We expect that a larger radius electrode would provoke an increased glial response and cause more damage upon insertion creating a tradeoff between electrode resistance and biological damage.

5.5 Biological and Physical Models

5.5.1 Biological Modelling

Based on the idea that the body forms an encapsulation layer to protect itself from an implant shown in Figure 5.2, we built a model that explores the relationship between the biological encapsulation and the performance of the device. By treating the encapsulation as a region separating the electrode tip from the nearest neuron and using the model basis defined above, we can relate the biological response to the lifetime of the device. We used the data from [18] as the source for encapsulation growth as a function of time. Since EP-1 is an indicator of gliosis, we define the region where ED-1 fluoresces above 0.02 as the depth of the encapsulation layer (figure 5.17).

Recognizing the trend towards softer devices, we built the dependence of encapsulation as a function of modulus into the model. Using [19] as a basis (figure 5.18), we have a logarithmic equation representing this relationship at one month. Since [19] was conducted on the abdomen of mice, we calibrated the values by matching them to [18], conducted in the brain.

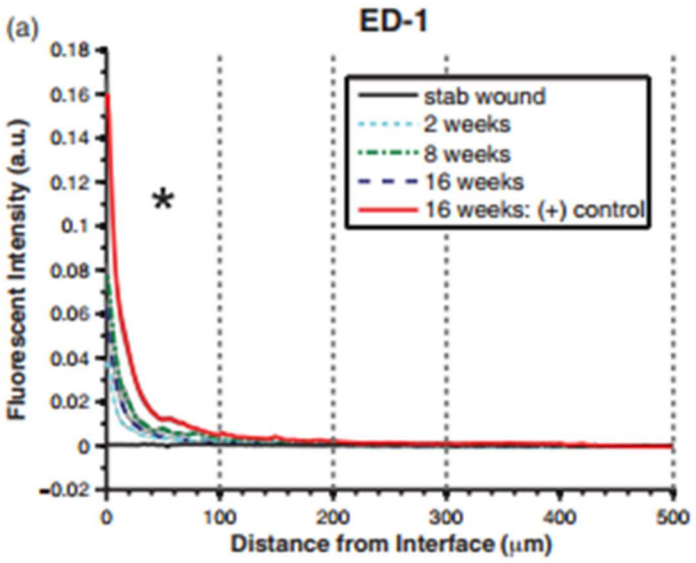

Figure 5.17: ED-1 expression (an indicator for activated microglia) was measured as a function of distance from the surface of UEA implants using fluorescence[18].

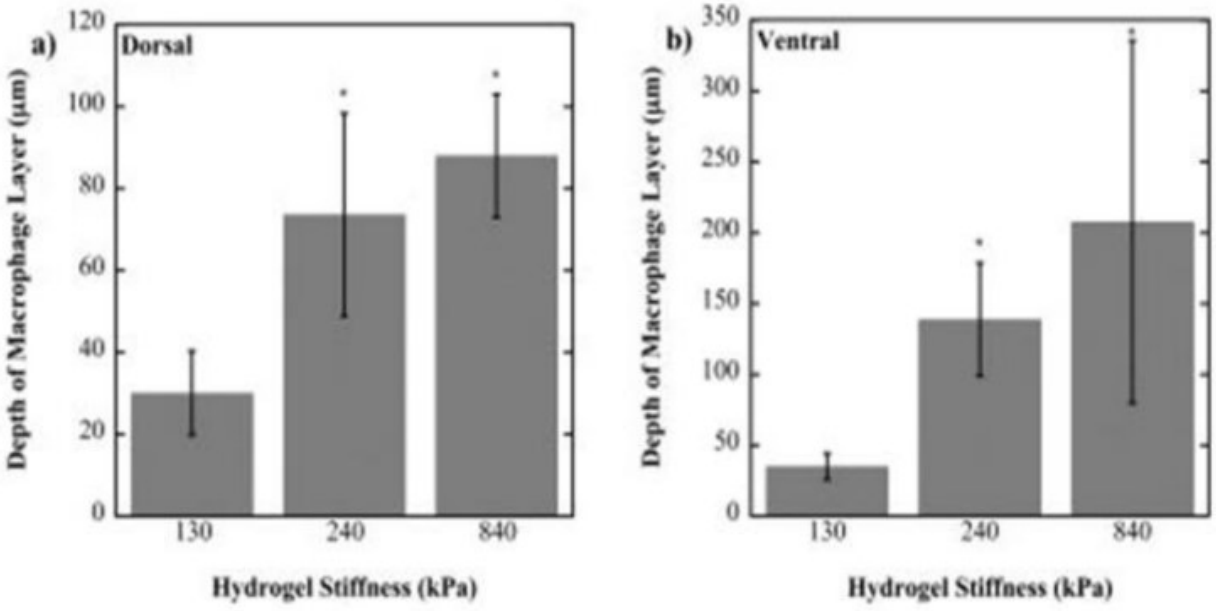

Figure 5.18: The macrophage layer surrounding a PEG implant was measured at 28 days as a function of the PEG modulus. The PEG was implanted in the dorsal and ventral sides of the abdomen of immunocompetent mice[19].

Using these two datasets, we generated a plot of predicted encapsulation as a function of time (figure 5.19). As expected, softer devices are unlikely to fail due to biological factors within five years. Devices made of silicon (140 GPa) see encapsulations in the 40 um range after just a few years, a distance that reduces SNR to ~3 according to figure 5.8.

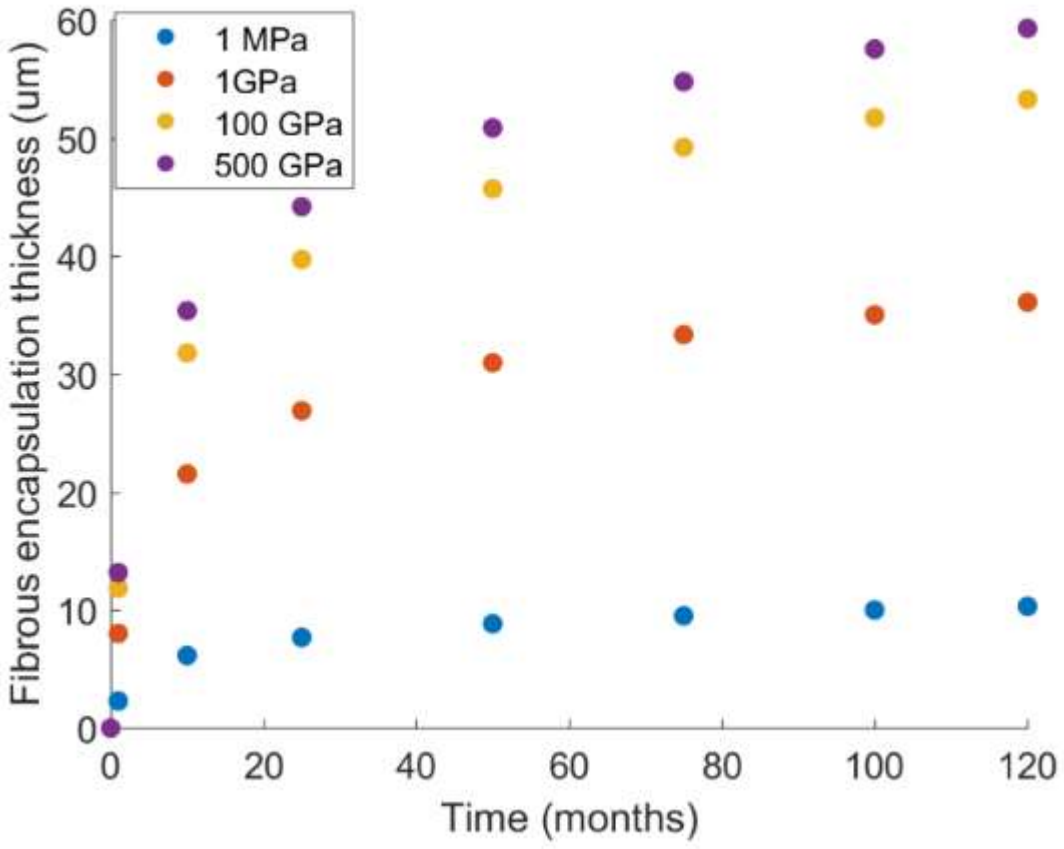

Figure 5.19: Encapsulation thickness as a function of time generated using Chronic-Minded Design model. Stiff devices are expected to fail much sooner due to the biological response than soft materials.

5.5.2 Physical Defect Modelling

When considering materials failure in neural implants, the field has provided evidence for a variety of failure modes, including delamination of the insulation, pinholes present from manufacturing, cracking of the insulation and/or electrode, and tip dissolution[3]. One of the primary goals with this chapter was to incorporate the main failure modes into an equivalent circuit model, enabling quantitative analysis of how these material failures translate into loss of device lifetime. This

section describes how we characterized material failures, and how they have been incorporated into the model.

To simplify the model, we took delamination, cracking, and pinholes to all result in the same issue: removal of insulation from a section of the electrode. By making this claim, we reform the objective of this section to modeling how a loss of insulation over some given area affects the voltage divider that we have established in the equivalent circuit.

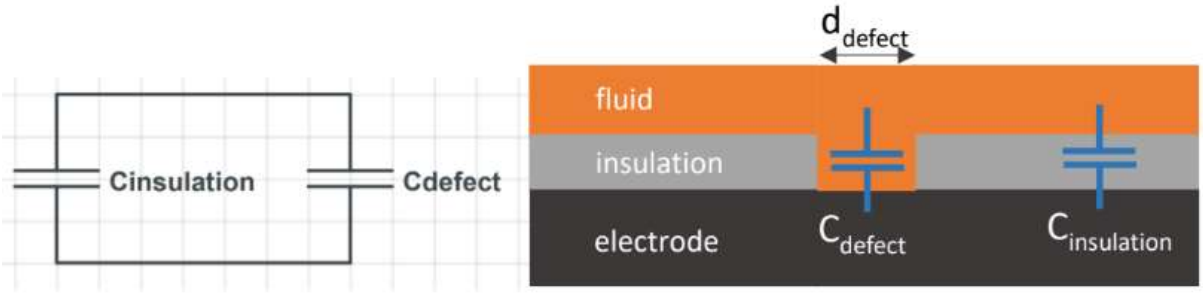

Figure 5.20: (left) Simplified circuit model of two capacitances contributing to Csh (right) Cross sectional view of fluid insulation-electrode interface, highlighting the origins of $C_{insulation}$ and C_{defect}. The d_{defect} term shows the defect diameter, which is used to determine the area of the defect.

In section, 5.4.2.1, we stated that maximizing Za', the amplifier impedance, will maximize V_{rec} and SNR. The shunt capacitance is an important contributor to Za' and the shunt capacitance will be modified by the removal of insulating material. Csh was modeled as two capacitors in parallel in eq. 12. $C_{insulation}$ represents the surface area covered by insulation and is a parallel plate capacitor with dielectric constant corresponding to that of typical insulation. (k=3, corresponding to k of Parylene C, was used for this work[21]) C_{defect} was modeled as parallel plate capacitor, with the dielectric constant of saline used to simulate the fluid around the implant (k=50[26]), and the area of the defect used as the capacitor area.

We modeled Rsh in the same way as Rs: a small surface of the surrounding liquid of resistivity of $\rho_{solution}$, with d_{defect} representing the defect diameter (seen the right image in Fig 20). As this defect gets larger in diameter, the resistance of the defect pathway gets lower, which drags the impedance seen across the amplifier lower, and causes loss of signal.

With a physical model outlined for defects, we then sought to characterize how different size defects would affect device lifetime. For this, we chose to investigate different defect growth rates, as we made the assumption that defects continue to grow and evolve over time. This is likely an imperfect assumption, especially the idea that growth is completely uniform over time, but very little data exists on defects growth for implanted films, and we recognize this assumption as a limitation of the current model.

Using the measured dissolution rate of SiO_2 in PBS as a starting point (0.04 nm/day of SiO_2[6]), we show the effect of defect growth rate on device lifetime, ranging from 0.05 to 1 nm/day in Figure 5.21. We show that defect growth rate is a significant factor, and this is not surprising given the attention paid to defects in device design. These defects introduce shunt paths and are in parallel with the amplifier impedance, meaning the presence of any defect, even ones that are small relative to the total surface area of the electrode, are likely to drop the amplifier impedance significantly. The important takeaway for material designers and device engineers is that virtually no surface defects are tolerable, and materials that can be deposited without defects or delamination should have very high priority, even in spite of other tradeoffs they may present.

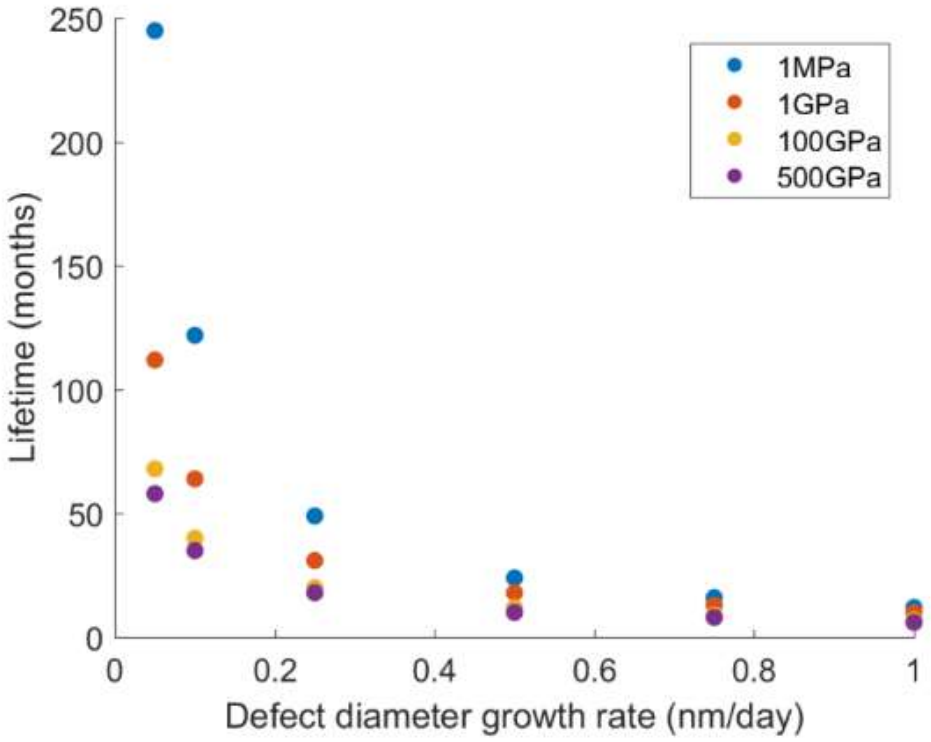

Figure 5.21: Plot of defect growth rate vs device lifetime

5.6 Discussion

The literature data used for this modelling effort was limited, but sufficient to reach a lifetime prediction model that incorporates material properties, the biological response to implants, and defect modelling. Figure 5.19 and 5.21 indicate that the elastic modulus of the implant material is a critical factor in implant lifetime. The additional glial encapsulation provoked by the insertion of high-modulus electrodes pushes the electrode further from the measured neuron, and limits high

modulus (>1GPa) electrode lifetimes. This model predicts that the use of highly compliant electrodes is valuable in extending intracortical implant lifetimes. While compliant materials often make sacrifices in conductivity, ease of handling, or ease of fabrication, the improvements in lifetime are significant. This finding aligns with a trend towards more flexible devices that was described in chapter 1.

Figure 5.16 plots the results of the equivalent circuit model, separating the magnitude of the contributions to electrode impedance. At nearly every electrode geometry, electrode resistivity is not the dominant contributor to electrode impedance. Instead, the majority of resistance in the electrode comes from the tip resistance, tip capacitance, and spreading resistance. These values are all dependent on the amount of the electrode tip exposed and the radius of the electrode. While minimizing exposed electrode area can result in a higher density of recording sites and higher neuronal specificity, care should be taken to ensure that the competing demand of minimizing electrode impedance is considered.

The model suggests very low tolerance for defects in figure 5.21. An increase in defect growth rate of less than 1 nm/day can reduce the lifetime of a soft implant from more than 5 years to less than a year. Defects are typically avoided, but the pursuit of highly compliant materials may see a reduction in material durability. It is important for implant designers to ensure that highly flexible implants can be fabricated with high adhesion and pinhole-free insulation materials or the lifetime improvement benefits earned through the reduction in fibrous tissue formation will be lost to defect formation.

5.6.1 Assumptions and weaknesses of the model

While this model represents a step forward in the modeling of device lifetime for neural implants, there are several important limitations that are more important to address.

1. The impact of neighboring neurons on noise: We know that neighboring neurons contribute noise to a neuron being measured, but we have made no attempt to quantify how severe this noise may be.
2. Detailed data on defect growth rates for insulation materials: The model shows sensitivity to defect growth rate, but absolute lifetime values are inaccurate unless we have a clearer picture of how different materials produce defects over time. Studies like [6] are extremely valuable in the implant designer's toolbox of material properties.
3. The effect of electrode cross sectional area on glial scarring: It is intuitive that a larger radius electrode will cause more damage upon implantation and likely lead to more glial

scarring due to the increased volume displacement from larger electrodes. Due to insufficient data in the literature, we were unable to account for the effect of implant geometry on glial scarring.

4. The effect of tip dissolution on electrode impedance: We have seen that tip conductivity and geometry affects the resistance of the electrode, and we expect that if the tip were to dissolve over time, this change in geometry would affect the conductivity. However, we have not attempted to model tip dissolution in this version of the model. This may not be a large oversight as modern implants are designed to resist dissolution.
5. Detailed data on the modulus-glial response interaction: We have attempted to model the expected thickness of glial scarring as a function of the electrode Young's modulus, but data is lacking in this area, particularly data on glial scarring in human brains.

5.7 Conclusion

This chapter set out to quantify the major mechanisms that allow electrode/insulation systems to measure neural signals and investigate how material and environmental factors affect device performance over time. Here we present a model that breaks a microelectrode system into subcomponents via an equivalent circuit model, which allows for investigation of specific electrical and material properties while remaining general enough to apply to a wide class of electrodes. After validating that the results produced by the model are similar to those seen experimentally (namely, that distance vs signal amplitude, SNR, and max recording distance are all in line with literature values), we investigate how conductivity, electrode radius, amplifier impedance, electrode modulus, and defect growth rate affect device lifetime. The key factors influencing implant performance were implant geometry, implant stiffness, and insulation defect growth rate. These factors tend to compete with each other and the implant that achieves stable, chronic intracortical recording will solve the optimization problem through a combination of compliant, durable, and low impedance materials selection and implant design.

5.8 Acknowledgements

This chapter was adapted from unpublished work by the authors, Jake Sporrer and Dr. Matt Mcphail. The authors would like to thank Prof. Kevin Healy and Prof. Jose Carmena for guidance on the direction of this project.

5.9 References

1. Hochberg, L., Bacher, D., Jarosiewicz, B. et al. Reach and grasp by people with tetraplegia using a neurally controlled robotic arm. Nature 485, 372–375 (2012). https://doi.org/10.1038/nature11076
2. Miranda, Robbin A., William D. Casebeer, Amy M. Hein, Jack W. Judy, Eric P. Krotkov, Tracy L. Laabs, Justin E. Manzo, et al. "DARPA-Funded Efforts in the Development of Novel Brain–Computer Interface Technologies." Journal of Neuroscience Methods, Brain Computer Interfaces; Tribute to Greg A. Gerhardt, 244 (April 15, 2015): 52–67. https://doi.org/10.1016/j.jneumeth.2014.07.019.
3. Barrese, James C., Naveen Rao, Kaivon Paroo, Corey Triebwasser, Carlos Vargas-Irwin, Lachlan Franquemont, and John P. Donoghue. "Failure Mode Analysis of Silicon-Based Intracortical Microelectrode Arrays in Non-Human Primates." Journal of Neural Engineering 10, no. 6 (November 2013): 066014. https://doi.org/10.1088/1741-2560/10/6/066014.
4. Sridharan, Rukmani, Andrew R. Cameron, Daniel J. Kelly, Cathal J. Kearney, and Fergal J. O'Brien. "Biomaterial Based Modulation of Macrophage Polarization: A Review and Suggested Design Principles." Materials Today 18, no. 6 (July 1, 2015): 313–25. https://doi.org/10.1016/j.mattod.2015.01.019.
5. Takmakov, Pavel, Kiersten Ruda, K. Scott Phillips, Irada S. Isayeva, Victor Krauthamer, and Cristin G. Welle. "Rapid Evaluation of the Durability of Cortical Neural Implants Using Accelerated Aging with Reactive Oxygen Species." Journal of Neural Engineering 12, no. 2 (January 2015): 026003. https://doi.org/10.1088/1741-2560/12/2/026003.
6. Fang, Hui, Jianing Zhao, Ki Jun Yu, Enming Song, Amir Barati Farimani, Chia-Han Chiang, Xin Jin, et al. "Ultrathin, Transferred Layers of Thermally Grown Silicon Dioxide as Biofluid Barriers for Biointegrated Flexible Electronic Systems." Proceedings of the National Academy of Sciences 113, no. 42 (October 18, 2016): 11682–87. https://doi.org/10.1073/pnas.1605269113.
7. Ledochowitsch, P., R. F. Tiefenauer, B. Pepin, M. M. Maharbiz, and T. J. Blanche. "Nanoflex for Neural Nanoprobes." In 2013 Transducers & Eurosensors XXVII: The 17th International Conference on Solid-State Sensors, Actuators and Microsystems (TRANSDUCERS & EUROSENSORS XXVII), 1278–81, 2013. https://doi.org/10.1109/Transducers.2013.6627009.
8. Subbaroyan, Jeyakumar, David C. Martin, and Daryl R. Kipke. "A Finite-Element Model of the Mechanical Effects of Implantable Microelectrodes in the Cerebral Cortex." Journal of Neural Engineering 2, no. 4 (October 2005): 103. https://doi.org/10.1088/1741-2560/2/4/006.

9. Kozai, Takashi D. Y., Kasey Catt, Xia Li, Zhannetta V. Gugel, Valur T. Olafsson, Alberto L. Vazquez, and X. Tracy Cui. “Mechanical Failure Modes of Chronically Implanted Planar Silicon-Based Neural Probes for Laminar Recording.” Biomaterials 37 (January 1, 2015): 25–39. https://doi.org/10.1016/j.biomaterials.2014.10.040.
10. Guitchounts, Grigori, Jeffrey E. Markowitz, William A. Liberti, and Timothy J. Gardner. “A Carbon-Fiber Electrode Array for Long-Term Neural Recording.” Journal of Neural Engineering 10, no. 4 (July 2013): 046016. https://doi.org/10.1088/1741-2560/10/4/046016.
11. Luan, Lan, Xiaoling Wei, Zhengtuo Zhao, Jennifer J. Siegel, Ojas Potnis, Catherine A Tuppen, Shengqing Lin, et al. “Ultraflexible Nanoelectronic Probes Form Reliable, Glial Scar–Free Neural Integration.” Science Advances 3, no. 2 (February 15, 2017): e1601966. https://doi.org/10.1126/sciadv.1601966.
12. Diaz-Botia, C.A., L.E. Luna, M. Chamanzar, C. Carraro, P.N. Sabes, R. Maboudian, and M.M. Maharbiz. “Fabrication of All-Silicon Carbide Neural Interfaces.” In 2017 8th International IEEE/EMBS Conference on Neural Engineering (NER), 170–73, 2017. https://doi.org/10.1109/NER.2017.8008319.
13. Seo, Dongjin, Jose M. Carmena, Jan M. Rabaey, Elad Alon, and Michel M. Maharbiz. “Neural Dust: An Ultrasonic, Low Power Solution for Chronic Brain-Machine Interfaces.” arXiv, July 8, 2013. https://doi.org/10.48550/arXiv.1307.2196.
14. Kovach, Kyle M., Doe W. Kumsa, Vishnupriya Srivastava, Eric M. Hudak, Darrel F. Untereker, Shawn C. Kelley, Horst A. von Recum, and Jeffrey R. Capadona. “High-Throughput in Vitro Assay to Evaluate the Cytotoxicity of Liberated Platinum Compounds for Stimulating Neural Electrodes.” Journal of Neuroscience Methods 273 (November 1, 2016): 1–9. https://doi.org/10.1016/j.jneumeth.2016.07.018.
15. Robinson, D.A. “The Electrical Properties of Metal Microelectrodes.” Proceedings of the IEEE 56, no. 6 (June 1968): 1065–71. https://doi.org/10.1109/PROC.1968.6458.
16. Lind, R., P. Connolly, C. D. W. Wilkinson, and R. D. Thomson. “Finite-Element Analysis Applied to Extracellular Microelectrode Design.” Sensors and Actuators B: Chemical 3, no. 1 (January 1, 1991): 23–30. https://doi.org/10.1016/0925-4005(91)85004-3.
17. Nelson, Matthew J., Pierre Pouget, Erik A. Nilsen, Craig D. Patten, and Jeffrey D. Schall. “Review of Signal Distortion through Metal Microelectrode Recording Circuits and Filters.” Journal of Neuroscience Methods 169, no. 1 (March 30, 2008): 141–57. https://doi.org/10.1016/j.jneumeth.2007.12.010.
18. McConnell, George C., Howard D. Rees, Allan I. Levey, Claire-Anne Gutekunst, Robert E. Gross, and Ravi V. Bellamkonda. “Implanted Neural Electrodes Cause Chronic, Local Inflammation That Is Correlated with Local Neurodegeneration.” Journal of Neural Engineering 6, no. 5 (August 2009): 056003. https://doi.org/10.1088/1741-2560/6/5/056003.

19. Polikov, Vadim S., Patrick A. Tresco, and William M. Reichert. “Response of Brain Tissue to Chronically Implanted Neural Electrodes.” Journal of Neuroscience Methods 148, no. 1 (October 15, 2005): 1–18. https://doi.org/10.1016/j.jneumeth.2005.08.015.
20. Shoham, Shy, and Srikantan Nagarajan. “The Theory of Central Nervous System Recording.” In Neuroprosthetics, Volume 2:448–71. Series on Bioengineering and Biomedical Engineering, Volume 2. WORLD SCIENTIFIC, 2004. https://doi.org/10.1142/9789812561763_0014.
21. Wellman, Steven M., James R. Eles, Kip A. Ludwig, John P. Seymour, Nicholas J. Michelson, William E. McFadden, Alberto L. Vazquez, and Takashi D. Y. Kozai. “A Materials Roadmap to Functional Neural Interface Design.” Advanced Functional Materials 28, no. 12 (2018): 1701269. https://doi.org/10.1002/adfm.201701269.
22. Homer, Mark L., Arto V. Nurmikko, John P. Donoghue, and Leigh R. Hochberg. “Implants and Decoding for Intracortical Brain Computer Interfaces.” Annual Review of Biomedical Engineering 15 (2013): 383–405. https://doi.org/10.1146/annurev-bioeng-071910-124640.

Chapter 6. Conclusions and future directions

6.1 Conclusions

This thesis described a microfluidic platform for accelerated aging of bioelectronic implants. To demonstrate the value of such a platform, model intracortical implants made of tungsten or platinum/iridium coated in Parylene C were purchased from a commercial supplier of neural probes. These implants were aged using two methods, the heated saline/hydrogen peroxide method and the immune cell method. Chapter 2 described the design, fabrication, and validation of the microfluidic chamber as a platform capable of performing both aging methods.

In chapter 3, the state-of-the-art accelerated aging method was evaluated in the microfluidic system. Implants were surrounded by a heated phosphate buffered saline and hydrogen peroxide solution. Using electron microscopy, impedance analysis, and energy dispersive X-ray spectroscopy, the degradation of these implants was compared to previous studies and in vivo degradation. This method showed that the saline/hydrogen peroxide method was representative at reproducing many of the degradation mechanisms observed in vivo. This method also showed that increasing the aging time, the temperature of aging, and the hydrogen peroxide concentration increased the degree of degradation.

In chapter 4, an immune cell accelerated aging method was introduced. For this method, implants were placed in a microfluidic bioreactor containing immune cells. These cells were stimulated to produce reactive oxygen. The degradation of the implants was characterized using the same methods as in chapter 3. The aging time and total number of cell activation events were found to be statistically significant factors contributing to the degradation of both probe types. The rate of tungsten probe dissolution was lower in immune cell aged chambers than saline/hydrogen peroxide chambers, likely owing to the difference in temperature. Interestingly, the degree of reactive oxygen-induced polymer chain scission was higher for implants aged in the immune cell chamber than implants aged in the saline/hydrogen peroxide chamber. The immune cell aging method was capable of acceleration of tungsten dissolution as well as reactive oxygen-induced polymer chain scission, two key failure mechanisms present in vivo. A comparable maximum acceleration is achievable for both methods, 32x for heated saline aging and 39.7x for immune cell aging.

Chapter 5 described a modelling framework for the prediction of intracortical implant lifetime. This model included considerations of biological and material failures. The bulk of this dissertation has primarily considered implant durability from a materials perspective. Significant acceleration of fibrous tissue formation and neuron death is currently not possible. To address this type of biological failure, in vivo testing is required. One goal of the modelling framework described in chapter 5 is to provide an avenue to reduce the in vivo testing required for implant validation by modelling fibrous tissue growth as a function of implant modulus. Several studies have been performed to evaluate the generalized biological response as a function of material properties[12,13]. The results of these studies were combined with an

insulation defect growth rate model, a model of a representative neuron, and an equivalent circuit model of an intracortical implant to predict the lifetime of an implant where the recorded neuron signal strength exceeds thermal noise.

The goal of this work was to propose a new accelerated aging method for bioelectronic implants, compare that method to the current state of the art, and show how both methods can be improved by microfluidic technology. While this work has expanded the toolbox of accelerated aging for neural implant designers, there is significant room for innovation. The next sections will describe potential avenues to make this technology more accessible, representative, and versatile.

6.2 Advancing microfluidic accelerated aging of bioelectronic implants

6.2.1 Automating microfluidic chamber maintenance

The microfluidic platform described in this dissertation required a reasonable degree of human interaction and maintenance. The hydrogen peroxide aging scheme described in chapter 3 required syringes to be refilled with fresh PBS/hydrogen peroxide solutions. The immune cell aging scheme described in chapter 4 required the syringes to be refilled with complete cell culture media/PMA solutions and required the microfluidic bioreactors to be refilled with complete cell culture media each day. There are certainly automated pump systems that can handle this type of maintenance without human interaction. Automation of these daily refills is required for the microfluidic aging platform to be scaled up to large numbers of implants. Similar to the peroxide system[1] that achieved increased automation of peroxide maintenance[2], a first step to increasing the accessibility of the microfluidic aging platform is automation.

6.2.2 Multimode aging schemes

One concept for accelerated aging is to combine the immune cell aging method with the heated saline method. In theory, an ideally designed implant would not cause a significant immune response over its entire lifetime. A well designed intracortical implant would still elicit a significant immune response upon implantation. Intracortical implants penetrate the brain by definition. The immune response to implantation can be minimized by varying implantation parameters, like speed, implant geometry, or stiffness[3], but will never be completely eliminated. However, if an implant were able to integrate successfully with brain tissue because it was free floating, compliant, and small, the immune response after several years of implantation would be minimal. In this case, a representative aging scheme would be to replicate the conditions of the initial response for some time and then to replicate the conditions of the chronic response later. These aging conditions could be achieved in the microfluidic chamber platform without removing the implant.

The multimode aging method would see implants attacked by the immune cell aging system for several weeks to months of accelerated time. In this regime, aging would proceed as described

in chapter 4, immune cells would produce reactive oxygen to simulate the immune response in the body. After the initial immune response phase ends, the cells would be flushed from the chamber and replaced with a representative saline solution. The implant aging process would then proceed as described in chapter 3, without the hydrogen peroxide addition. The microfluidic chamber would be removed from the cell culture incubator and placed on a hotplate to undergo thermal acceleration.

This strategy relies on the assumption that the immune response subsides after some time. Implant designers would need to be confident that their implant will not elicit a chronic immune response. Implants that do not elicit a chronic immune response are not currently served by any accelerated aging method. A pure saline aging method ignores the acute immune response, and a saline/hydrogen peroxide method subjects the implant to hydrogen peroxide attack for the entire lifetime of the aged implant, an attack that the implant would not see in vivo. A well-chosen hybrid aging scheme will be able to reproduce the conditions experienced by an implant better than any single method can.

6.2.3 Peripheral nerve implant fatigue acceleration

One aging scheme that might be integrated into a hybrid aging method is mechanical failure. There is a significant push to develop stretchable electronics for the peripheral nervous system. Unlike implants in the brain, peripheral nervous system implants undergo significant motion during operation. To address this, implant designers have developed several stretchable probe designs. Liquid metals and microcracked materials have been proposed to address stretchability issues[4,5]. These implants need to experience accelerated aging not just for the chemical and biological attacks they will undergo, but for the mechanical fatigue they may experience in use. While chapter 2 described a microfluidic platform using glass and PDMS, fully PDMS microfluidic chambers have been demonstrated in literature[6]. A fully PDMS chamber could be mounted to a mechanical system intended to replicate the type of motion a probe may experience in the body. This mechanical system would be able to bend the microfluidic chamber and the electrode repeatedly to accelerate the mechanical conditions the electrode would be expected to endure.

6.2.4 Non-biological generation of reactive species

In chapter 4, repeat activation of J774a.1 cells generated the reactive species used for accelerated aging. There are other methods for generating reactive species that do not require cells. One such method is the use of Fenton's reagent, a hydrogen peroxide and iron solution that generates superoxide[9]. This chemical method of reactive oxygen generation is likely more reliable at producing specific quantities of reactive oxygen than any biological method could be. The Fenton method does require a specific chemistry to function, limiting its application as a representative aging environment (the chemistry of the brain is a significant contributor to implant failure, as can be observed by tungsten probe dissolution in vivo). Another strategy is the use of pulse radiolysis. In [7], a 2 MeV electron Van de Graaff

accelerator was used to generate reactive oxygen in water. Using radiation to generate reactive oxygen does not require a specific chemistry and could be an avenue toward reactive oxygen-based acceleration. This method does require a source of high energy electrons to function, increasing complexity. Additionally, the direct impact that these high energy electrons might have on the implant itself must be considered. These methods do not require the use of cell culture, simplifying them in some respects compared to the scheme proposed in chapter 4. The use of a Fenton's reagent aging scheme has been hinted at by other researchers as a potential acceleration avenue[8]. A comparison between the effects of non-biologically generated reactive species and the immune cell-generated species described in chapter 4 could potentially provide valuable information about how specific reactive species contribute to each failure mechanism.

6.2.5 Using human cells for microfluidic accelerated aging of neural implants

This work showed a non-biological reactive oxygen attack, hydrogen peroxide, as well as a biological reactive oxygen attack, mouse immune cells. A potential route to even more representative aging is the use of human cells. Human cells are the closest biological analogue to humans themselves. To most accurately recreate the immune response experienced by a human brain, cultured human neurons and glial cells would be ideal. One potential avenue for the exploration of the acceleration of the human brain's neural response is the use of stem cells. Stem cells are cells that can differentiate into many different cell types. There are three main types of stem cells that might be useful for microfluidic accelerated aging: embryonic stem cells, induced pluripotent stem cells (iPSC), and tissue-specific stem cells.

Embryonic stem cells are obtained from the inner cell mass of an embryo three to five days after the egg cell is fertilized and can give rise to every cell type in the body except the placenta and umbilical cord. Embryonic stem cells are pluripotent, meaning that they can differentiate into nearly any cell type. These cells are by far the most flexible in the type of cells that they can differentiate into but tend to be difficult to acquire because they must be extracted from human embryos, a practice that faces significant opposition and is even banned in several countries.

Tissue-specific stem cells are cells that have partially differentiated into a cell type but maintain the ability to further differentiate and self-renew. These cells can often be difficult to harvest and tend to be less robust in their self-renewal process, making them difficult to reculture.

Induced pluripotent stem cells (iPSC) are engineered in a lab by converting tissue-specific cells into cells that behave like embryonic stem cells, typically by using a retrovirus to deliver genes to fibroblast cells. Because iPSCs can be created from non-embryonic stem cells, they face less opposition while maintaining the ability to differentiate nearly as freely. iPSC can be differentiated into neural stem cells, stem cells that can differentiate into neurons and glia.

One method to evaluate the immune response to neural implants would be to generate a coculture of neurons and glial cells from iPSCs, introduce a neural implant, and evoke an

increased immune response from these cells. In chapter 4, a process to invoke an increased immune response from mouse cells and use that response to accelerate the degradation of neural implants was described. Replacing those mouse cells with human neuron and glial cells would be a step toward more representative aging. It is an open question whether this neuron/glial cell coculture has an acceleration lever. For the mouse cells, the introduction of PMA caused a production of reactive oxygen. This activation acted as a tunable reactive species generation lever, varying the reactive species generated. Any human cell culture method would need to be able to repeatedly generate reactive species in a similar manner. In the next section, an emerging application for iPSCs will be explored, organoids.

6.2.6 Organoids for microfluidic accelerated aging of neural implants

Organoids are 3-d cell clusters grown from stem cells. They are typically between tens of micrometers and a few millimeters. These cell clusters undergo some degree of differentiation and self-renewal. The goal of organoid research is to create miniature replicas of organs that can perform similar functions as organs found in humans. These organoids are grown using two methods, guided growth and unguided growth. Unguided organoids start as embryoid bodies derived from pluripotent stem cells embedded into an extracellular matrix. They are grown with very little intervention to most accurately replicate the type of differentiation that cells undergo in human growth. As a result, unguided organoids tend to have a high degree of variability. Guided organoids can start as partially differentiated stem cells or embryoid bodies and are grown with specific interventions. Growth factors, mechanical conditions, and environmental modifications can all be used to guide differentiation. These organoids are typically used when a specific cell type is desired, and they exhibit less variance than unguided organoids. Unguided organoids tend to more accurately represent the interactions between cell types, but guided organoids tend to produce desired structures with greater precision.

For representative aging, both precision and accuracy are critical. However, reproducibility is extremely important. Therefore, guided organoids are better suited to accelerated aging of neural implants. Guided organoids have been used to study the immune response to electrode implantation. A model neural implant (a needle) has been introduced to neural stem cell cultures that have differentiated into induced microglia-like stem cells. The response to the implant was evaluated using fluorescence imaging to detect an indicator of glial scarring, glial fibrillary acidic protein. When the implant was introduced, the induced microglia-like stem cells clustered near the injury site and became more rounded, resembling ‘‘activated’’ microglia found in injured or diseased brains [10]. This result shows the potential organoids have as a representative environment for aging.

There are several key challenges associated with using organoids for accelerated aging. First, even though guided organoids are more consistent than unguided organoids, they still suffer from significant organoid to organoid variability. One of the most common extracellular matrix materials to grow organoids in is decellularized tissue which is not consistent in composition [11]. This inconsistency is one of the reasons that even identical preparation protocols will

produce variable organoids. This variability is incompatible with a test intended to evaluate reliability. Second, organoids require careful selection of extracellular matrix and need specific handling protocols that currently only exist in labs that specialize in organoids. Organoid technology is not mature enough to be used as a tool yet. For accelerated aging to utilize organoid technology, a research lab that already specializes in organoid research would need to be involved in the accelerated aging process. Any acceleration scheme should be usable by an implant designer without the need for a partnered research lab. Third, if a reliable brain organoid could be created, a method to cause that brain to accelerate the intensity of its immune response would be required to achieve acceleration. Currently, such a method does not exist. Last, vasculature is a limitation. The size of organoids is limited by the distance over which oxygen can diffuse, typically less than 400 μm[11]. While a small organoid is not necessarily a problem for accelerated aging, vascularization challenges should be considered before organoids are used for aging of neural implants.

6.3 References

1. Takmakov, Pavel, Kiersten Ruda, K. Scott Phillips, Irada S. Isayeva, Victor Krauthamer, and Cristin G. Welle. “Rapid Evaluation of the Durability of Cortical Neural Implants Using Accelerated Aging with Reactive Oxygen Species.” Journal of Neural Engineering 12, no. 2 (January 2015): 026003. https://doi.org/10.1088/1741-2560/12/2/026003.

2. Caldwell, Ryan, Matthew G. Street, Rohit Sharma, Pavel Takmakov, Brian Baker, and Loren Rieth. “Characterization of Parylene-C Degradation Mechanisms: In Vitro Reactive Accelerated Aging Model Compared to Multiyear in Vivo Implantation.” Biomaterials 232 (February 1, 2020): 119731. https://doi.org/10.1016/j.biomaterials.2019.119731.

3. Lecomte, Aziliz, Emeline Descamps, and Christian Bergaud. “A Review on Mechanical Considerations for Chronically-Implanted Neural Probes.” Journal of Neural Engineering 15, no. 3 (March 2018): 031001. https://doi.org/10.1088/1741-2552/aa8b4f.

4. Minev, Ivan R., Pavel Musienko, Arthur Hirsch, Quentin Barraud, Nikolaus Wenger, Eduardo Martin Moraud, Jérôme Gandar, et al. “Electronic Dura Mater for Long-Term Multimodal Neural Interfaces.” Science 347, no. 6218 (January 9, 2015): 159–63. https://doi.org/10.1126/science.1260318.

5. Wen, Ximiao, Bo Wang, Shan Huang, Tingyi “Leo” Liu, Meng-Shiue Lee, Pei-Shan Chung, Yu Ting Chow, et al. “Flexible, Multifunctional Neural Probe with Liquid Metal Enabled, Ultra-Large Tunable Stiffness for Deep-Brain Chemical Sensing and Agent Delivery.” Biosensors and Bioelectronics 131 (April 15, 2019): 37–45. https://doi.org/10.1016/j.bios.2019.01.060.

6. McDonald, J. Cooper, and George M. Whitesides. “Poly(Dimethylsiloxane) as a Material for Fabricating Microfluidic Devices.” Accounts of Chemical Research 35, no. 7 (July 1, 2002): 491–99. https://doi.org/10.1021/ar010110q.

7. Zielonka, Jacek, Tadeusz Sarna, Joan E. Roberts, James F. Wishart, and B. Kalyanaraman. “Pulse Radiolysis and Steady-State Analyses of the Reaction between Hydroethidine and Superoxide and Other Oxidants.” Archives of Biochemistry and Biophysics 456, no. 1 (December 1, 2006): 39–47. https://doi.org/10.1016/j.abb.2006.09.031.

8. Caldwell, Ryan, Matthew G. Street, Rohit Sharma, Pavel Takmakov, Brian Baker, and Loren Rieth. “Characterization of Parylene-C Degradation Mechanisms: In Vitro Reactive Accelerated Aging Model Compared to Multiyear in Vivo Implantation.” Biomaterials 232 (February 1, 2020): 119731. https://doi.org/10.1016/j.biomaterials.2019.119731.

9. Prousek, Josef. “Fenton Chemistry in Biology and Medicine.” Pure and Applied Chemistry 79, no. 12 (January 1, 2007): 2325–38. https://doi.org/10.1351/pac200779122325.

10. Abud, Edsel M., Ricardo N. Ramirez, Eric S. Martinez, Luke M. Healy, Cecilia H. H. Nguyen, Sean A. Newman, Andriy V. Yeromin, et al. “IPSC-Derived Human Microglia-like Cells to Study

Neurological Diseases." Neuron 94, no. 2 (April 19, 2017): 278-293.e9. https://doi.org/10.1016/j.neuron.2017.03.042.

11. Qian, Xuyu, Hongjun Song, and Guo-li Ming. "Brain Organoids: Advances, Applications and Challenges." Development 146, no. 8 (April 16, 2019): dev166074. https://doi.org/10.1242/dev.166074.

12. McConnell, George C., Howard D. Rees, Allan I. Levey, Claire-Anne Gutekunst, Robert E. Gross, and Ravi V. Bellamkonda. "Implanted Neural Electrodes Cause Chronic, Local Inflammation That Is Correlated with Local Neurodegeneration." Journal of Neural Engineering 6, no. 5 (August 2009): 056003. https://doi.org/10.1088/1741-2560/6/5/056003.

13. Polikov, Vadim S., Patrick A. Tresco, and William M. Reichert. "Response of Brain Tissue to Chronically Implanted Neural Electrodes." Journal of Neuroscience Methods 148, no. 1 (October 15, 2005): 1–18. https://doi.org/10.1016/j.jneumeth.2005.08.015.